

UC Irvine

UC Irvine Electronic Theses and Dissertations

Title

Simulations of Runaway Processes in Astrophysics

Permalink

<https://escholarship.org/uc/item/3850j4cn>

Author

Palubski, Igor

Publication Date

2024

Peer reviewed|Thesis/dissertation

UNIVERSITY OF CALIFORNIA,
IRVINE

Simulations of Runaway Processes in Astrophysics

DISSERTATION

submitted in partial satisfaction of the requirements
for the degree of

DOCTOR OF PHILOSOPHY

in Physics

by

Igor Zbigniew Palubski

Dissertation Committee:
Professor Manoj Kaplinghat, Chair
Professor Kevork N. Abazajian
Professor Tim M.P. Tait

2024

DEDICATION

To my family

TABLE OF CONTENTS

	Page
LIST OF FIGURES	v
LIST OF TABLES	x
ACKNOWLEDGMENTS	xi
VITA	xii
ABSTRACT OF THE DISSERTATION	xiv
1 Introduction	1
1.1 The Habitable Zone	1
1.2 Dark Matter and Tensions in Modern Cosmology	4
1.2.1 Dark Matter and Λ CDM Cosmology	4
1.2.2 Evidence for Dark Matter	5
1.2.3 The "small scale crisis" in Cosmology	7
2 Habitability and Water Loss Limits on Eccentric Planets Orbiting Main-Sequence Stars	14
2.1 Abstract	14
2.2 Introduction	15
2.3 Methods	19
2.3.1 Water Loss and Runaway Greenhouse	21
2.3.2 Fractional Habitability	25
2.3.3 Model Inputs	26
2.3.4 Model Validation	28
2.4 Results	31
2.4.1 Fractional Habitability	31
2.4.2 Mass Loss and Runaway Greenhouse Planets	33
2.4.3 Bistability	35
2.4.4 Habitability at Higher Obliquities	37
2.5 Discussion	39
2.6 Conclusions	42

3	No Terminator Habitability on Earth-like M-dwarf Aquaplanets With 1-bar Surface Pressures	44
3.1	Abstract	44
3.2	Introduction	45
3.3	Methods	46
3.4	Results	48
3.5	Discussion	52
3.6	Conclusions	55
4	Numerical Challenges in Modeling Gravo-thermal Collapse in Self-Interacting Dark Matter Halos	57
4.1	Abstract	57
4.2	Introduction	58
4.3	Simulation Framework	61
4.3.1	Implementation of Dark Matter Scattering	63
4.3.2	Implementation of Force-Softening Scheme	66
4.3.3	Implementation of the Time-Stepping Criterion	67
4.3.4	Characterization of the Halo Core	69
4.4	Numerical Effects on SIDM Halo Evolution	70
4.4.1	SIDM Methods	70
4.4.2	Mass Resolution and Initial Conditions	76
4.4.3	Time-Stepping Criterion	77
4.4.4	Adaptive Gravitational Force Softening	82
4.5	Comparison to the Fluid Model	84
4.6	Conclusions	85
5	Breakdown of approximate universality in the evolution of SIDM halos	88
5.1	Abstract	88
5.2	Introduction	89
5.3	Differential Cross Sections	91
5.3.1	Yukawa Scattering	91
5.3.2	Resonant Scattering	93
5.3.3	Velocity Averaging Methods	94
5.4	Simulations	96
5.5	Simulation Convergence	98
5.6	Halo Evolution Under Differential Scattering	101
5.6.1	Predicting Core Formation	102
5.6.2	Predicting Core Collapse Time	106
5.6.3	Evolution of Core Properties	108
5.6.4	Consequences for Black Hole Formation	112
5.7	Summary	113
	Bibliography	116
	Appendix A	136

LIST OF FIGURES

	Page
2.1 The evolution to the equilibrium state of the G-dwarf planet with $e = 0$ receiving receiving $125\%S_0$, where S_0 is the modern solar constant (the instellation on modern day Earth): Mean global temperature (top), mean water mixing ratio (middle) and mass loss rate (bottom)	22
2.2 Top: Global mean surface temperature vs. increase in instellation in percent of the modern solar constant for a G-dwarf planet, using the standard EBM, the EBM modified to include a RGH parameterization, and the CAM4 GCM. Bottom: Comparison of the mean OLR between the three models. The CAM4 data is from Wolf and Toon <i>et al.</i> (2015)	29
2.3 The instellation range over which planets exhibit habitable surface conditions throughout their entire orbit (bright yellow region) shrinks with increasing eccentricities, but the emergence of a temporarily habitable zone (light blue region) helps to compensate for this reduction.	30
2.4 The range of instellations for which warm start planets orbiting M-,K-,G- and F-dwarf stars exhibit (non-zero) fractional habitability, as a function of orbital eccentricity.	32
2.5 Time to lose Earth's entire surface water inventory on aqua-planets orbiting M-dwarf AD Leo and G-dwarf star The Sun in Myr. The M-dwarf planet is exposed to $\sim 6x$ more XUV flux than the G-dwarf planet with an equivalent climate, leading to a $\sim 6x$ higher mass loss rate. The black contour outlines the boundaries of the moist greenhouse.	34
2.6 Fractional Habitability on the M-,K-,G- and F-dwarf planet with varying eccentricity and instellation, after EBM simulations assuming cold start conditions.	35
2.7 Warm - cold start difference in the fractional habitability on the M-,K-,G- and F-dwarf planet with varying eccentricity and instellation.	36
2.8 Fractional Habitability on an M-dwarf planet with $0^\circ, 45^\circ, 90^\circ$ obliquity, after EBM simulations assuming warm start conditions.	38
3.1 Mean surface temperatures as a function of stellar flux for the substellar, antistellar, and terminator regions of an Earth-sized planet orbiting M3V star AD Leo (blue) and M8V star TRAPPIST-1 (red). The freezing point of liquid water is marked with a horizontal dashed line for reference.	49

3.2	(a) The average day and night side top-of-model outgoing longwave radiation. (b) The average clearsky day and night side top-of-model outgoing longwave radiation. (c) The day and night averaged radiative cloud forcing (exact cloud positions not shown). The blue lines correspond to Earth-sized planets orbiting M3V star AD Leo, while the red lines correspond to Earth-sized planets orbiting M8V star TRAPPIST-1. The dashed vertical lines indicate the incident stellar fluxes at which the planetary night sides for both host-star spectral types fully deglaciate.	51
3.3	(a) The average night-side specific humidity. (b) and (c) The average day side (night side) low, medium, high and total cloud cover (%). Blue lines correspond to Earth-sized planets orbiting M3V star AD Leo, while red lines correspond to Earth-sized planets orbiting M8V star TRAPPIST-1. The dashed vertical lines indicate the incident stellar fluxes at which the planetary night sides for both host-star spectral types fully deglaciate.	53
4.1	The evolution of a $1.15 \times 10^9 M_\odot$ halo with either a $c_{200} = 19$ or 31 concentration, assuming a self-interaction cross section of $\sigma/m = 50 \text{ cm}^2/\text{g}$. The low-concentration halo, which collapses late in cosmological time, is generated for both $\kappa = 0.002$ and 0.02. The high-concentration halo, which collapses earlier, is only generated for $\kappa = 0.002$. The halo evolution is shown as a function of dimensionless time, normalized in terms of the thermal relaxation time of the halo, t_0 . The top axis provides the dimensionful time in Gyr. Top: The evolution of core density, ρ_{core} , normalized to the NFW scale radius, ρ_s . Note the two vertical axes: a linear (log) scale is used for densities below (above) $3\rho_s$. Results for the Spline, Kernel-Overlap, and Top-Hat SIDM implementations are shown in red, blue, and green, respectively. The solid (dashed) lines correspond to the high (low)-resolution simulations. Bottom: The evolution of velocity dispersion, v_{core} , normalized to the halo's maximum velocity, v_{max} . All plotted curves have been smoothed by averaging over the six nearest snapshots, which span about $10t_0$, with the exception of very early or late times where the halo evolution is rapid and no smoothing is necessary. For the high-resolution simulations, all three SIDM methods predict similar evolution during core formation, but diverge during core collapse. Specifically, the Spline method leads to the most rapid halo evolution, while the Top-Hat method leads to the slowest. The low-resolution simulations show considerable variation in the minimum density, which ultimately affects the core-collapse timescale. As discussed in Sec. 4.4.2, this is traced back to numerical noise in the initial conditions. Lastly, simulations with $\kappa = 0.02$ experience a failure at late times where core-collapse reverses, regardless of the SIDM method and resolution. These results pertain specifically to halos simulated with adaptive force softening for gravity.	71

4.2	The evolution of core density as a function of the total scattered mass for the high-resolution simulations with $\kappa = 0.002$. The solid opaque lines correspond to the low-concentration halo, while the dashed lines are for the high-concentration halo. The Kernel-Overlap and Top-Hat methods achieve the same core density at equivalent scattered mass, while the Spline method achieves the same core density with less scattering. These results pertain specifically to halos simulated with adaptive force softening for gravity. . . .	74
4.3	The collapse time, t_{coll} , in units of relaxation time plotted as a function of minimum core density, normalized to ρ_s . Results are shown for the low- (left panel) and high-resolution (right panel) simulation of the low-concentration halo with $\kappa = 0.002$. They are plotted for two different realizations of the NFW initial conditions of the halo (IC1 and IC2), shown by the empty/filled circles. For a given initial condition and SIDM method (indicated by color), each low-resolution halo is re-simulated three times to test reproducibility. The dominant source of scatter in the minimum core density and collapse time for the low-resolution simulations is the numerical noise in the generation of the initial conditions. These results pertain specifically to halos simulated with adaptive force softening for gravity.	75
4.4	Top: The evolution of total energy versus core density for the low-concentration halo with $\kappa = 0.002$ and 0.02 . Plotted in this space, the halo’s energy evolves clockwise with time. This evolution is characterized by a phase of core expansion at constant energy followed by the halo’s energy becoming more negative, i.e. losing thermal energy, from the time of core formation to core collapse. Simulations with $\kappa = 0.02$ exhibit a critical failure of energy conservation once core densities reach $50\text{--}500\rho_s$ (depending on SIDM method), where both the kinetic and potential energy is rapidly lost. Generally, the Spline method experiences this failure at much higher core densities than the other two methods. Bottom: The evolution of halo energy over time. For comparison, the evolution of a CDM halo is plotted in black. The Spline method produces energy evolution closest to the CDM halo at times past the “maximum core”, showing that this method produces the least net energy gain due to the DM scattering. These results pertain specifically to halos simulated with adaptive force softening.	79
4.5	The evolution of core density and energy of the low-concentration halo with fixed and adaptive force softening for gravity, using the Spline implementation. The particle smoothing h_s is adaptive. Additionally, the tolerance parameter, η , is varied. The simulation with fixed force softening and $\eta = 0.002$ exhibits much improved energy conservation relative to the others. The black line corresponds to the best-fit fluid model solution with $C = 0.84$, obtained by fitting to the simulation with best energy conservation.	83

5.1	The viscosity cross sections used in the simulations plotted as a function of relative velocity. For narrative purposes, the cross section are divided into two groups, the non-resonance and resonance-dominant. The former is composed of Yukawa cross sections together with two weakly resonating cross sections (i.e. $g \simeq 1$). Following the results from Refs. [229, 234] all cross section are normalised such that $K_5 = 16.5\text{cm}^2/\text{g}$ and should produce similar halo evolution for a given halo.	99
5.2	Left: The evolution of the core density for halo #2 and with interaction cross section $C0$, which is equivalent to halo BM2 from Ref. [232]. Right: The evolution of halo's total energy for all simulations listed in Table 5.1. We ensure that all simulations experience less than 1% deviations in halo's energy to limit the artificial cooling in the halo's core that occurs due to "bad" scattering events [173, 156].	100
5.3	The evolution of core density for halo #1 under the viscosity cross sections described in Table 1. Plotted in dashed line is the evolution under a constant, effective cross section $\sigma_{\text{eff}} = 16.5\text{cm}^2/\text{g}$ calculated using the method from Ref. [229]. Generally, the resonating cross sections (plotted in shades of red) tend result in faster halo evolution than σ_{eff} , while the Yukawa cross section evolve more slowly. Yukawa cross sections with $w \ll v_{\text{max}}$ deviate the most from the evolution expected from σ_{eff}	103
5.4	Core density at maximum core plotted against various velocity averaged cross section. Generally, ρ_{min} is more correlated lower powers of v_{rel} . We choose K_3/K_5 as the single variable to parameterize the halo.	104
5.5	Core density and time at maximum core plotted against the ratio of the velocity-averaged, K_3/K_5 , cross sections. The resulting fits to an exponential function are shown. Both the density and time at the maximum core exhibit rapid changes for $K_3/K_5 \leq 1$, but approach a constant at large K_3/K_5	105
5.6	Core size vs. core density at the maximum core stage. Each point corresponds to a simulation with a different cross section color coded as described in Table. 5.1. The dots are simulations of halo #1 and crosses are simulations of halo #2. The red points are simulations with resonant cross sections and these tend to evolve faster with smaller and higher density cores at the maximum core stage. Conversely, the blue points are non-resonating cross sections which evolve more slowly producing larger and lower density cores once the core is fully formalised.	105
5.7	Core collapse time as a ratio to the maximum core time versus K_3/K_5 , the velocity-averaged cross sections. The resulting exponential fit is shown. t_{coll} serves as a normalization timescale that produces universal halo evolution for any self-interaction cross section.	107
5.8	Halo evolution normalised by the collapse timescale t_{coll} and maximum core properties $\rho_{\text{min}}, t_{\text{min}}$ for all simulated cross section for halo #1. The resulting increases the agreement with the effective cross section σ_{eff} and removes any systematic deviations from universality due to differences in the cross sections.	108

5.9	<p>Left: Core density versus core size for all cross sections and both halos simulated in Table 5.2, 5.1. All exhibit approximately the same power law during core expansion $\alpha_e = 1.43 \pm 0.03$ and during core collapse $\alpha_c = 2.24 \pm 0.02$. Right: The core velocity dispersion versus core size. Both core expansion and core collapse exhibit a single power law with the corresponding α that is generally cross-section independent.</p>	109
5.10	<p>Halo density profile at equivalent times in the halo evolution for the cross sections C7 (constant) and R8 (the cross section most dominant at $v_{\text{rel}} \gg v_{\text{max}}$). The differences in the core density are relatively small prior to core collapse, and the outer halo profiles are identical at equivalent times in the halo evolution. However, the differences in the core densities grow far into core collapse due to the remaining scatter in the core collapse time in our analytic fits.</p>	110
5.11	<p>Left: Halo core mass as a function of core velocity dispersion squared for a simulation sample with a constant, resonant and monotonic cross sections. The analytic prediction for the mass evolution in the LMFP regime is plotted for reference in the black dashed line. Eventually all simulations deviate as they enter the SMFP regime and the core begins to shed less mass as the temperature increases. Right: The ratio of the LMFP to SMFP heat conductivity for the halo's core. Despite initially lower core mass exhibited by cross sections that dominate at $v_{\text{rel}} > v_{\text{max}}$, the R8 cross section transitions to the SMFP regime at a larger core mass compared to cross sections that dominate at $v_{\text{rel}} < v_{\text{max}}$, which could lead to a relatively higher mass black hole once the relativistic instability is reached.</p>	112

LIST OF TABLES

		Page
2.1	The temperature regimes and corresponding average water mixing ratios used in our simulations with an EBM with a runaway greenhouse parameterization.	21
2.2	Stellar and planetary parameters used as input to the EBM, including broad-band planetary albedos from Shields <i>et. al</i> (2013) and incident XUV fluxes from Airapaitian <i>et. al</i> (2017) and Chadney <i>et al.</i> (2015).	27
4.1	Halo and simulation parameters used in this work, including the concentration ($c_{200} = R_{200}/r_s$), NFW scale radius (r_s) and density (ρ_s), number of particles (N_p), force-softening length for gravitational ($h_{g,i}$) and self ($h_{s,i}$) interactions, time-stepping criterion (κ), and tolerance parameter (η). The parameter κ corresponds to the maximum probability that two particles scatter with each other in a given time step and is defined in Sec. 4.3.3. The parameter η captures the fraction of the gravitational softening length that a particle can travel in a specified time step; it is discussed in Sec. 4.3.2. All of the listed configurations are simulated using the three SIDM methods described in Sec. 4.3.1: Kernel Overlap, Spline, and Top Hat.	62
5.1	Halo parameters	98
5.2	Cross section parameters.	98

ACKNOWLEDGMENTS

I would like to thank Manoj Kaplinghat for his mentorship and encouragement. Thank you for your easy-going nature, openness and patience. Our long research discussions were not only fun but also a crucial element of my academic journey. I am grateful to Aomawa Shields for teaching me about so much more than research. Over the years I have worked with many fantastic academics, who have mentored me along the way. Thanks to Andrew Rushby for teaching me the ropes in the early years of my PhD and for always being there to answer my questions. To Russell Deitrick, Eric Wolf and Victor Robles for teaching me about the art of physics simulation. To Mariangela Lisanti and Oren Slone for helping me shape my ideas into coherent publications.

I would like to thank my family and friends for their unwavering support over my entire academic journey. Special thanks go to my partner Alex, and my mom, the two people without whom none of this would be possible. I would like to thank Dylan, Geoff, Julie-Ann, Edmund, Sophia, Vidya, Courtney, Gordon, Ben, Rob, Brie and Bederic for sharing this journey together while making joyful memories along the way. Thanks to Lila for being the best feline friend I could ask for. I would also like to thank my entire 2017 cohort and, office mates and my entire research group for inspiration and good company.

Thanks to the department of Physics and Astronomy for providing such a supportive environment to thrive in. Thanks to everyone who taught courses where it was truly exciting to learn. Thanks to numerous Professors and teachers that have instilled the love for math and science in me over the course of my life.

VITA

Igor Zbigniew Palubski

EDUCATION

Doctor of Philosophy in Physics University of California, Irvine	2024 <i>Irvine, CA</i>
Master of Science in Physics University of California, Irvine	2022 <i>Irvine, CA</i>
Bachelor of Science in Physics (minors in Math & Astronomy) Iowa State University	2017 <i>Ames, IA</i>

RESEARCH EXPERIENCE

Graduate Research Assistant University of California, Irvine	2018–2024 <i>Irvine, California</i>
--	---

TEACHING EXPERIENCE

Teaching Assistant University of California, Irvine	2017–2024 <i>Irvine, CA</i>
Teaching Assistant Iowa State University	2016–2017 <i>Ames, IA</i>
Learning Assistant Iowa State University	2015–2016 <i>Ames, IA</i>

REFEREED JOURNAL PUBLICATIONS

- Limits of Analytic Theory—Gravothermal Evolution of SIDM Halos Under Velocity-Dependent Interactions** 2024
JCAP (in-prep)
- A toolbox for predicting signals of self-interacting dark matter halos** 2024
JCAP in-prep
- Numerical Challenges in Modeling Gravothermal Collapse in Self-Interacting Dark Matter Halos** 2024
JCAP (in-review)
- Terminator Habitability: the Case for Limited Water Availability on M-dwarf Planets** 2023
ApJ
- The Eccentric Habitable Zone: Habitability and Water Loss Limits on Eccentric Planets** 2022
ApJ
- Imaging the Localized Plasmon Resonance Modes in Graphene Nanoribbons** 2020
ApJ
- Global Energy Budgets for Terrestrial Extrasolar Planets** 2019
ApJ Letters

OTHER PUBLICATIONS

- Red-dwarf Habitability Recipe** 2019
August issue of Sky and Telescope

ABSTRACT OF THE DISSERTATION

Simulations of Runaway Processes in Astrophysics

By

Igor Zbigniew Palubski

Doctor of Philosophy in Physics

University of California, Irvine, 2024

Professor Manoj Kaplinghat, Chair

Numerical and N-body simulations are used across astrophysics in problems ranging from the small—modeling stellar winds, or planetary atmospheres—to the large—in simulations of large patches of cosmos or individual galaxies. Applications studied in this dissertation span this entire range of scales of the cosmos and include the exploration for alternate states of habitability on extrasolar planets, and modeling gravothermal collapse in Self-Interacting-Dark-Matter (SIDM) halos. I develop simulation codes to study planetary habitability on the edge of the runaway greenhouse and (runaway) core collapse in DM halos that galaxies reside in. A variety of common code implementations for SIDM N-body simulations is tested and numerical effects are outlined for typical usages of such codes. With these models, the Eccentric Habitable Zone (EHZ) is constrained for wide range of planetary orbits, and I present a set of equations to predict the evolution of SIDM halos under any velocity-dependent self-interaction cross section. Additionally, we explore the potential for a new planetary habitable state we termed "Terminator Habitability" on water rich planets.

Chapter 1

Introduction

Complexity of modeling is growing rapidly in the 21st century and the range of applications grow. As complexity rises so does the computational cost and numerical problems that necessitate innovation in this space.

1.1 The Habitable Zone

The discovery of the first planet orbiting a main sequence star [132] transformed both astronomy and planetary science, providing a shared foundation for these disciplines. This groundbreaking finding also contributed to the emergence of a new field: astrobiology, the study of life and its place in the universe. Consequently, the prospect of discovering extraterrestrial life appeared more attainable than ever before. Nearly 30 years later there are now more than 7000 confirmed exoplanets, around 200 of which are terrestrial ¹. Majority of these planets were discovered by NASA's monumental Kepler mission [17], which was in operation between 2009 and 2018. More recently, the Transiting Exoplanet Survey

¹NASA Exoplanet Archive, accessed August 2, 2016, <http://exoplanetarchive.ipac.caltech.edu>

Satellite (TESS) mission [171] has searched for exoplanets in our galactic neighborhood and found thousands of planet candidates mostly within 300pc of Earth². Nevertheless, several obstacles persist in the quest to identify habitable planets and extraterrestrial life. These encompass technological challenges, such as the need for improved detectors, larger apertures, and data analysis techniques[60]. Additionally, there are theoretical challenges: determining how to identify a habitable planet, given that we have only one known example to study [136, 182, 183]. To answer this question, we typically begin with the concept of the habitable zone, and the extensions of thereof.

The habitable zone (HZ) is one of the most popularized terms in all of astronomy. It is a region around a star in which Earth-like planets can maintain liquid water on the planetary surface. One can immediately see the shortcoming of this definition. An Earth-like planets means one on a nearly perfect circular orbit, planetary obliquity of about 23° with about a 1-bar atmosphere, dominated by nitrogen gas, carbon dioxide and water, and a surface dominated by oceans. Initially, this concept was used only for stars like the Sun, main-sequence, G-dwarf stars, but was expanded to include F-, and M-type stars [96], however it is a very specific with respect to the planetary parameters. The HZ does not consider alternative atmospheres, or orbital configurations. It does not take into account habitability of moons, or subterranean life such as what might exist on Mars, or the icy moons of Jupiter Europa, or Enceladus. These moons, while much to distant to the Sun to receive enough solar energy to sustain life, are continuously warped by the tides of Jupiter, heating them and potentially thawing out entire oceans below their icy surface [135, 213].

The inner boundary of the HZ is defined by the "moist greenhouse" limit, while the outer edge is defined by the "maximum greenhouse" limit. At the inner boundary of the habitable zone, the surface temperature must remain sufficiently low to allow for the stability of liquid water. However, the planet's upper atmosphere may become warm enough to prevent water vapor

²NASA Exoplanet Archive, accessed August 2, 2016, <http://exoplanetarchive.ipac.caltech.edu>

from being confined within the troposphere. Once water vapor reaches the stratosphere, it is photolyzed, breaking it down into H_2 and O . Subsequently, the light hydrogen gas slowly escapes the gravitational pull of the planet, making the loss of water vapor irrecoverable. This is a more conservative limit compared to the "runaway greenhouse" limit, where the surface temperatures reach a point where all of the water on the planet evaporates and the atmosphere becomes saturated with water vapor.

The outer boundary of the habitable zone is determined by the maximum greenhouse warming a planet can achieve through CO_2 . As CO_2 pressure increases, it warms the planet, allowing it to remain habitable at lower stellar fluxes. However, when CO_2 pressure exceeds approximately 8 bars, the enhanced planetary albedo due to Rayleigh scattering counteracts the greenhouse effect, causing the planet to cool [108]. The outer edge of the habitable zone is thus identified by setting the CO_2 pressure to this maximum level and decreasing the stellar flux until the planet freezes [96].

As an extension to the traditional HZ, the habitability of Earth-like planets with different orbital configurations has been considered. Ref. [11, 42] first considered the impact of orbital eccentricity and found that the HZ is effectively extended for eccentric planets. This can be understood by the simple fact the annually average stellar radiation, hereafter "instellation", a planet receives increases with higher orbital eccentricity. On the other hand, such planets can experience global winters at the apoastron, where the amount of energy received from the star is at minimum. This scenario poses a challenge for life that may inhabit such planets, but does not exclude the possibility of life altogether. The interplay between orbital parameters and the HZ is discussed further in Chapter 2 where a modified 1-dimensional Energy-Balance-Model (EBM) employed to explore a wide range of orbital parameters and host star types.

Another possibility not captured by the usual definition of the HZ is an alternate habitable state, where only a portion of the planet maintains temperature amenable for liquid water.

For example, on synchronously rotating planets, where one side of the planet is always facing the star, it may be possible to form a thick, reflective cloud cover at the sub-stellar point, while at the anti-stellar point of the planet the temperature are below the freezing point of water. In such an extreme scenario the runaway greenhouse is staved off by this thick cloud cover. Liquid water could be present around the terminator region of the planet even if the planet was too close to the host star to be within the traditional habitable zone. This scenario is explored in Chapter 3, where a 3-dimensional general-circulation-model (GCM) is employed to study this phenomenon on water-rich planets.

1.2 Dark Matter and Tensions in Modern Cosmology

1.2.1 Dark Matter and Λ CDM Cosmology

Cosmology, the study of the universe's origins, structure, evolution, and ultimate fate, has made tremendous strides over the past century. The current standard model in cosmology, known as Lambda Cold Dark Matter (Λ CDM), has been instrumental in shaping our understanding of the universe. This model incorporates two dominant components: the cosmological constant (Λ), which represents dark energy, and Cold Dark Matter (CDM). Dark energy comprises about $\sim 68\%$ of the mass-energy content of the universe, dark matter $\sim 27\%$, while the baryonic matter we are more accustomed to, is only $\sim 5\%$ of the universe mass-energy content.

Dark matter and dark energy are the most mysterious components of the Λ CDM model. Dark matter is a form of matter that does not emit, absorb, or reflect light, making it invisible to telescopes. Instead, dark matter is detected through its gravitational effects on visible matter, radiation, and the large-scale structure of the universe. Dark energy is thought to be responsible for the observed accelerated expansion of the universe. Its exact nature remains

unknown, but it is often modeled as a constant energy density filling space homogeneously. Together, dark energy and dark matter are chiefly responsible for the large-scale structure of the universe and its observed expansion.

The Λ CDM model posits that the universe began in an extremely hot and dense state approximately 13.8 billion years ago, an event known as the Big Bang. Following the Big Bang, the universe underwent a brief period of rapid expansion known as cosmic inflation. During inflation, the universe expanded exponentially, leaving it nearly perfectly homogeneous and setting the stage for the formation of large-scale structures such as galaxies and clusters of galaxies. In locations of overdensity, dark matter would begin to collapse under gravity, starting the process of galaxy formation. The evidence for existence of dark matter comes from nearly a century of direct and indirect observations and these are outlined in the following section.

1.2.2 Evidence for Dark Matter

The existence of dark matter is supported by a variety of observational evidence across different scales, from the rotation curves of galaxies to the dynamics of galaxy clusters and the properties of the CMB. One of the earliest pieces of evidence for dark matter comes from the study of galaxy clusters, the largest gravitationally bound structures in the universe. In the 1930s, Fritz Zwicky observed that the mass of the Coma cluster, inferred from the velocities of its member galaxies, far exceeded the mass estimated from the visible light emitted by the galaxies [244]. Zwicky coined the term "dark matter" to describe this missing mass.

In the 1970s, astronomer Vera Rubin and her collaborators measured the rotational velocities of stars in spiral galaxies. According to Newtonian mechanics, the rotational velocity of stars should decrease with distance from the galactic center, similar to how planets in the solar

system orbit more slowly as they move farther from the Sun. However, Rubin's observations revealed that the rotational velocities of stars in galaxies like Andromeda remained nearly constant, even at large distances from the galactic center [178]. This discrepancy suggested that all galaxies are embedded in dark matter envelopes, or halos, whose mass far exceeds that of the visible matter. Nearly fifty years later, the nature of Dark Matter remains elusive but it is commonly thought to be a novel particle leftover from the Big Bang, whose interactions with the visible matter are either very weak or non-existent [165].

Gravitational lensing provides the means to observe dark matter directly. When light from a distant object, such as a galaxy or a quasar, passes near a massive object like a galaxy cluster, the light is bent by the gravitational field, creating multiple images or distorted arcs. The amount of lensing depends on the total mass of the lensing object, including both visible and dark matter. One of the most striking examples of gravitational lensing is the Bullet Cluster, a collision between two galaxy clusters. Observations of the Bullet Cluster show a clear separation between the visible matter, primarily in the form of hot gas detected by X-ray observations, and the dark matter, inferred from gravitational lensing. This separation provides strong evidence for the existence of dark matter and its collisionless nature [30].

The CMB, the relic radiation from the Big Bang, offers further support for the Λ CDM model and the presence of dark matter. The CMB exhibits tiny temperature fluctuations that correspond to density variations in the early universe. These variations, mapped by missions like the Wilkinson Microwave Anisotropy Probe (WMAP) and the Planck satellite, provide a snapshot of the universe when it was just 380,000 years old [199]. The patterns of these fluctuations are influenced by the amount and distribution of dark matter. By analyzing the CMB, cosmologists can infer the universe's overall composition, including the proportions of dark matter and dark energy. The Λ CDM model provides an excellent fit to the observed CMB data, reinforcing the case for dark matter's existence [199, 160].

Despite its remarkable accuracy in the description of the universe, the Λ CDM model faces

several notable challenges, particularly on the scales of small, or satellite galaxies. These challenges, often referred to as the "small-scale crisis," include the missing satellites problem, the cusp-core problem, and the diversity problem and may hint at additional physics not captured by the Λ CDM framework. One such modification postulates that dark matter particles may scatter with one another via a new non-gravitational interaction. This Self-Interacting-Dark-Matter model (or SIDM) is proving to be one of the most promising solutions to the small-scale crisis. In the following section, the challenges facing Λ CDM cosmology are outlined and the SIDM model is described

1.2.3 The "small scale crisis" in Cosmology

The Missing Satellite Problem

The missing satellites problem arises from the discrepancy between the number of small satellite galaxies predicted by Λ CDM simulations and the number observed around galaxies like the Milky Way. Simulations suggest that large galaxies like the Milky Way should be surrounded by hundreds of smaller, satellite galaxies. However, only a few dozen satellite galaxies have been observed around the Milky Way, leading to questions about the accuracy of the Λ CDM model on small scales [100, 143, 102].

Several solutions have been proposed to address this discrepancy. One possibility is that many of the predicted subhalos are low in baryon content and therefore too faint to be detected with current observational techniques. Processes such as supernova feedback and photoionization of the galactic gas content could disrupt star formation or strip away the stars in these small halos [47, 23, 38].

However, in recent years, the number of faint satellite galaxies has increased significantly [221, 133, 44, 114, 204, 43]. Now, over 50 satellite galaxies of the Milky Way are known, with

estimates suggesting that 3-5 times more may yet be discovered [74, 43]. Furthermore as our understanding of reionization and the effects of stellar feedback on star formation has improved [25, 79, 205, 64, 80], the theoretical predictions for the number of luminous satellites has fallen. Consequently, the missing satellites problem is no longer seen as a significant issue. Instead of indicating a need for non-standard dark matter, the observed number of satellites now helps rule out dark matter models that would eliminate too much substructure [129, 18].

The Too-Big-To-Fail (TBTf) Problem

Ref. [19] conducted a comparison between local dwarf galaxies and simulations involving only CDM. They found that the most massive dark matter substructures around simulated halos resembling the Milky Way were significantly more massive than the dwarf galaxy masses inferred from line-of-sight velocity measurements [216, 225]. If this prediction is correct, such large satellites would have to be severely lacking in luminous matter i.e stars. Intriguingly, we should expect the opposite from such massive halos. Due to their deep gravitational potential, the impact of photoionizing feedback, which would inhibit gas accretion and consequently star formation should be weaker relative to smaller subhalos, making these massive galaxies too-bit-to-fail at forming stars.

There has been several proposals for solutions to this problem that preserve the Λ CDM framework. An overestimation of the mass of the MW halo would translate to an overestimation of the masses of the subhalos [19, 20]. Baryonic effects can also play a role. Intense gas outflows, such as those driven by supernovae, can induce rapid fluctuations in the gravitational potential, which in turn transfer energy to dark matter particles and result in a reduction of the central DM density [162, 69, 149, 63]. Reduced DM density in turn leads to the outflow of luminous mass from the DM subhalo. However, others point out that the supernovae in MW dwarfs are not energetic enough to blow out nearby DM to solve the TBTf problem [63]. The loss of baryon mass due to other baryonic processes: reionization,

ram pressure or tidal stripping could explain the TBTF problem in satellites, but not in isolated, field galaxies, which also experience a TBTF problem [63, 101, 157, 64]. Additionally, it's unclear if solutions invoking purely baryonic effects can simultaneously explain the kinematic properties of NW dwarfs [175, 94].

The Cusp-Core Problem

The cusp-core problem refers to the difference between the predicted and observed density profiles of dark matter in the centers of galaxies. Λ CDM simulations predict that dark matter halos should have a steep, cuspy central density profile, with $\rho \propto r^{-1}$ [147]. However, observations of dwarf galaxies and low surface brightness galaxies show that these galaxies are better fit by shallower, cored profiles with lower central densities [57, 134, 125, 196, 151, 176, 152, 22].

Proposed solutions to this tension include baryonic processes such as supernova-driven gas outflows, which can redistribute dark matter and create a cored profile [243, 203, 118, 179]. Additionally, observational biases in stellar velocity dispersion, and neglecting gas pressure can lead to inferring a fictitious core [159]. However, these have not been able to fully alleviate this tension to date. SIDM offers another possible solution. Self-interactions provide a mechanism for heat and mass transfer within the DM halo. In general this leads to thermalization and coring of the density profiles in the galactic center [48, 179].

Diversity Problem

In the Lambda Cold Dark Matter model, the hierarchical formation of structures results in halos that follow a self-similar pattern, typically described by Navarro-Frenk-White (NFW) profiles [147]. The parameters of these halos, the density scale (ρ_s) and the scale radius (r_s), are closely linked, meaning that a single parameter can define a halo. For instance, once

the maximum circular velocity (V_{max}) is determined, the entire density profile of the halo, including the inner density cusp, is specified. However, this is not generally the case for observed dwarf galaxies, which exhibit little correlation between V_{max} and ρ_s and significant diversity in their inner rotation curves [113]. The central density of galaxies of similar V_{max} can vary by as much as an order of magnitude [113, 153]. Therefore, any explanation for the core-cusp problem must also account for this observed diversity. This diversity could result from inaccurately measured distances and inclinations of the dwarf galaxies [154, 167]. Nonetheless, if dwarf galaxies indeed exhibit diverse rotation curves, the Λ CDM cosmology would require significant revision [90, 169]. Introducing DM self-interactions naturally produces more diverse rotation curves regardless of the details of particle physics. In the following section, the SIDM model is discussed in more detail.

Self-Interacting Dark Matter

In response to the challenges faced by the Λ CDM model, alternative theories of dark matter have been proposed. One such theory is Self-Interacting Dark Matter (SIDM), which posits that dark matter particles interact with each other through forces other than gravity [198]. These self-interactions can have significant effects on the structure and dynamics of dark matter halos, potentially resolving some of the small-scale issues in the Λ CDM model. Through energy and mass redistribution DM particle interactions can alter the central density of DM halos and make halos more spherical as the DM particle velocity distribution becomes more isotropic [198, 24, 235]. The initial motivation for SIDM came from the aforementioned small-scale challenges in standard cosmology. For a wide range of scattering cross sections, SIDM can alleviate most of these issues while preserving the large-scale successes of Λ CDM cosmology (see Ref. [206] for a review).

The initial enthusiasm for SIDM stemmed from its capacity to generate constant density cores in dwarf galaxies [198, 235] and diminish the extent of substructure in dark matter

halos, thereby addressing the core-cusp and missing satellites problems. The reduction of substructure is thought to be the result of host-subhalo DM interactions. As a subhalo orbits its host, its DM particles will scatter with the more extensive halo of the host often causing the subhalo particles to be kicked out of the subhalo’s gravitational potential, thereby reducing its mass. Depending on the subhalo’s orbit and the SIDM cross section, this effect can be strong enough to fully disrupt a subhalo in a single orbit, leaving its entire mass content to be consumed by the host. This can significantly reduce the number of expected subhalos around a host galaxy like the Milky Way. While it remains unclear if the missing satellite problem remains in the light of more recent studies [204, 145, 99], the number of MW satellite predicted by SIDM remains a constraint on the interaction cross section. Similarly, SIDM naturally solves the TBTF problem. With the decreased central densities in SIDM halos, the circular velocity profiles of galaxies inhabiting these halos are also reduced [48, 174, 175, 145, 195]. This adjustment results in SIDM simulations aligning more closely with stellar velocity dispersion measurements compared to simulations that only involve Cold Dark Matter (CDM).

It has also been suggested that SIDM can explain the diversity problem [92, 48]. The interplay between a baryonic disk and its surrounding DM halo can induce minor alterations in the baryonic component of a dwarf galaxy, resulting in significant changes to the overall density profile [92, 48, 34, 174, 175, 195]. SIDM can either enhance or reduce the central density of dark matter in the presence of baryons, contingent upon the concentration of the baryonic component. If the baryonic mass is concentrated, the central density of DM can be higher relative to CDM, while the opposite is true if the baryonic mass is more diffuse. In the case of highly concentrated baryonic matter with SIDM, the DM core can contract and “core collapse,” producing a very small and dense core with a steep outer profile [103, 9, 8, 104]. Core collapse in the absence of baryons requires a higher cross section, but can occur for several MW dwarfs for cross sections $\sigma/m \sim 30-100 \text{ cm}^2/\text{g}$ at the velocity scales MW dwarfs [32]. Recently, it has been suggested that such a high cross section is necessary to explain

the diversity problem in the MW dwarfs even after taking into account baryonic feedback processes that can alleviate the TBTF problem [154, 195]

Outside of the small-scale evidence for SIDM, observations of galaxy clusters suggest there is a small self-interaction cross section of $\sim 1 \text{ cm}^2/\text{g}$ at these mass/velocity scales. This can be inferred from the offsets between the DM halos and the galaxies they host [142, 131, 173]. An offset of this nature might result from a system not in equilibrium or from dynamic influences such as tidal forces or dynamical friction varying between stars and dark matter due to differences in their respective mass distribution. However, such offsets seem to be uncommon in a CDM universe [181]. Alternatively, and more directly, evidence for such a small SIDM cross section can be inferred from the DM density profiles derived through strong gravitational lensing of galaxy clusters [93, 5, 4].

There are examples of star-poor substructures, of mass $\sim 10^9 M_\odot$, only detected through gravitational lensing, which exhibit remarkably high central density and a steep central density slope reminiscent of a collapsed DM halo [141, 35]. These substructures provide additional evidence for a large self-interaction cross section at the velocity scales of dwarf galaxies entirely in the absence of baryonic mass, which could provide an alternative explanation for the existence of such centrally dense substructures. Given, the importance of core collapse to explain the full range of tensions with Λ CDM cosmology, necessary tools have been developed and tuned to model this phenomenon accurately. In Chapter 4, a comparison between common N-body SIDM implementations is performed. Key model parameters for modeling core collapse are discussed as well as resolution effects and their impacts on simulation results.

Given the wealth of evidence for an SIDM cross section that varies strongly at different mass/velocity scales, in the recent years, there has been an increased interest in velocity-dependent SIDM [93, 214, 237, 145, 210, 232]. The velocity-dependent model often invoked for SIDM is a t/u-channel Yukawa interaction, mediated by a light mediator [14, 206]. This

interaction exhibits a desired steep velocity dependence $\approx v^{-4}$ above a characteristic velocity scale, making it easy to fit to both the dwarf galaxy and galaxy cluster data. However, observations do allow for a resonant cross section for as long as it preserves a strong velocity dependence at large velocities [28]. In Chapter 5, SIDM halos subjected to a variety of Yukawa and resonant cross sections are examined and a set of parametric equations that are functions of only one variable derived from the cross section are presented.

Chapter 2

Habitability and Water Loss Limits on Eccentric Planets Orbiting Main-Sequence Stars

2.1 Abstract

A planet's climate can be strongly affected by its orbital eccentricity and obliquity. Here we use a 1-dimensional energy balance model modified to include a simple runaway greenhouse (RGH) parameterization to explore the effects of these two parameters on the climate of Earth-like aqua planets —completely ocean-covered planets— orbiting F-, G-, K-, and M-dwarf stars. We find that the range of instellations for which planets exhibit habitable surface conditions throughout an orbit decreases with increasing eccentricity. However, the appearance of temporarily habitable conditions during an orbit creates an eccentric habitable zone (EHZ) that is sensitive to orbital eccentricity and obliquity, planetary latitude, and host star spectral type. We find that the fraction of a planet's orbit over which it exhibits

habitable surface conditions is larger on eccentric planets orbiting M-dwarf stars, due to the lower broadband planetary albedos of these planets. Planets with larger obliquities have smaller EHZs, but exhibit warmer climates if they do not enter a snowball state during their orbits. We also find no transient runaway greenhouse state on planets at all eccentricities. Rather, planets spend their entire orbits either in a RGH or not. For G-dwarf planets receiving 100% of the modern solar constant and with eccentricities above 0.55, an entire Earth ocean inventory can be lost in 3.6 Gyr. M-dwarf planets, due to their larger incident XUV flux, can become desiccated in only 690 Myr with eccentricities above 0.38. This work has important implications for eccentric planets that may exhibit surface habitability despite technically departing from the traditional habitable zone as they orbit their host stars.

2.2 Introduction

With the rapidly expanding catalog of discovered exoplanets, much effort will be dedicated to characterizing these planets and identifying those that may be habitable—that is, possessing conditions conducive to the presence of liquid water [96, 106, 185]. Habitability is strongly dependent on many stellar, orbital, and planetary parameters [136, 189]. A first-order approach to identifying a potentially habitable planet is to pinpoint one that orbits within the boundaries of its host star’s habitable zone—the region around a star where a planet with an Earth-like atmosphere may be warm enough for liquid water to flow on its surface [96]. The inner edge of the habitable zone (IHZ) is determined by the onset of the runaway greenhouse, a climate state in which the atmosphere becomes opaque to outgoing thermal (longwave) radiation, inhibiting a planet’s ability to cool and desiccating the surface, leaving zero water content on the planet. At the outer edge of the habitable zone (OHZ), determined by the maximum CO₂ greenhouse (GH) limit, any further addition of CO₂ into the atmosphere will no longer keep surface temperatures above the freezing point of water. [96, 158, 108, 107].

However, the traditional boundaries of the habitable zone are based on the assumption of Earth-like planetary conditions and do not take into account the range of orbital eccentricities or obliquities possible in extrasolar planetary systems. The large variations in orbital distance from their stars of highly eccentric planets may generate significant changes in surface temperature, creating intervals of habitable surface conditions interspersed with climate extremes during an orbit, defying traditional habitable-zone calculations [124]. Similarly, large planetary obliquities lead to larger seasonal variations in the stellar flux latitudinal pattern, which in turn can drastically affect a planet’s climate and possibly push it permanently into a snowball state. Counter to the climatic state of present Earth, at an obliquity of 23.44° , if a planet’s obliquity is 54° or greater (220), the polar regions receive more stellar flux and tend to be warmer than the equatorial regions, leading to the formation of ice belts—ice covered regions that extend from the equator poleward. Below this threshold ice caps—ice-covered polar areas of a planet—are formed instead. In general, increasing obliquity destabilises the ice caps, i.e., at higher obliquities, ice caps collapse to the equator at higher values of stellar flux [177]. Similarly, on planets with obliquities higher than 54° , the corresponding ice belts collapse towards the poles. A planet’s temporal habitability—defined here as any fraction (< 1) of the orbital period over which habitable conditions are present—as a function of its orbital eccentricity has not previously been quantified. Temporarily habitable planets may experience a snowball or a runaway greenhouse (RGH) state over a significant portion of the orbit but are habitable for its remainder. Surface life on such planets would likely have to seek shelter through a RGH period and/or hibernate through a snowball period. The survival of subsurface life through a snowball episode will depend on the thickness of sea ice. If ice grows to a few hundred meters or more, photosynthesis will not be possible. However, if it remains thin, or if there exist some oases—small deglaciated regions—life may survive these snowball episodes [2].

Many confirmed exoplanets are on eccentric orbits (see, e.g., 111, 146, 85, 65, 73, 91, 222, 21). At the time of writing, $\sim 50\%$ of these have orbital eccentricities $e > 0.1$ and $\sim 10\%$ have $e >$

0.5.¹ Previous studies on the effects of eccentricity on the habitability of an Earth-like planet orbiting a Sun-like star found that such planets may have liquid water on the surface even at high eccentricities [219, 42]. These studies determined that the habitability of an eccentric planet may be approximated by the annually-averaged stellar flux received by the planet, which may correspond to a distance that is within the boundaries of the traditional habitable zone [219]. High eccentricity may therefore help planets maintain habitable surface conditions near or even outside of the OHZ [108, 107], though the highest eccentricities have been shown to induce cyclic snowball climate behavior [15]. And smaller gaseous, “mini Neptune” exoplanets on eccentric orbits may undergo photoevaporation of their hydrogen/helium envelopes, revealing potentially habitable Earth-mass planets [127]. Similarly, obliquity has been shown to have a significant impact on planetary climate. Large obliquity may pose difficulties for habitable climates due to ice instabilities, but high-obliquity habitable Earth-like planets are possible [218, 200, 7, 55]. These studies underscore the importance of quantifying the effects of extreme orbits on planetary habitability.

The climatic effect of eccentricity has been studied using a one-dimensional (1-D) energy balance model (EBM) [42]. Planets have been found to remain habitable for a range of eccentricities, and when initially frozen, thaw if perturbed to a higher eccentricity [42]. However, this work did not include a parameterization to simulate the runaway greenhouse state to which highly eccentric planets are susceptible at periastron (closest approach to the star), nor did it quantify temporal habitability as a function of the spectral energy distribution (SED) of a planet’s host star. Planets in a runaway greenhouse state have surface temperatures exceeding the critical point of water (647 K), leading to complete evaporation of their oceans. Since there is no cold trap at such extreme temperatures, all water vapor rises unrestrictedly into the upper layers of the atmosphere, where it can be photolyzed. While hydrogen more easily escapes to space, oxygen may remain behind to form ozone, to oxidize the surface, or to build up O₂-rich atmospheres that may present a

¹The extrasolar planets encyclopedia. (<http://www.exoplanet.eu/>)

false positive signature for life [228, 126].

An existing complication to the potential habitability of M-dwarf planets remains the extreme activity of their host stars [180, 202, 190]. M-dwarfs emit strongly in the X-ray (0.1-12 nm) and extreme UV (12-1000 nm) regions of the electromagnetic spectrum (hereafter “XUV”). XUV photons can drive the gravitational escape of atmospheric constituents [126, 115, 50, 116]. Stellar winds, coronal mass ejections, and flare activity can exacerbate these effects [115, 98, 150]. Planets with sufficiently large water mixing ratios in the atmosphere are particularly susceptible to desiccation of their surfaces given host stars with high amounts of XUV flux.

For this study we use a 1-D, latitudinally resolved EBM with an explicit sea ice model and a RGH parameterization to investigate the effects of eccentricity and obliquity on the climate and habitability of terrestrial aqua planets—completely ocean-covered planets—orbiting F-, G-, K-, and M-dwarf stars. The eccentric habitable zone (EHZ) considers the orbit-averaged flux as the main predictor of habitability on eccentric planets [11]. The EHZ compares the orbit-averaged flux on an eccentric orbit to the flux values within the classical habitable zone, which corresponds to a circular orbit. Here, we refine the definition of the EHZ to include the effects of strong seasonality. Previous work found that planets orbiting cool, lower-mass, M-dwarf stars, whose SEDs peak at longer, redder wavelengths, are more stable against global glaciation, and thaw out of such states at lower levels of incoming stellar radiation (hereafter “instellation”) compared with planets orbiting hotter, more luminous stars with more visible and near-UV output [193, 191]. The effect of host star SED on the climate and habitability of eccentric planets may therefore be significant, and has not yet been constrained. While Barnes *et al.* (2008) calculated the EHZ as a function of effective stellar temperature, an exploration of the climatic effect of host star spectral energy distribution (SED) was not included.

We account for periods of both snowball and moist/runaway greenhouse and calculate the

fraction of the planetary surface that has clement conditions for liquid water throughout its orbit. We do this for planets orbiting stars of different spectral type, assuming a fixed (Earth-like) amount of atmospheric CO_2 . We also calculate the full-orbit EHZ, which corresponds to planets that exhibit habitable conditions over the entire orbit. Lastly, we calculate the water loss rates for planets in an eccentricity-instellation parameter space where they are subject to both runaway and moist greenhouse states. We compare the timescales for these planets to lose an entire Earth ocean inventory as a function of their host star spectral type.

In Section 2 we describe the modifications made to the EBM to implement the RGH parameterization, as well as the model we use to calculate the water loss rates for different stellar XUV fluxes. In Section 3 we present the results in the form of EHZ instellation ranges, habitability fractions, water loss rates, and ocean loss timescales, as a function of eccentricity and host star SED. In Section 4 we discuss the implications of this work for the habitability of planets whose orbits take them interior to and well outside of the traditional boundaries of the habitable zone. Conclusions follow in Section 5.

2.3 Methods

We use a 1-D Energy Balance Model (EBM), based on North and Coakley (1979), that has been used to explore the potential climates of exoplanets in previous work [193]. This seasonally varying model balances the absorbed incident stellar energy flux with the outgoing longwave flux and horizontal heat diffusion at all latitudes. As a 1-D latitudinal model that averages over longitudes, the EBM inherently applies best to rapidly rotating planets. Here we assume that our modeled planets are rapidly rotating like the Earth, where the rotational frequency is much larger than the orbital frequency. The original model was modified to include a latitudinally-varying diffusion coefficient that adjusts tropical heat transport to generate temperatures consistent with thermal wind observations [123]. Our EBM includes

an explicit sea ice model, where the ocean is allowed to freeze once temperatures drop below -2°C , producing either ice caps or ice belts, depending on planetary obliquity. The model incorporates the energy flux between the ocean and ice but no ice dynamics.

The outgoing longwave radiation (OLR) is linearly parameterized with surface temperature based on the effects of CO_2 and water vapor on the radiative properties of the atmosphere. An atmosphere with a condensable greenhouse gas has been shown to have a linear scaling of the OLR [105]. This linear scaling is relatively independent of the water content for as long as some water is present, but flattens with increasing temperatures due to the disappearance of the spectral window regions. We modify the EBM to include a parameterization for a RGH limit as follows: At a surface temperature of 46.3°C and a corresponding OLR of 300 W/m^2 (the Komabayashi-Ingersoll Limit, [83]), we hold the OLR fixed as surface temperatures continue to increase, to simulate the atmosphere’s opacity to IR radiation, characteristic of a RGH effect [83]:

$$OLR = \begin{cases} A + BT & T \leq 46.3^{\circ}\text{C} \\ 300\text{ W/m}^2 & T > 46.3^{\circ}\text{C}, \end{cases} \quad (2.1)$$

where $A = 203.3\frac{\text{W}}{\text{m}^2}$ and $B = 2.09\frac{\text{W}}{\text{m}^2\text{ }^{\circ}\text{C}}$. We run model simulations until the annual rate of change in global mean surface temperature falls below $0.004\frac{^{\circ}\text{C}}{\text{yr}}$, at which point the model is designated as converged. However, planets that enter the RGH do not converge, and we end these simulations once the mean global temperature exceeds 100°C . This approach allows each model run to reach equilibrium while maintaining computational efficiency. We simulate aqua planets by assigning a uniform distribution of 99% ocean and the smallest (1%) percentage of land required to prevent singular behavior in the model. For all model simulations we assume a rapid (24-hr) planetary rotation rate, an orbital period of 360 days,

and an incident flux of 1360 W/m^2 at the averaged Earth-Sun distance at zero eccentricity, to isolate the effects of orbital eccentricity and host star SED on planetary climate. Planets orbiting in the habitable zones of lower-mass stars may be captured into 1:1 spin-orbit resonances [41, 96, 87, 46, 190], which will certainly affect climate (see, e.g., 194). However, highly eccentric planets, which are the focus of this study, are more likely to exhibit a higher order spin-orbit resonance than synchronous rotation [40].

2.3.1 Water Loss and Runaway Greenhouse

We calculate the water loss rates for planets with Earth-like atmospheres and G- or M-dwarf host stars, via the energy-limited escape mechanism [188, 126, 75, 16], which allows us to place the strongest constraints on ocean inventory loss rates. We characterize planets in a moist greenhouse as those having atmospheric water mixing ratios between 3×10^{-3} and 1, the upper limit being the point when a RGH ensues [95, 224, 223]. Moist greenhouse planets have stratospheric temperatures high enough to raise the cold trap higher up in the stratosphere or remove it completely. We estimate the water loss rate of a planet due to its host star’s XUV flux as a function of orbital eccentricity.

n	T(K)	mixing ratio
0	< 340	0
1	340 - 350	$3 \cdot 10^{-3}$
2	350 - 370	10^{-1}
3	> 370	1

Table 2.1: The temperature regimes and corresponding average water mixing ratios used in our simulations with an EBM with a runaway greenhouse parameterization.

We use a similar prescription to that of prior work [188, 16], where planetary water loss varies with host star XUV flux at a given orbital distance. We expand this framework to any orbital distance on an eccentric orbit. The following changes are made to estimate the order of magnitude of water loss for moist and RGH planets: First, we identify three temperature

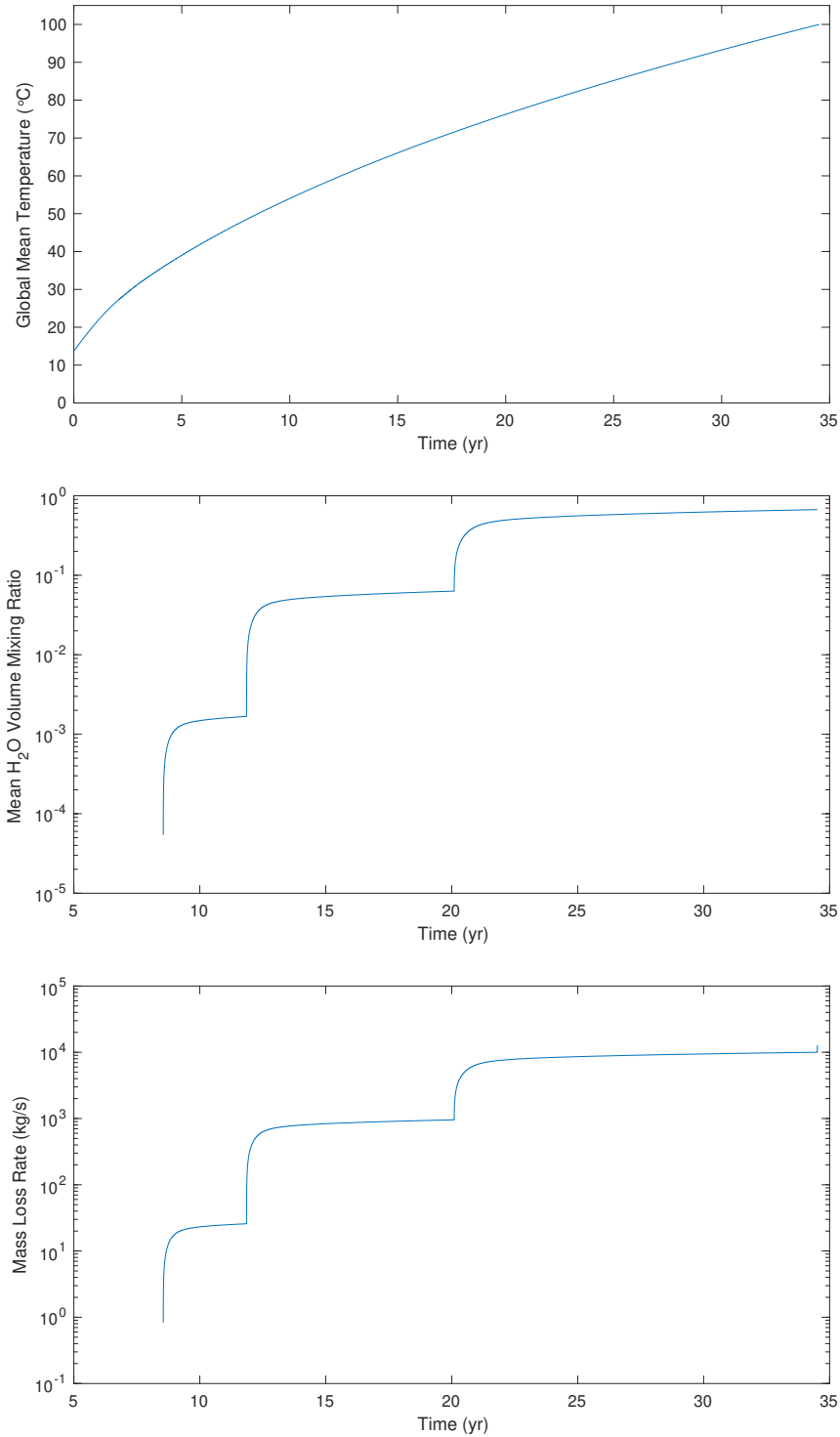


Figure 2.1: The evolution to the equilibrium state of the G-dwarf planet with $e = 0$ receiving receiving $125\% S_0$, where S_0 is the modern solar constant (the instellation on modern day Earth): Mean global temperature (top), mean water mixing ratio (middle) and mass loss rate (bottom) .

regimes which correspond to different water vapor mixing ratios based on the work of Kasting *et al.*(2015) and Wolf *et al.* (2015). For temperatures $T < 340$, the cold trap appears within the stratosphere, preventing any significant mass loss [95]. For the $340 < T < 350$ bracket, we adopt a water mixing ratio of 3×10^{-3} , and in the $350 < T < 370$ bracket a ratio of 10^{-1} . Finally, for $T > 370K$ the water mixing ratios approach unity [95]. Figure 2.1 shows an example evolution of the stratospheric water content and the mass loss rate of a model G-dwarf planet with $e = 0$ and $S = 125\%S_0$. This particular planet enters the RGH after 35 years, and it goes through all four brackets of stratospheric water content, starting from a dry stratosphere up to water mixing ratios approaching unity. The uptick in the mass loss rate at the end of the simulation is the actual mass loss rate in a RGH, but we end the simulations before water mixing ratios approach unity as the final climatic state is known. The first and second brackets correspond to a low and high mixing ratio moist greenhouse. The fourth temperature bracket denotes water loss in planetary regions where the mixing ratios approach unity while the global climate remains stable. This approach allows us to pinpoint those planets in our simulations whose surface conditions were likely indicative of moist greenhouse atmospheres. All temperature regimes and corresponding mixing ratios used in our model are listed in Table 1.

We identify RGH planets as those with surface temperatures exceeding 100° C (such that the water vapor mixing ratio is ~ 1), and no equilibrium state within 250 model years of simulation. The mass loss rate of the atmosphere \dot{m} is calculated by equating the absorbed energy of XUV photons to the gravitational potential at the surface of the planet. Similar to Scalo *et. al* (2007) and Bolmont *et. al* (2017), we link the XUV flux at 1 AU to the mass loss rate of the atmosphere at any distance. However, for each temperature regime of the moist greenhouse, we add a multiplicative factor proportional to the water vapor mixing ratio in the upper atmosphere, and multiply by the corresponding photon absorbing area. Finally, we sum up the mass loss contribution from each region and integrate over the course of the orbit and divide by the orbital period to get the annual mass loss of the atmosphere:

$$\dot{m} = \frac{1}{P} \sum_{n=1}^3 \int_P \frac{\epsilon \kappa(t, \lambda) F_{XUV}[d(t), \lambda] \cdot A_n[t, \lambda] R_p}{GM_p} dt \quad (2.2)$$

where M_p and R_p are the planet's mass and radius, $d(t)$ is the star-planet distance at time t , λ is the latitude, P is the orbital period, ϵ is the XUV absorption efficiency—the fraction of incoming XUV energy transformed into gravitational potential through mass loss, κ is the water mixing ratio factor and A_n is the surface area of each water mixing ratio regime. For all our simulations, $R_p = R_\oplus$, $M_p = M_\oplus$. Planets in a RGH are located within the highest temperature regimes of the sample, with mixing ratios of 1 across the entire planet, reducing the above expression to just one term:

$$\dot{m} = \frac{1}{P} \int_P \frac{\epsilon F_{XUV}[d(t), \lambda] \pi R_p^3}{GM_p} dt \quad (2.3)$$

The ocean loss rate is nine times larger than the hydrogen escape rate, due to the stoichiometry of the photodissociation of water (i.e., for every two hydrogen atoms escaping the atmosphere, a water molecule, which weighs $\sim 9x$ as much, must be photo-dissociated). Following the derivation in Luger and Barnes (2015), the critical flux at which oxygen begins to escape is:

$$F_{crit} = 180 \left(\frac{M_p}{M_\oplus} \right)^2 \left(\frac{R_p}{R_\oplus} \right)^{-3} \left(\frac{\epsilon}{0.3} \right)^{-1} \text{ erg cm}^{-2} \text{ s}^{-1}, \quad (2.4)$$

which corresponds to $F_{crit} = 0.54 \text{ W/m}^2$ for Earth-like planets and an absorption efficiency factor of 0.1. Given a semi-major axis of 1AU, such high XUV flux values are only attained

at periastron passage at eccentricities above $e = 0.767$ and $e = 0.907$ in the M- and G-dwarf planet cases, respectively. As these eccentricities constitute a small fraction of the total parameter space explored, we assume here that only hydrogen escapes the planet’s gravitational well while the oxygen remains behind.

2.3.2 Fractional Habitability

Modeling efforts typically base surface habitability on a planet’s annually-averaged global surface temperature. By this metric, habitability can be “lost” over the course of the orbit of an eccentric planet, particularly during the farthest (apoastron) and closest (periastron) approaches to the host star. As the planet moves farther out towards apoastron, it can completely freeze over. Conversely, at periastron, surface temperatures can reach high enough levels for the planet to enter a moist or RGH state. Between these orbital extremes, an eccentric planet may exhibit temporal habitability, with clement conditions for surface liquid water at times during its year. To quantify the amount of temporal habitability on eccentric planets, we adopt the “fractional habitability” approach of Spiegel *et al.* (2008), where the “habitability function”, $H[d(t), \lambda]$, is equal to one for latitudes with habitable temperatures at a given position in the orbit, and zero otherwise:

$$H[d(t), \lambda] = \begin{cases} 1 & 270 \leq T(\lambda, t) \leq 370 \text{ K} \\ 0 & \text{all other temperatures} \end{cases} \quad (2.5)$$

The fraction of the year for which each latitude is in the habitable temperature range, f_{time} (the latitudinal fractional habitability), is the time-integrated habitability function divided by the orbital period:

$$f_{time}[\lambda] = \int_P \frac{H[d(t), \lambda]}{P} dt \quad (2.6)$$

Finally, the net fractional habitability is the area-weighted integral of the latitudinal fractional habitability over all latitudes:

$$f_{hab} = \int_P \int_{-\pi/2}^{\pi/2} \frac{H[d(t), \lambda] \cos(\lambda)}{2P} d\lambda dt \quad (2.7)$$

We are primarily interested in quantifying the fraction of temporal habitability for planets orbiting stars of different stellar types, and used aqua planets as a test bed for observing general climate trends for varying eccentricity. Broadband planetary albedos (used as inputs to the EBM) increase monotonically with rising stellar effective temperatures [96, 188, 193]. In our EBM, as the surface temperatures fall below $-2^\circ C$, ice forms and the broadband albedo changes correspondingly. We run the EBM with “warm start” (starting from a climate similar to modern-day Earth) and “cold start” (starting from globally ice-covered) conditions and calculate the fractional habitability once the climate reaches equilibrium. The difference in fractional habitability between the two initial conditions is a measure of climate hysteresis—the dependence of the climate state on its history.

2.3.3 Model Inputs

High resolution broadband albedos for planets orbiting F2V star HD128167, K2V star HD22049 [187], G2V star The Sun [26], and M3V star AD Leo² [168, 186] were calcu-

²The Virtual Planetary Laboratory Spectral Database. (<http://vpl.astro.washington.edu/spectra/stellar/mstar.htm>)

lated in previous work, using the Spectral Mapping Atmospheric Radiative Transfer Model, or SMART [137], assuming an Earth-like atmosphere and surfaces composed of ocean, land, and ice of different grain sizes [193]. We employ the broadband albedos of planets with ocean-covered surfaces for our aqua planets, with frozen regions corresponding to a 50% mixture of snow and blue marine ice weighted by the corresponding SED, which is normalized to 100% of the modern solar constant (1360 W/m^2). For more details on this approach, see Shields *et al.* (2013).

We run our models with an obliquity $\theta = 0^\circ, 45^\circ, 90^\circ$ and the Earth’s longitude of periastron, or azimuthal obliquity, $\omega = 102.065^\circ$. This angle only affects the climate of planets with non-zero obliquity and is defined from the vernal equinox, thus already accounting for the precession angle. The XUV flux for the Sun is taken from Airapetian *et al.* (2017), who constructed it with both the Solar Dynamic Observatory and the Flare Irradiance Spectral Model (FISM). The AD Leo XUV flux taken from Chadney *et al.* (2015) was constructed using a coronal model. Additionally, in our mass loss calculations we do not include stellar evolution (i.e., we keep the stellar luminosity constant). All stellar parameter inputs are summarized in Table 2.2.

Star	Broadband Albedos			$F_{XUV}(a = 1AU)$
	Land Albedo	Ocean Albedo	Ice Albedo	mW/m^2
AD Leo (M3V)	0.332	0.234	0.315	29.4
HD 22049 (K2V)	0.401	0.302	0.401	—
The Sun (G2V)	0.415	0.319	0.514	5.60
HD 128167 (F2V)	0.414	0.329	0.537	—

Table 2.2: Stellar and planetary parameters used as input to the EBM, including broadband planetary albedos from Shields *et al.* (2013) and incident XUV fluxes from Airapaitian *et al.* (2017) and Chadney *et al.* (2015).

The XUV fluxes for both the M- and G-dwarf stars at an average Earth-Sun distance of 1 AU are scaled to the varying orbital distance of the eccentric planet over the course of its year, and used as input to our EBM. We assume here that the XUV flux scales linearly with the bolometric luminosity. An absorption efficiency factor of $\epsilon = 0.1$ is applied in

our calculations. For this choice of XUV fluxes, our planets are well within the energy-limited regime for all eccentricities below 0.97 and 0.95 for the M- and G-dwarf planets, respectively. Above these eccentricities the XUV flux at the periastron passage is large enough ($> 10^4 \frac{\text{erg}}{\text{cm}^2 \text{s}}$) so that radiative recombination significantly inhibits the rate of mass loss [144].

2.3.4 Model Validation

The EBM with broadband albedos as input from SMART was previously validated and shown to reproduce the Earth’s current ice line latitude and global mean surface temperature to within 6° and 3°C , respectively [193]. Here we have validated the EBM with our RGH parameterization by reproducing the moist and RGH instellation thresholds of Wolf and Toon (2015). As shown in Figure 2.2, the climate of our simulated G-dwarf planet with zero eccentricity remains stable up to $119\% S_0$ —where S_0 is the modern solar constant for the Earth—compared to $121\% S_0$ found by [224]. The onset of the moist greenhouse and significant water loss occurs here at $116\% S_0$, compared to $119\% S_0$ in their study. Figure 2.2 shows the global mean temperature and the mean OLR as calculated with our EBM with the RGH parameterization, compared with the 3D CAM4 GCM (global climate model), and with the EBM with the traditional linear OLR parameterization. Our OLR parameterization produces a much better agreement in surface temperature with the GCM than the EBM with the default OLR parameterization, while not greatly changing the average OLR behavior as instellation increases. The CAM4 simulations exhibit a sharp increase in surface temperature and the mean OLR as the planet transitions into the moist greenhouse, once the solar constant is increased by 12.5%. However, as the solar constant increases, the climate is stabilized by the increasing top-of-atmosphere albedo, due to the formation of thick cloud decks [224]. The EBM does not include moist physics, and our RGH parameterization leads to a thermal runaway that is exponential with increasing instellation.

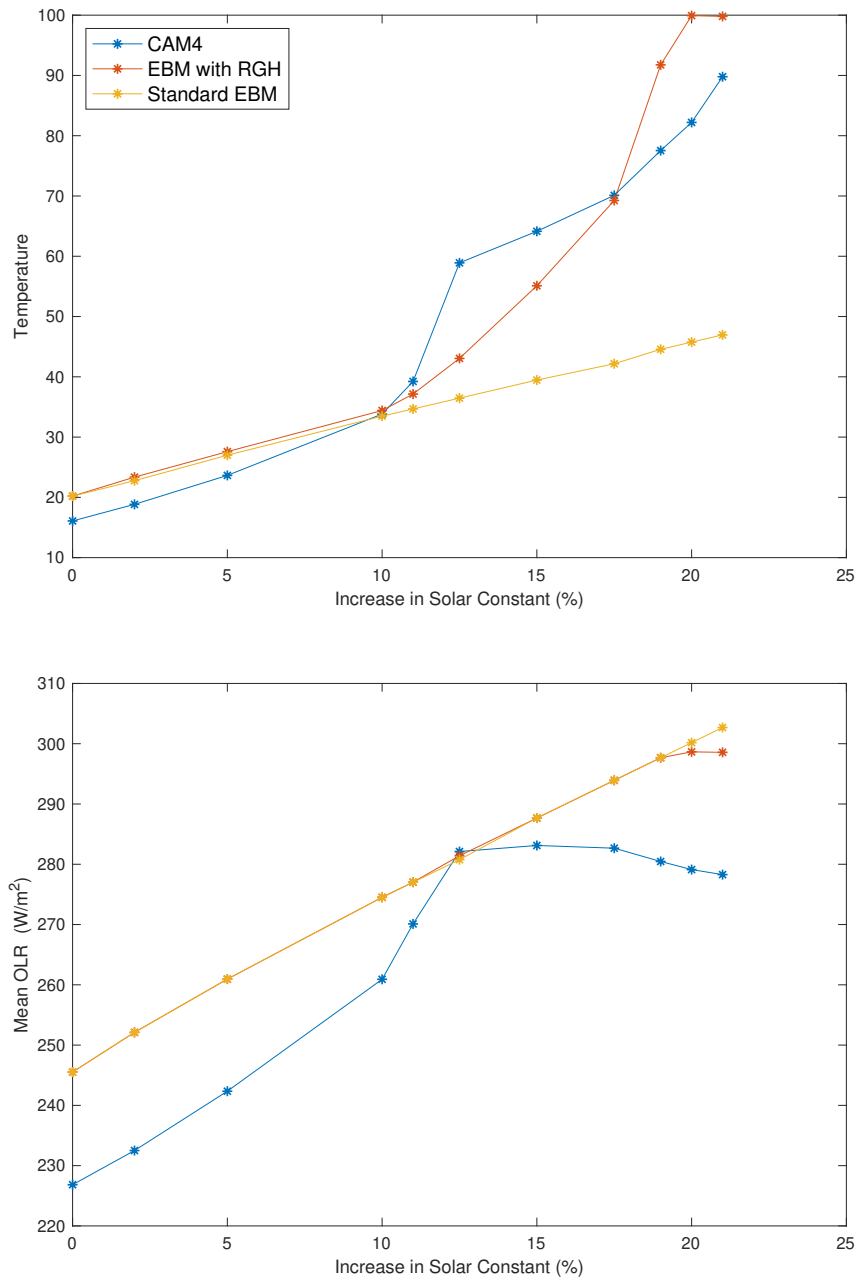


Figure 2.2: Top: Global mean surface temperature vs. increase in instellation in percent of the modern solar constant for a G-dwarf planet, using the standard EBM, the EBM modified to include a RGH parameterization, and the CAM4 GCM. Bottom: Comparison of the mean OLR between the three models. The CAM4 data is from Wolf and Toon *et al.* (2015)

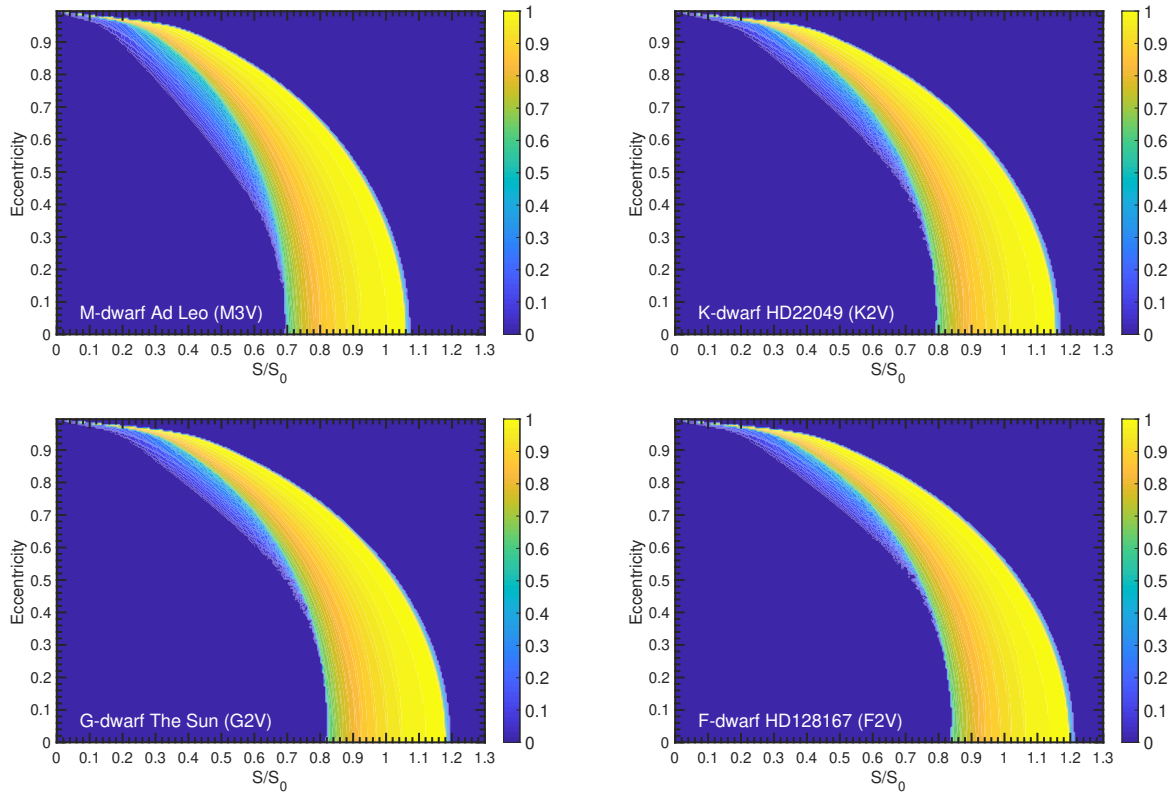


Figure 2.3: The instellation range over which planets exhibit habitable surface conditions throughout their entire orbit (bright yellow region) shrinks with increasing eccentricities, but the emergence of a temporarily habitable zone (light blue region) helps to compensate for this reduction.

2.4 Results

2.4.1 Fractional Habitability

Figure 2.3 shows the warm start results in the eccentricity-instellation parameter space for all 2.3 stellar types. In our EBM, the cold edge of habitability is ultimately determined by the large ice-cap instability, which causes rapid collapse of the ice caps to the equator once the instellation falls below a certain threshold. On the warm end, habitability is truncated by the thermal runaway of the atmosphere. We find that in the case of a G-dwarf planet with an eccentricity $e = 0$, and an Earth-like atmosphere, the inner edge of EHZ corresponds to a stellar flux of 119% S_0 , while the outer edge corresponds to 82.5% S_0 , although with a significant ice cap. In the case of the M-, K-, and F-dwarf spectral types the outer and inner edges of the EHZ are [70% S_0 , 107.5% S_0], [80% S_0 , 117% S_0], [84.5% S_0 , 121.5% S_0], respectively. With increasing eccentricity, planets with habitable conditions shift toward lower instellation values. On the K-, G-, and F-dwarf planets, the warming effects of eccentricity have a stronger impact on the inner rather than outer edge of the EHZ, due to the extra energy required to thaw sea ice on an ice-covered planet, compared with the transition from a water world to a moist hot house. On planets orbiting just outside of their host stars' full-orbit EHZ—the eccentricity-instellation parameter space over which any portion of the planet's surface is habitable throughout its entire year—a minimum eccentricity of about 0.2 is required to actually thaw sea ice. On the inner edge, we see a much steeper outward migration with increasing eccentricity.

In our set of modeled planets, we observe temporal habitability around any star with sufficient orbital eccentricity. A sharp transition is seen in Figure 2.3, from planets with fractional habitability close to unity and exhibiting full-orbit habitability (yellow region), to planets with fractional habitability below 0.5 (light blue region). This light blue region consists of planets which experience globally frozen conditions for a fraction of the year and

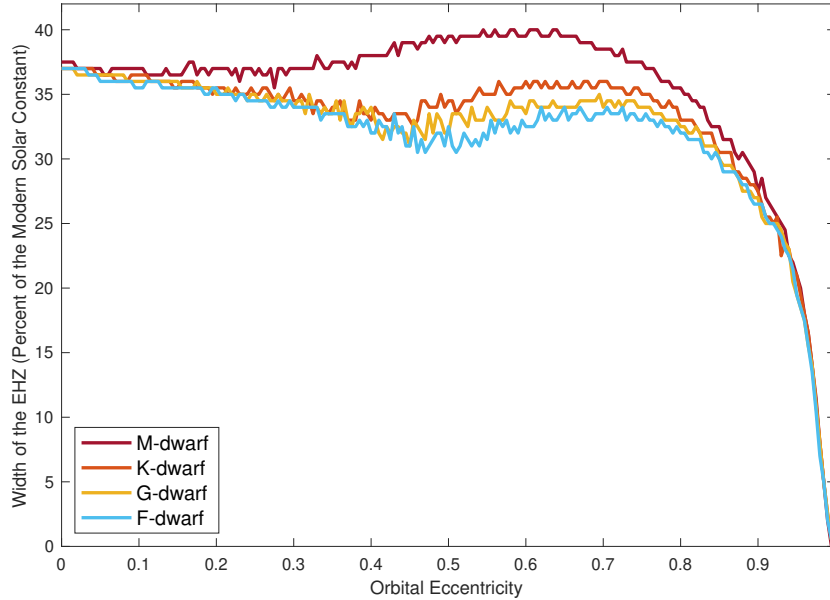


Figure 2.4: The range of instellations for which warm start planets orbiting M-,K-,G- and F-dwarf stars exhibit (non-zero) fractional habitability, as a function of orbital eccentricity.

habitable conditions during the rest of the orbit. Cooler stars exhibit temporal habitability over a larger eccentricity-instellation parameter space. The region of temporal habitability on M-dwarf planets is 27%, 34% and 39% larger than their K-, G-, and F-dwarf analogs, respectively. Moreover, the minimum eccentricity and instellation required for the appearance of temporal habitability is smaller for planets orbiting cooler stars. For our M-dwarf planets, we observe temporal habitability at an eccentricity as low as $e = 0.13$. The minimum eccentricity required for the appearance of temporal habitability around the K-, G-, and F-dwarf planets is 0.230, 0.270, and 0.285, respectively. For larger eccentricities, temporal habitability appears over a larger range of instellations for any host star. At the same time, the instellation range of the full-orbit EHZ shrinks with increasing eccentricities. At eccentricities above $e = 0.6$, the region of temporal habitability becomes a significant component of the total EHZ and constitutes $\sim 50\%$ of the total at $e = 0.8$.

The difference in the response of the inner and outer edges is responsible for the gradual decline and shift of the EHZ to lower instellations up to $e = 0.5$, where the appearance of

temporal habitability expands the outer habitable edge (Figure 2.4). Due to the appearance of temporal habitability at eccentricities as low as ~ 0.13 , the M-dwarf planet has no decline in the EHZ until all planets enter the RGH at extreme eccentricities.

2.4.2 Mass Loss and Runaway Greenhouse Planets

We calculate the annual mass loss rates for the Sun and for the mid-type M-dwarf star, AD Leo. Figure 2.5 shows the time (in Myr) it takes to lose Earth’s entire surface water inventory as a function of eccentricity and instellation. For planets in a RGH with the same eccentricity and instellation, the mass loss rate is directly proportional to the XUV flux (see equation 3). Due to the fact that AD Leo produces $\sim 6x$ larger XUV flux than the Sun, the water loss is $\sim 6x$ larger. We find that the eccentricity threshold for thermal runaway is lower on the M-dwarf planet by $12\% S_0$ at $e = 0$ and $5.5\% S_0$ at $e = 0.9$ relative to the G-dwarf planet.

On a circular orbit, a G- and an M-dwarf planet in a RGH receiving $120\% S_0$ can become desiccated in ~ 3.6 Gyr and ~ 690 Myr, respectively. We find that at any eccentricity the mass loss becomes significant at a few percent of S_0 below the thermal runaway threshold. For the G-dwarf planet at $e = 0$ and instellations between 118.5% and $119.5\% S_0$, prior to the thermal runaway the planetary conditions are conducive to the loss of Earth’s surface water inventory in $7.3 - 5.2$ Gyr. Similarly, the M-dwarf planet receiving $106.5\% - 107.5\% S_0$ (thermal runaway occurs with a flux of $108\% S_0$) has desiccation timescales of $1.32 - 1.03$ Gyr. This region of significant water loss while in the moist greenhouse exhibits itself as the small strip immediately to the left of the black contour indicating the transition from the moist to RGH region. Across the $0 - 0.9$ eccentricity range, the annual water loss rate in a RGH state varies by a factor of ~ 2 at most, regardless of the host star SED.

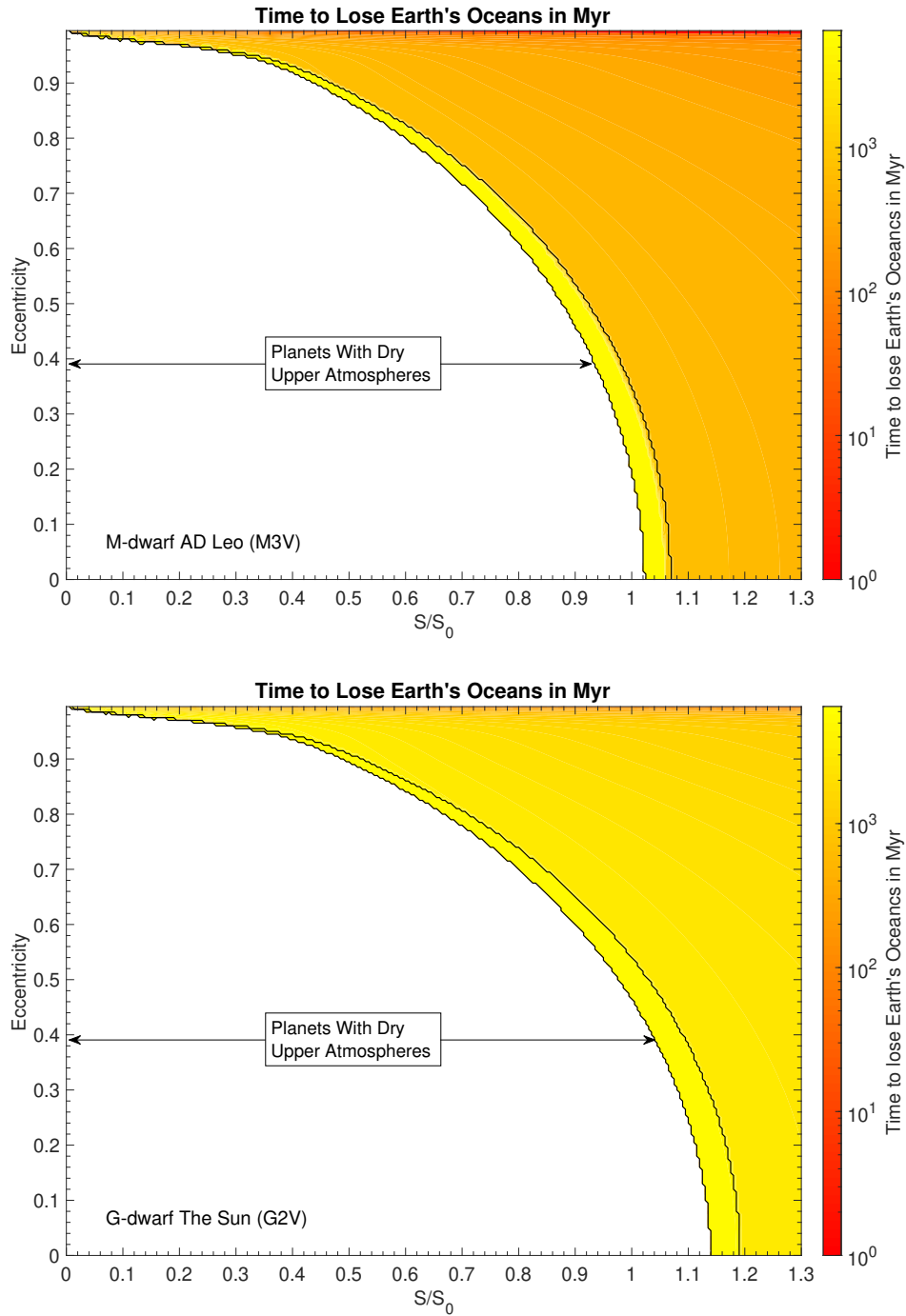


Figure 2.5: Time to lose Earth's entire surface water inventory on aqua-planets orbiting M-dwarf AD Leo and G-dwarf star The Sun in Myr. The M-dwarf planet is exposed to $\sim 6x$ more XUV flux than the G-dwarf planet with an equivalent climate, leading to a $\sim 6x$ higher mass loss rate. The black contour outlines the boundaries of the moist greenhouse.

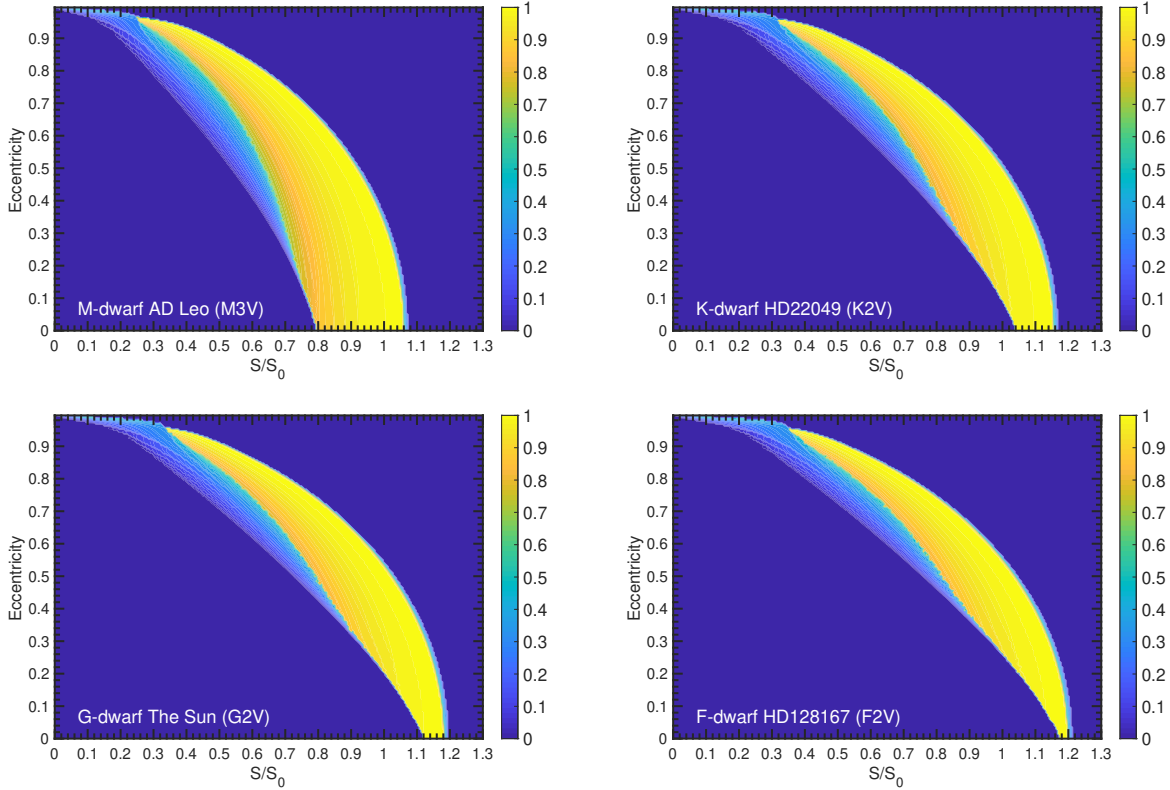


Figure 2.6: Fractional Habitability on the M-,K-,G- and F-dwarf planet with varying eccentricity and instellation, after EBM simulations assuming cold start conditions.

2.4.3 Bistability

Figure 2.6 shows the fractional habitability on M-, K-, G-, and F-dwarf planets at varying eccentricity assuming cold start initialization. A comparison with the warm start results shown in Figure 4 reveals two different outcomes, depending on starting conditions—a situation we refer to here as “bistability”. On circular orbits, planets orbiting all stellar types exhibit bistability in some instellation range. The cooler the host star, the smaller this range of bistability. As shown in Figure 2.7, climate hysteresis (approximated by the warm minus cold start difference in fractional habitability) decreases with increasing eccentricity for any stellar type. In the case of the M-dwarf spectrum, planets with eccentricities above 0.26 exhibit no bistability. Similarly, in the K-,G-, and F-dwarf cases, no bistability (seen as the yellow wave-shaped region) occurs at eccentricities above 0.45, 0.48, and 0.5, respectively.

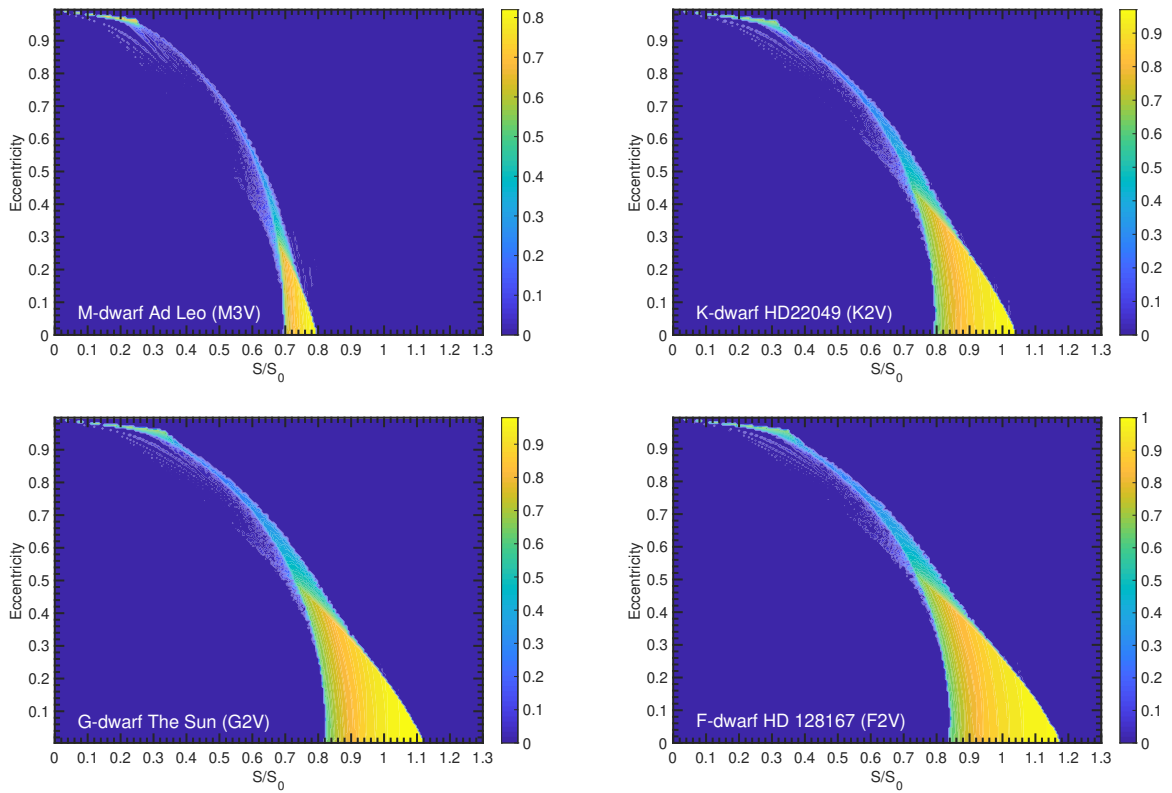


Figure 2.7: Warm - cold start difference in the fractional habitability on the M-,K-,G- and F-dwarf planet with varying eccentricity and instellation.

The outer edge of the full-orbit EHZ is affected by the initial conditions at any eccentricity. In both warm and cold start cases, planets only exhibit differences in habitability in the bistability region at low eccentricities or along the interface between the temporal and full-orbit habitable regions (seen as the long blue arc), indicating an expansion of the region of temporal habitability on cold start planets compared to those simulated with warm start conditions.

2.4.4 Habitability at Higher Obliquities

To test the sensitivity of our results to changes in obliquity, we repeated our zero-obliquity calculations of fractional habitability on warm start M-dwarf planets for larger obliquities (45° and 90°), as shown in Figure 2.8. Obliquity has a small effect on the inner edge of the EHZ, due to the absence of sea ice on these planets. Over the entire range of eccentricities, for an M-dwarf planet with an obliquity of 90° , the inner edge of the EHZ occurs at a flux that is at most 2.5% larger than its 0° obliquity counterpart. However, the outer edge of the habitable zone is more sensitive to changes in obliquity, due to the presence of ice caps (or ice belts) on these planets. The outer edge of the EHZ appears at a flux that is at most 7% higher on planets with 90° compared to 0° obliquity. Planets with 90° obliquity also exhibit a region of small fractional habitability (< 0.1), corresponding to habitable conditions at the poles, constituting both full-orbit ($e \approx 0$) and temporarily habitable EHZ regions ($e \gg 0$). For planets with zero eccentricity, this region spans an instellation range of $68 - 76\% S_0$. With increasing eccentricity it extends outside of the full-orbit EHZ to include planets with eccentricities as large as 0.9. With this region of small fractional habitability included, planets with 90° obliquity have an EHZ that is 46% larger than their 0° obliquity counterparts.

We find that larger obliquity leads to warmer climates on planets in the full-orbit EHZ. With

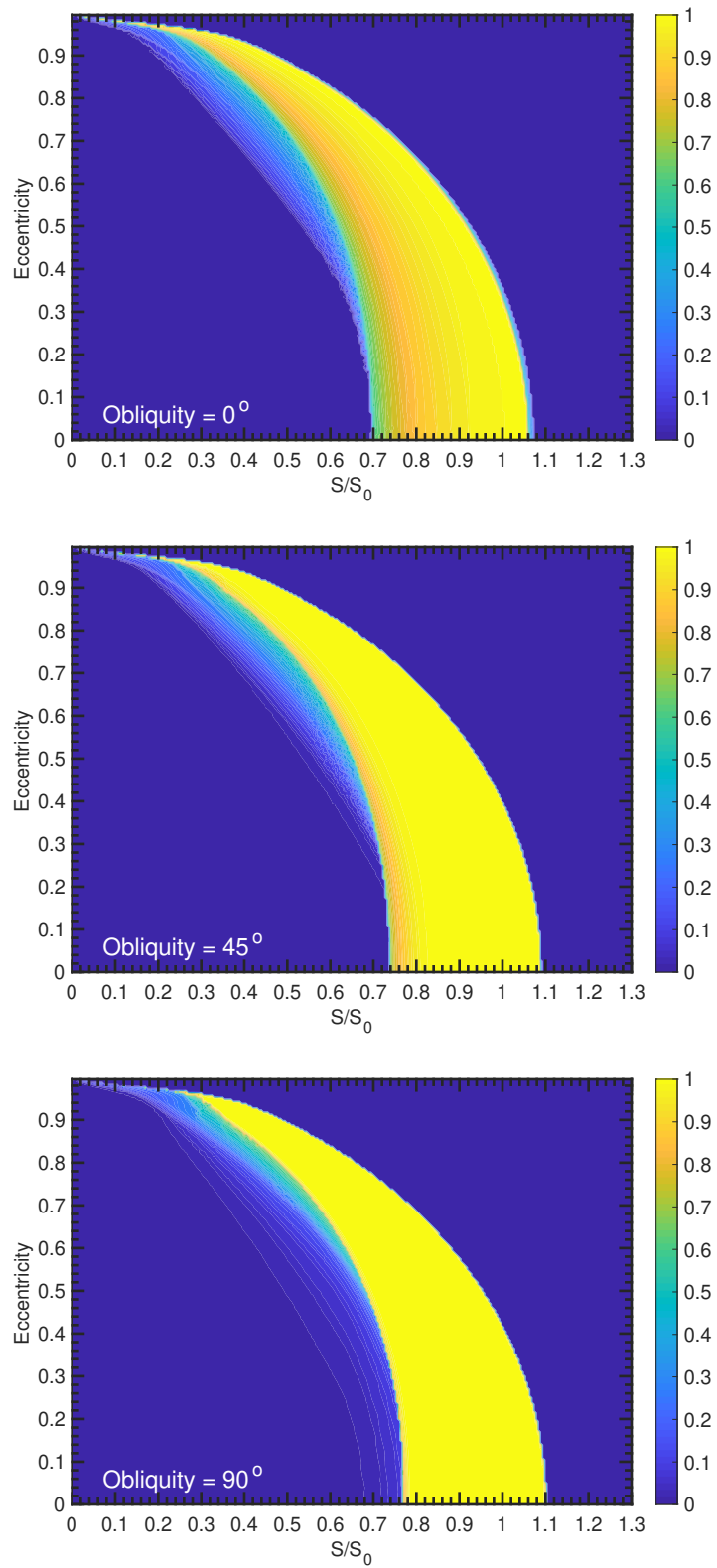


Figure 2.8: Fractional Habitability on an M-dwarf planet with 0° , 45° , 90° obliquity, after EBM simulations assuming warm start conditions.

increasing obliquity the ice caps/belts retreat and fractional habitability approaches unity. For planets with a 90° obliquity, we see no sea ice, and fractional habitability is equal to 1 within the full-orbit EHZ.

2.5 Discussion

In this work we used an EBM with a simple RGH parameterization to explore the effects of eccentricity, obliquity and host star SED on habitability and water loss of terrestrial aqua planets with Earth-like atmospheres orbiting F-, G-, K-, and M-dwarf stars. The instellation range over which planets exhibit habitable surface conditions throughout their entire orbit shrinks with increasing eccentricities, but the emergence of a temporarily habitable zone helps to compensate for this reduction of the full-orbit EHZ. The temporarily habitable zone widens with decreasing host star effective temperature. Uniquely for M-dwarf planets, the total EHZ (temporal + full-orbit) widens with increasing eccentricity up to $e \approx 0.6$. For planets in a RGH, Earth's entire surface water inventory can be lost in a few Gyr. Similar water loss is achieved in a moist greenhouse state once water mixing ratios approach unity in the tropical regions of the planet. Earth-like aqua planets on eccentric orbits remain habitable during some portion of their orbits for a wide range of instellations, and reduced or eliminated bistability increases the likelihood that an observed eccentric planet is in a state determined purely by its current orbital configuration.

Given the sensitivity of the inner habitable-zone edge to increases in eccentricity, if an Earth-like aqua planet on a circular orbit were perturbed to a higher eccentricity it could potentially enter the RGH state, desiccating the surface. In the case of the G-dwarf planet receiving $100\% S_0$ this occurs in Figure 2.5 at eccentricities above $e = 0.55$. For the M-dwarf planet receiving $100\% S_0$, the minimum eccentricity required for the thermal runaway of the planet is $e = 0.38$.

For any eccentricity, the EHZ shifts towards lower instellations for cooler stars, due to the lower albedos of surface ice and snow on orbiting planets, and the absorptive properties of atmospheric gases. At longer wavelengths ice and snow absorb more strongly [45], leading to smaller broadband planetary albedos [193, 191], more efficient thawing of sea ice, and a wider region of temporal habitability on planets orbiting cooler stars. Additionally, greenhouse gases like water vapor and CO₂ absorb more strongly in the IR, which leads to a thermal runaway of the climate at lower values of instellation. Sea ice thaws more efficiently on planets orbiting cooler stars. While this holds true for planets at any eccentricity, the differences in the fractional habitability due to different spectral energy distributions diminish with increasing eccentricities—at high eccentricities different stars have similar fractional habitability as a function of instellation.

We find that increasing obliquity shrinks the EHZ for planets at any eccentricity. Increasing obliquity leads to an inward migration of the outer edge of the EHZ, due to ice-albedo feedback and ice-sheet instability. These mechanisms do not affect planets near the inner edge of the habitable zone due to the total absence of sea ice. This effect is strongest at $e = 0$. With increasing eccentricity, the increasing seasonal variations in radiative forcing dominate the effects of obliquity as with the effects of stellar spectral energy distribution. We find that larger obliquity warms the climates of planets within the full-orbit EHZ. However, at higher obliquities the sea ice becomes increasingly unstable, leading to larger climate hysteresis.

For our choice of orbital period (360 days), we find no planets exhibiting periodic phases of RGH conditions at any eccentricity. This fact should hold true for any planet with smaller orbital periods. However, with larger periods, for a sufficiently large eccentric orbit, planets may be able to spend enough time at or near apoastron to cool sufficiently for evaporated oceans to condense back onto the surface. Additionally, the moist greenhouse region in this parameter space is quite small in both the M- and G-dwarf cases, but the large water loss rates achieved for moist greenhouse planets may challenge the habitability of these planets.

In our mass loss calculations we assume a constant, quiescent XUV flux. While this may be sufficient for older and more dormant main-sequence stars, the flare activity on a mid-type M-dwarf such as AD Leo may alter the physics of atmospheric escape. Additionally, for XUV fluxes exceeding $\sim 0.4 \text{ W/m}^2$ the absorption efficiency decreases rapidly[16]. In the case of AD Leo, this flux is achieved at periastron passage at an eccentricity of 0.73. In the case of the Sun, such flux values are only achieved at eccentricities above 0.89. Our water loss timescales may therefore be overestimated on planets with the largest eccentricities for an assumed constant absorption efficiency factor of 0.1.

We find a large drop in fractional habitability along the transition from full-orbit to temporarily habitable planets. This sharp transition is likely due to a combination of effects. The ice-albedo feedback and the ice-cap instability accelerate the expansion of the ice caps as planets move towards apoastron. Planets that freeze over remain frozen for a significant amount of time, significantly reducing their fractional habitability. This causes a sharp transition between completely thawed planets and those that are temporarily frozen.

Our choice of constant water mixing ratios in the three temperature brackets may lead to over or underestimation of water loss of order unity on moist greenhouse planets, depending on the instellation. However, owing to the fact that water mixing ratios rise rapidly above 340K, this approximation is appropriate for determining the mass loss limited inner boundary of the EHZ to within one percent of the solar constant.

The EHZ assumes an Earth-like atmosphere, with fixed CO_2 . Planets on eccentric orbits may experience changes in atmospheric CO_2 concentration as surface temperatures vary throughout the orbit if a CO_2 cycle operates on these planets, as it does on the Earth [215] and Mars [77]. Including a dynamic, orbital distance-driven CO_2 cycle into a climate model would be useful towards further refining the boundaries of the EHZ.

We assume constant broadband planetary albedos throughout our simulations, given an

Earth-like atmosphere. The reflective properties of a planet’s atmosphere will likely change with temperature, water vapor mixing ratio, and CO₂ concentration, affecting the planet’s overall (atmosphere + surface) broadband albedo. Incorporating into a climate model a temperature-dependent broadband planetary albedo parameterization that accounts for variations in the atmospheric concentration throughout the temperate, moist, and RGH regimes would be an important step to take in future work.

2.6 Conclusions

Using a 1-D EBM with a simple runaway greenhouse parameterization, we have demonstrated that eccentric planets orbiting cooler stars exhibit temporal habitability in a larger region of the eccentricity-instellation parameter space compared with planets orbiting hotter, more luminous stars. This difference is largely due to lower relative ice and snow surface albedos, leading to more efficient thawing of sea ice on planets orbiting cooler, redder stars. Our approach reveals a refined eccentric habitable zone (EHZ) that is sensitive to host star SED and planetary obliquity. Additionally, our runaway greenhouse parameterization allowed us to calculate the inner boundary of the eccentric habitable zone (EHZ) with much greater accuracy than the traditional linear OLR parameterization. Orbital eccentricity leads to a rapid outward migration of the inner edge of the EHZ and a slower outward migration of the outer edge, leading to an overall reduction of the EHZ for all our simulated planets except M-dwarf planets. However, this reduction is somewhat alleviated at eccentricities above ~ 0.5 by the appearance of a sizable temporal habitable zone. Conversely, the EHZ on eccentric planets orbiting M-dwarf stars widens with increasing eccentricity until all planets enter a runaway greenhouse state at extreme eccentricities. While in a runaway greenhouse, the M-dwarf planet experiences $6\times$ greater water loss compared to its G-dwarf counterpart. Across the $e = 0 - 0.9$ eccentricity range the water loss rates in a runaway greenhouse state vary

by a factor of 2. We also find that increasing planetary obliquity shrinks the EHZ, due to the inward migration of the outer edge of the EHZ, at the same time warming the climate of the planets in the full-orbit EHZ. Our study of bistability, through a fractional habitability comparison, reveals that the climates of planets with non-zero orbital eccentricities may be less sensitive to their histories. Bistability disappears all together with eccentricities larger than 0.26 on M-dwarf planets, an eccentricity much smaller than the 0.46 - 0.5 values required for no bistability on planets orbiting hotter K-, G-, and F-dwarf stars.

Chapter 3

No Terminator Habitability on Earth-like M-dwarf Aquaplanets With 1-bar Surface Pressures

3.1 Abstract

The large day-night temperature contrasts possible on synchronously-rotating planets introduce the possibility of the day side reaching temperatures hot enough to generate a runaway greenhouse state, while on the night side surface temperatures remain below the freezing point of liquid water. In this scenario, the only place where surface habitability may be possible lies along the planet’s terminator—the narrow strip of latitudes dividing the day and night sides of the planet. We refer to such planets as possessing, “terminator habitability”. Here we employ a three-dimensional global climate model to explore this possibility on Earth-like aquaplanets—planets with a large water inventory and an absence of continents—orbiting mid- and late-type M-dwarf stars. We find that terminator habitability is

implausible with atmospheric surface pressures of 1 bar, due to the strong day-night heat and water transport characteristic of highly irradiated and synchronously-rotating aquaplanets. We find these results to be largely insensitive to the spectrum of the M-dwarf host star.

3.2 Introduction

Habitable-zone M-dwarf planets orbit much closer in to their stars than their counterparts orbiting F-, G-, or K-dwarf stars, increasing the likelihood of a 1:1 spin-orbit resonant, “synchronous” rotation state [41], where planets have permanent day (substellar) and night (antistellar) sides. In such a state, a planet’s night side could reach temperatures low enough for all atmospheric content to condense out onto the surface [87, 139, 120]. On the highly irradiated day side, a runaway greenhouse could ensue, in which saturation with water vapor causes the atmosphere to become opaque to outgoing infrared (IR) radiation, preventing the planet from cooling, and causing surface temperatures to “runaway” uncontrollably [83, 96, 108]. This stark contrast between day and night side climatic states introduces the possibility that surface habitability could exist solely in the terminator region of the planet—the boundary that divides the day and night sides; a situation we refer to as “terminator habitability”.

The habitability of synchronously-rotating M-dwarf planets has been the subject of extensive research and debate over the last two decades (see, e.g., 96, 72, 87, 1, 86, 202, 180, 184, 108, 233, 190, 226, 109). Understanding and quantifying the degree to which surface habitability is possible on these planets is of demonstrable importance as habitable-zone planets continue to be found orbiting M-dwarf stars (see, e.g., 6, 170, 66, 39).

Previous modeling studies have shown that given a thick enough atmospheric concentration ($>\sim 100$ mbar) of a greenhouse gas such as CO_2 , the atmosphere of a synchronously-rotating planet could transport enough heat from the day side to the night side to prevent atmospheric

collapse on the night side of these planets [87, 227]. Additionally, atmospheric heat transport is more efficient on aquaplanets—planets with a large water inventory and an absence of continents—rather than dry planets due to the additional greenhouse warming and stronger atmospheric water vapor heat transport [86, 46]. These results largely assume terrestrial values of instellation, and have not explored the effect on day-night temperature contrasts of increasing instellation towards the inner edge of the habitable zone. The effect of the spectral energy distributions (SEDs) of M dwarfs, which emit large amounts of radiation at near-IR wavelengths, where CO₂ and H₂O absorb strongly, have also not been taken into account in these studies. The M-dwarf SED has been shown to produce higher temperatures at a given instellation on orbiting planets compared to planets orbiting more luminous stars at equivalent stellar flux distances [193, 191, 192].

Here, we employ a three-dimensional (3D) global climate model (GCM) to explore the possibility of terminator habitability as a stable climate state on aquaplanets with Earth-like atmospheric concentrations of CO₂ and surface pressure, receiving varying amounts of instellation from mid- and late-type M-dwarf stars. In section 2, we describe our model configuration and simulations. In section 3, we describe the results of our simulations over a range of stellar fluxes for planets orbiting both mid- and late-type M-dwarf host stars. We discuss the climatic implications of synchronously rotating planets on day-night contrasts and terminator habitability in section 4.

3.3 Methods

We used version 4 of the Community Earth System Model (CESM), a fully-coupled 3D global circulation model (GCM), in concert with the ExoCAM package¹ which is based on the atmospheric component to CESM4 (the Community Atmosphere Model version 4, or

¹<https://github.com/storyofthewolf/ExoCAM>

CAM4). ExoCAM includes a flexible correlated- k radiative transfer package² for generalized exoplanet applications.

We simulated the climates of synchronously-rotating aqua planets (no land) orbiting mid-type M3V Ad Leonis and late-type M8V TRAPPIST-1 host stars. Simulations were run with a 50m, fully mixed ocean with zero heat transport (OHT) as has been done in previous exoplanet habitability studies [193, 233, 191, 110, 109]. Yang *et al.* (2019), have shown that OHT becomes increasingly weaker near the inner boundary of the Habitable Zone for synchronously rotating planets and atmospheric heat transport dominates. We set the zonal and meridional atmospheric grid resolution to 1.9° and 2.55° , respectively, with 26 vertical levels. We used composite spectra derived from observations for AD Leonis [186] and TRAPPIST-1 spectrum [122].

The ice model component of CESM, CICE4 [81], was set to thermodynamic ice only. We employed the more easily manipulated 2-band sea-ice albedo parameterization of CESM3, which divides the spectrum into the the visible ($\lambda \leq 0.7\mu m$) and near-IR ($\lambda > 0.7 \mu m$) bands. Two-band albedos were weighted by the spectrum of each host star. For the M3.5V host star, Ad Leonis, the bare ice albedos were 0.18 and 0.69 in the visible and near-IR, respectively. Dry snow albedos were 0.49 in the near-IR and 0.97 in the visible. For the M8V host star, TRAPPIST-1, the bare ice albedos were set to 0.13 (visible) and 0.68 (near-IR), 0.98 (visible) and 0.43 (near-IR) for dry snow.

We have assumed a present Earth atmosphere level of CO_2 , N_2 , H_2O and O_2 . Ozone levels were set to zero, as done in earlier work [193, 191]. The planetary radius and surface gravity are set to Earth’s values. We did not adjust the default orbital period in CESM4 (360 days), and set the rotation period equal to this period to simulate synchronous rotation. While habitable-zone M-dwarf planets would have smaller orbital periods, this assumption allowed us to isolate the effects of instellation and M-dwarf host star SED on the possibility

²<https://github.com/storyofthewolf/ExoRT>

of terminator habitability on orbiting planets.

Our simulations span an instellation range of $1360 W/m^2 - 2300 W/m^2$ —the inner arm of the habitable zone of M-dwarf stars. We present a comparison of how the climates and the day-night temperature contrasts of our simulated planets respond to high instellations near the inner boundary of the HZ in the following sections.

3.4 Results

Figure 3.1 shows the substellar, antistellar, and terminator mean surface temperatures for planets orbiting a mid- (AD Leo) and late- (TRAPPIST-1) type M dwarf star. Average substellar surface temperatures exhibit a weaker climatic response with increasing stellar flux compared to the antistellar and terminator regions of the planets. For example, the substellar temperatures of the planets orbiting AD Leo (TRAPPIST-1) increase by only 11.9K (13.1K) for a stellar flux increase of $690 W/m^2$, from $1360 W/m^2$ to $2050 W/m^2$. Comparatively, over the same change in stellar flux the antistellar temperatures increase by 35.7K (37.5K). At instellations above $2050 W/m^2$, where we observe the complete deglaciation of the night side for planets orbiting both stellar types, the antistellar temperatures have an even stronger comparative response to changes in instellation. Between $2050 W/m^2$ and $2300 W/m^2$, substellar temperatures increase by 16.4K (14.4K), compared with 44.4K (46.5K) for the antistellar and 31.7K (33K) for the terminator regions of the planets.

Outgoing longwave radiation (OLR) at the top of the atmosphere (TOA) in cloudy and clearsky conditions, and average cloud forcing, are shown in Figure 3.2 for the day and night sides of our simulated planets receiving variable amounts of incident stellar flux. Similar day/night OLR behavior is seen for simulated planets orbiting both host-star spectral types. For low stellar fluxes ($< 1600 W/m^2$) planets cool predominantly through the day side (Fig.

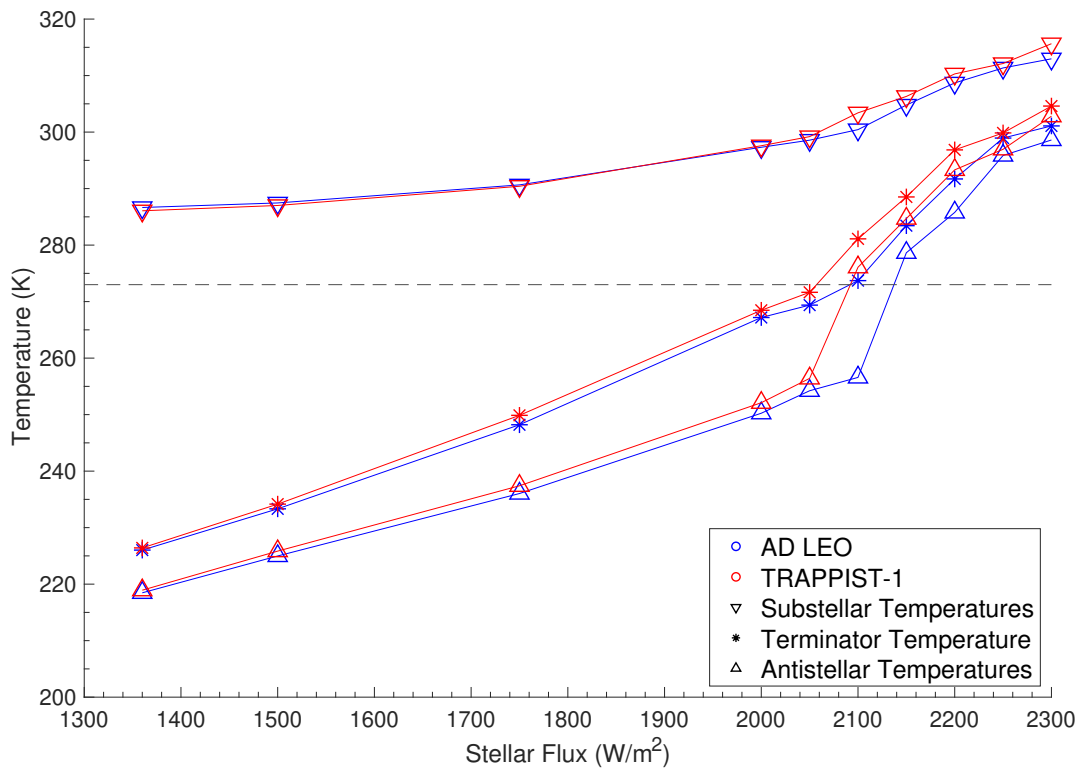


Figure 3.1: Mean surface temperatures as a function of stellar flux for the substellar, antistellar, and terminator regions of an Earth-sized planet orbiting M3V star AD Leo (blue) and M8V star TRAPPIST-1 (red). The freezing point of liquid water is marked with a horizontal dashed line for reference.

3.2a). At these fluxes the night side of the planet receives little heat, yielding correspondingly low amounts of OLR, producing the low surface temperatures seen in Figure 3.1. As the incident stellar flux is increased, the response in the OLR increases on the night side, dominating the cooling of these planets for stellar fluxes larger than $1600 W/m^2$. The day/night OLR contrast becomes increasingly larger at higher stellar fluxes. The largest contrast of $\sim 55 - 60 W/m^2$ is found on deglaciated planets receiving fluxes $> 2050 W/m^2$. However, in the absence of clouds, the day-side OLR dominates the total longwave emission at stellar fluxes up to $2050 W/m^2$ (Fig. 2b). The day-side cloud forcing is much stronger at all stellar fluxes considered in this work, as shown in Figure 3.2c. The cloud radiative forcing on the planets' day sides continues to increase up to the near the deglaciation thresholds for these planets's night sides, and then decreases as the night sides of both planets deglacier and the cloud deck shifts towards higher altitudes (Figure 3.2c).

Figure 3.3a shows the average night-side specific humidity over the range of simulated instellations. The specific humidity rises slowly below the deglaciation threshold due to atmospheric water transport from the day-side of the planet. Planets above the deglaciation threshold exhibit a much sharper rise in humidity as sea ice melts and the tropospheric cold trap is removed. Figure 3.3b shows the day-side cloud cover divided into the low, medium and high cloud levels. The steady rising trend of the cloud forcing with increasing stellar flux shown in Figure 3.2c corresponds to the increasing day-side cloud cover seen in Figure 3.3b. At all stellar fluxes below the deglaciation point the day-side high cloud cover remains relatively stable at $\sim 40\%$. The decrease in cloud cover and associated forcing upon deglaciation is indicative of the heaviest cloud cover on our synchronously rotating planets occurring at stellar fluxes near the deglaciation threshold. Clouds are concentrated in the hottest regions of the planet, around the substellar point. Medium and low cloud cover rises with increasing instellation up to the deglaciation threshold, beyond which the low and medium cloud cover fall while high cloud cover rises. Figure 3.3c shows the night-side cloud variables. Here, we find a low cloud deck that is highly sensitive to stellar instellation. Starting with a nearly

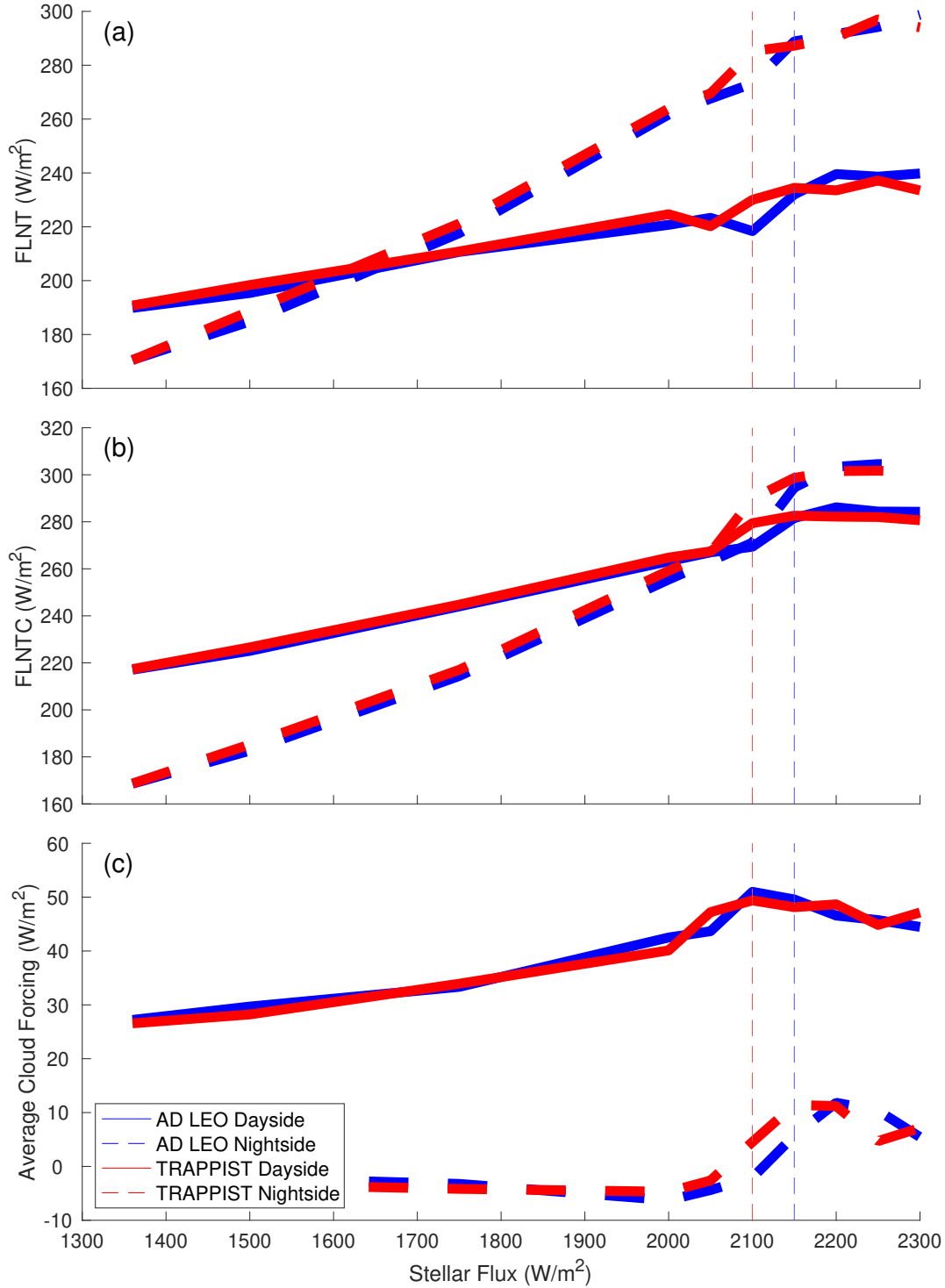


Figure 3.2: (a) The average day and night side top-of-model outgoing longwave radiation. (b) The average clearsky day and night side top-of-model outgoing longwave radiation. (c) The day and night averaged radiative cloud forcing (exact cloud positions not shown). The blue lines correspond to Earth-sized planets orbiting M3V star AD Leo, while the red lines correspond to Earth-sized planets orbiting M8V star TRAPPIST-1. The dashed vertical lines indicate the incident stellar fluxes at which the planetary night sides for both host-star spectral types fully deglaciate.

20% low cloud cover at the lowest instellation, a sharp rise in the average cover is seen all the way to the strongest night-side low-cloud cover, 100% at the deglaciation point, which coincides with the strongest cloud forcing (Fig. 2c). As the stellar flux is further increased the low cloud cover decreases due to the removal of the tropospheric cold trap. The night side has virtually no high clouds below the deglaciation threshold and there is a small increase in the medium clouds straddling the day/night side boundary with rising instellation. Planets receiving instellation beyond the deglaciation threshold exhibit progressively weaker radiative forcing as clouds are advected upwards and more medium/high clouds appear.

3.5 Discussion

The results of our simulations indicate that terminator habitability is implausible on Earth-like planets having an abundance of surface water. We find that with increasing instellation, the greenhouse warming resulting from a large water inventory overcomes the stabilizing effect of water clouds, leading to rising day-side temperatures and heat transport. The night-side water vapor begins to rise with increasing instellation below the deglaciation threshold due to vapor transported from the day sides of the planets. At the respective deglaciation thresholds of $< 2100 W/m^2$ and $2150 W/m^2$ for our TRAPPIST-1 and AD Leo planets, respectively, enough heat and water vapor are transported to the night side of the planets to completely deglaciate and remove the tropospheric cold trap on that side. Once this happens, night-side temperatures become more sensitive to increases in instellation as water vapor is now free to rise into the atmosphere, increasing the longwave heating rate. This effect combined with the heat transported from the day side results in much smaller day-night temperature contrasts with rising instellation past the deglaciation threshold. The day-side temperatures exhibit weaker sensitivity to instellation and temperatures remain temperate, thus eliminating the possibility of terminator habitability on M-dwarf aquaplanets with 1-bar

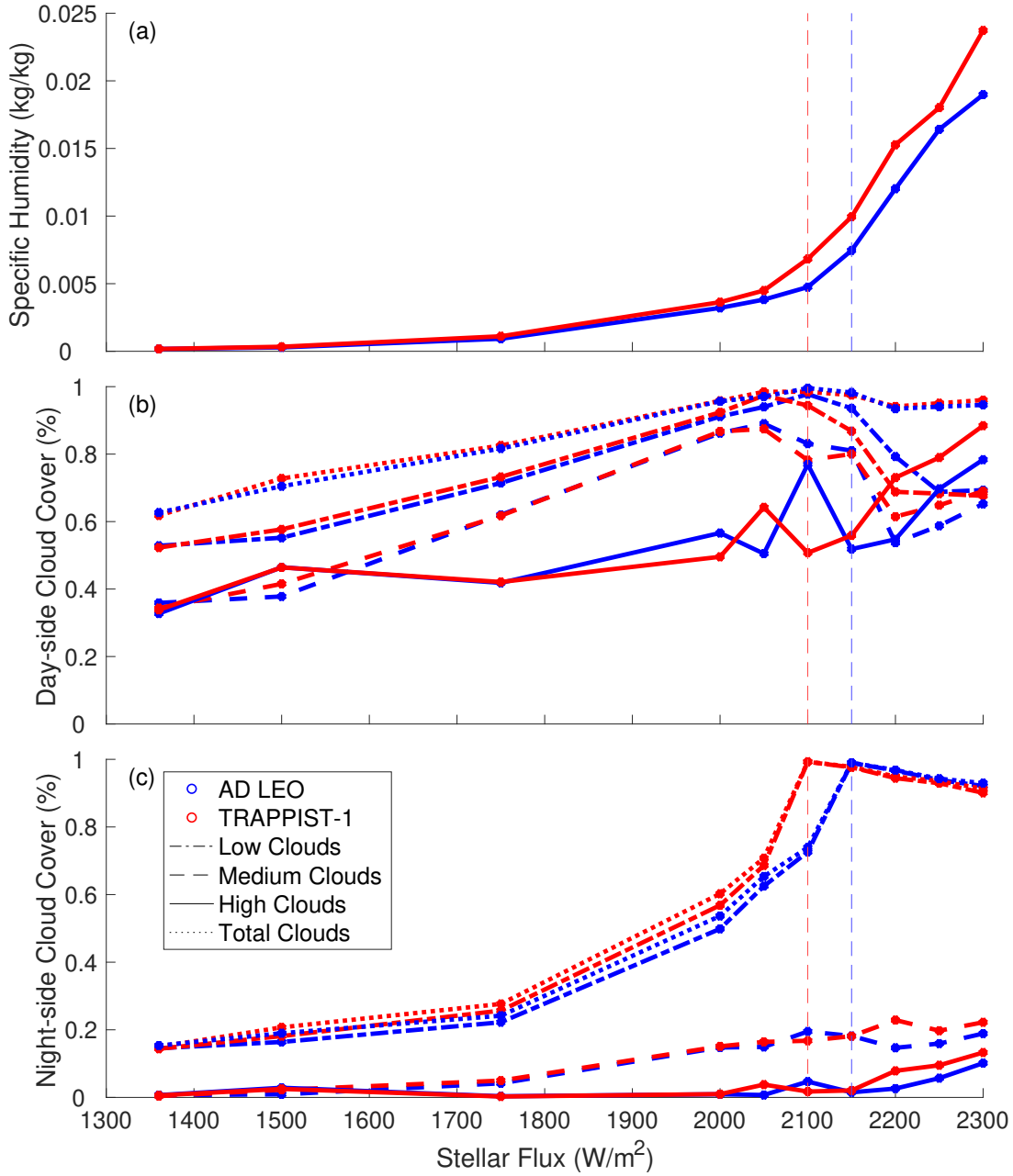


Figure 3.3: (a) The average night-side specific humidity. (b) and (c) The average day side (night side) low, medium, high and total cloud cover (%). Blue lines correspond to Earth-sized planets orbiting M3V star AD Leo, while red lines correspond to Earth-sized planets orbiting M8V star TRAPPIST-1. The dashed vertical lines indicate the incident stellar fluxes at which the planetary night sides for both host-star spectral types fully deglaciates.

surface pressures. We find that planets orbiting both host-star subspectral types deglaciate at similar instellations, and respond similarly to rising instellation, indicating that our results are robust across the M-dwarf stellar spectrum.

Terminator habitability may be possible on planets with atmospheres thinner than Earth’s if they have reduced day-night heat transport. This may lead to temperature contrasts large enough to observe temperatures above the boiling point of water at the substellar regions of a planet, while the surface on the planetary night side remains frozen. However, recent work by Zhang and Yang (2020) has shown that the effects of the background gas pressure on planetary climate of synchronous planets are non-monotonous due to a number of competing factors, which include increased lapse rate, pressure broadening of greenhouse gases’ absorption lines, weaker atmospheric circulation with increasing pressure of nitrogen gas, and a complex effect on the cloud cover.

Despite the reduced day-night heat transport and weaker atmospheric circulation, the larger water vapor capacity of a thinner atmosphere may facilitate the deglaciation of the night side at lower instellations. As with our 1 bar planets, further increases to the instellation will result in a stronger response in the specific humidity on the night side and a global runaway at a critical flux. As noted in Zhang and Yang (2020), the large water and heat capacity is the dominant warming effect on planets with surface pressures of 0.25 bar. However, somewhere in the 0.25 – 1 bar surface pressure space, a balance between the competing effects of heat capacity and atmospheric heat transport may be conducive to a sufficient day-night temperature contrast to observe terminator habitability. More work exploring this lower pressure parameter space is necessary to determine whether terminator habitability is possible on Earth-sized aquaplanets with thin atmospheres.

A sizable substellar continent could drastically reduce the atmospheric water and cloud cover [121]. It has been suggested that continents on synchronously rotating planets are more likely to congregate on the star-planet axis, so at the sub-, or anti-stellar points [217, 119]. Water

can be potentially trapped on the night side of the planet [209], further reducing the day-side water supply, especially on planets with thin Earth-like atmospheres. Additionally, with this continent, the day-side temperatures may rise much higher than on aquaplanets while the climate remains in radiative equilibrium. In such a scenario, at sufficiently high temperatures the dry day side could be rendered uninhabitable while atmospheric heat transport is significantly reduced, allowing for the existence of terminator habitability at a wider range of atmospheric thicknesses. Determining the effects of substellar continents on the possibility of terminator habitability is beyond the scope of this project, but should be explored in future research.

3.6 Conclusions

Using the CAM4 GCM, we show that terminator habitability is unlikely to exist on synchronous 1-bar Earth-like planets with a large water reservoir. Our simulations demonstrate that the strong day-night heat transport associated with large atmospheric water vapor concentrations greatly reduces the day-night temperature contrast near the inner boundary of the habitable zone, leading to global termination of planetary habitability by the runaway greenhouse. Our results are largely insensitive to host-star sub-spectral type, as planets orbiting both our early- and late-type M-dwarf stars follow a similar pattern in the evolution of the climate with increasing instellation. The day side of highly irradiated terrestrial planets is characterized by near complete cloud cover at the substellar region that spans the entire height of the atmosphere. Conversely, the night side exhibits only strong, low-level cloud cover that has nearly no effect on the overall climate, while the night side remains frozen. Planets deglacierate at instellations $50 W/m^2$ apart, at stellar fluxes of $2100 W/m^2$ and $2150 W/m^2$ for planets orbiting AD Leo and TRAPPIST-1, respectively. Deglacierated planets exhibit a sharp rise in water vapor and temperature on the planetary night side,

making the entire planet amenable to life at instellations near the threshold for the runaway greenhouse.

Chapter 4

Numerical Challenges in Modeling Gravothermal Collapse in Self-Interacting Dark Matter Halos

4.1 Abstract

When dark matter has a large cross section for self scattering, halos can undergo a process known as gravothermal core collapse, where the inner core rapidly increases in density and temperature. To date, several methods have been used to implement Self-Interacting Dark Matter (SIDM) in N-body codes, but there has been no systematic study of these different methods or their accuracy in the core-collapse phase. In this paper, we compare three different numerical implementations of SIDM, including the standard methods from the GIZMO and Arepo codes, by simulating idealized dwarf halos undergoing significant dark matter self interactions ($\sigma/m = 50 \text{ cm}^2/\text{g}$). When simulating these halos, we also vary the mass resolution, time-stepping criteria, and gravitational force-softening scheme. The

various SIDM methods lead to distinct differences in a halo’s evolution during the core-collapse phase, as each results in spurious scattering rate differences and energy gains/losses. The use of adaptive force softening for gravity can lead to numerical heating that artificially accelerates core collapse, while an insufficiently small simulation time step can cause core evolution to stall or completely reverse. Additionally, particle numbers must be large enough to ensure that the simulated halos are not sensitive to noise in the initial conditions. Even for the highest-resolution simulations tested in this study (10^6 particles per halo), we find that variations of order 10% in collapse time are still present. The results of this work underscore the sensitivity of SIDM modeling on the choice of numerical implementation and motivate a careful study of how these results generalize to halos in a cosmological context.

4.2 Introduction

Dark matter (DM) self interactions provide the means to transfer heat and mass across a halo [198]. When the self interactions are strong enough, they can impact the structure, morphology and diversity of galaxies and their satellites—see Refs. [206, 3] for reviews. This provides an exciting opportunity for Self-Interacting Dark Matter (SIDM) to be distinguished from collision-less Cold Dark Matter (CDM) through purely gravitational interactions on galactic and sub-galactic scales. Robust interpretations of such observations necessarily rely on careful modeling of galaxy evolution in these different DM frameworks. Towards this goal, this paper provides a first study of numerical challenges associated with simulating SIDM halos whose cores contract to high densities.

The heat transfer provided by collisions of DM particles allows the inner-most regions of a halo to heat up. During this core-expansion phase, the DM particles at the halo’s center acquire kinetic energy and expand their orbits. This reduces the core density for as long as heat is transferred inward [103, 235, 104, 214, 176]. Eventually, the core becomes hotter

than the outer regions, and the heat transfer flips so that heat is transferred from the isothermal core to the outer halo. This leads to the core shrinking in spatial size and increasing in density [8, 49]—a slow process because the temperature gradient in the inner halo is extremely shallow. The net effect of the shrinking core and outward heat flow is an increase in the temperature of the core as long as the system is in hydrostatic equilibrium. The increase in core temperature further facilitates the outward heat flow resulting in the runaway process called gravothermal core collapse. This process was first studied in the context of globular clusters—see e.g., Ref. [128]—and was later applied to the study of SIDM [8, 104, 51, 148, 232, 234, 230, 84, 242].

Self-scattering interactions with a cross section as small as $3 \text{ cm}^2/\text{g}$ have been shown to increase the diversity of rotation curves in the inner parts and bring them closer in agreement with observations [169, 240]. However, recent studies show that an interaction cross section larger than $10 \text{ cm}^2/\text{g}$ [94, 236, 89, 148] and as high as $100 \text{ cm}^2/\text{g}$ [32, 210, 229] at the dwarf spheroidal galaxy velocity scales of 10–30 km/s could reproduce the diversity of central densities measured in the satellite galaxies of the Milky Way. SIDM models that do not allow for core collapse are disfavored by the Milky Way satellite kinematic data [197, 195]. Core collapse in satellites could contribute to the large galaxy-galaxy strong lensing excess observed in several galaxy clusters [138, 231] and the anomalous densities of subhalos detected in galaxy-galaxy lensing [141, 36, 241]. Core collapse could additionally provide the seeds for Super Massive Black Holes (SMBH) observed at high redshift ($z \geq 7$) [161, 37, 117, 27, 54]. Such early core collapse would require a large interaction cross section, or dissipative scattering, or a more complex dark sector, e.g mirror DM [13, 97, 58, 12, 161, 27].

Modeling galaxy formation in the context of SIDM requires supplementing gravitational scattering with DM self-scattering in standard N-body codes [103, 235, 104, 214, 176, 59, 174, 173, 172, 145, 10, 33]. Three commonly used implementations include the Spline method written into Arepo [214], the Kernel-Overlap method in GIZMO [176, 174], and the Top-

Hat method [103, 235, 173, 172]. These methods differ, in part, in how they account for nearest neighbors and how they implement force softening. The authors of these codes tested the methods by verifying the scattering rates in DM halos with a Hernquist [76] or Navarro-Frenk-White (NFW) [147] profile, or by shooting individual DM particles at a uniform field of background particles. Ref. [140] performed the first comparison of the N-body codes Arepo and GIZMO in their base configuration for an isolated SIDM halo in the core-expansion phase. In their high-resolution simulations, employing fixed force softening much smaller than the DM core size, they found significant differences in the overall scattering rate between the two methods and noted up to 30% differences in their density profiles in the core-expansion phase. However, no convergence study has yet been performed that compares different SIDM implementations in the same N-body code and also pushes this comparison deep into the core-collapse phase.

In this paper, we perform a detailed comparison of the three aforementioned SIDM implementations and discuss the appropriate choices of numerical parameters and mass-resolution limitations. In particular, we consider how choices in number of particles, time stepping, and gravitational force-softening schemes impact a halo’s core density and collapse time scales. As a specific example, we focus on an isolated dwarf galaxy of mass $1.15 \times 10^9 M_\odot$ at both a high and low concentration. These two cases cover both early and late core collapse. For a cross section of $50 \text{ cm}^2/\text{g}$, we investigate how different SIDM implementations reproduce the core collapse of a DM halo by comparing the evolution of core density and velocity dispersion. As will be demonstrated, the evolution is highly sensitive to the numerical implementation of both the gravitational and self-scattering processes.

This paper is organized as follows. The details of the simulation implementation are described in Sec. 4.3. Section 4.4 discusses how halo evolution is affected by the SIDM implementation, mass resolution (number of particles), time-stepping criteria and gravitational force-softening scheme. Section 5.22 comments on how our numerical results compare with a fluid description

of core-collapsing halos. We conclude in Sec. 4.6. An appendix is included with some supplementary figures.

4.3 Simulation Framework

The DM-only halos studied in this work are evolved using the gravity-tree solver in GIZMO [78]. As a concrete case study, we consider a low- and high-concentration variant of a $M_{200} = 1.15 \times 10^9 M_\odot$ isolated halo with virial radius $R_{200} = 22.1$ kpc. The initial conditions for these halos are set using `Spheric` [63] and assume an NFW density profile with some scale radius, r_s , and density, ρ_s . All halos are exponentially truncated at $r_{\text{trunc}} = 23.6$ kpc beyond the virial radius (see Ref. [238] for details on the truncation form), similar to previous studies [239].¹ The high-concentration halo has $\rho_s = 1.04 \times 10^8 M_\odot/\text{kpc}^3$ and $r_s = 0.715$ kpc, which corresponds to a concentration of $c_{200} = 31$. The low-concentration halo has parameters of $\rho_s = 2.73 \times 10^7 M_\odot/\text{kpc}^3$ and $r_s = 1.18$ kpc, corresponding to $c_{200} = 19$. These halo parameters result in a core-collapse time of ~ 3.5 (14) Gyr for the high (low) concentration case, providing a good example of early versus late collapse in cosmological time.

For the two halos under consideration, we vary several different inputs to the numerical modeling, including the DM scattering implementation (Sec. 4.3.1), force-softening scheme (Sec. 4.3.2), and time-stepping criteria (Sec. 4.3.3). Table 5.1 summarizes the simulations used in this work. The halos are run at low, medium, and high resolution, which correspond to $N_p = 3 \times 10^4$, 5×10^5 , and 10^6 total gravitationally-bound particles in the halo, respectively. Additionally, all simulations are run with the same number of cores to minimize the influence of hardware on the results.

¹Ref. [148] found that the truncation radius has no effect on a halo’s evolution so long as it is larger than several times the scale radius.

c_{200}	r_s [kpc]	ρ_s [M_\odot/kpc^3]	N_p	$h_{g,i}$ [kpc]	$h_{s,i}$ [kpc]	κ	η
19 (low)	1.18	2.73×10^7	3×10^4	adaptive	adaptive	0.02 & 0.002	0.02
19 (low)	1.18	2.73×10^7	5×10^5	adaptive	adaptive	0.02 & 0.002	0.02
19 (low)	1.18	2.73×10^7	1×10^6	adaptive	adaptive	0.02 & 0.002	0.02
19 (low)	1.18	2.73×10^7	3×10^4	adaptive	adaptive	0.002	0.002
19 (low)	1.18	2.73×10^7	5×10^5	0.0353	adaptive	0.002	0.002
19 (low)	1.18	2.73×10^7	1×10^6	0.0353	adaptive	0.002	0.02
31 (high)	0.715	1.04×10^8	3×10^4	adaptive	adaptive	0.002	0.02
31 (high)	0.715	1.04×10^8	5×10^5	adaptive	adaptive	0.002	0.02
31 (high)	0.715	1.04×10^8	1×10^6	adaptive	adaptive	0.002	0.02

Table 4.1: Halo and simulation parameters used in this work, including the concentration ($c_{200} = R_{200}/r_s$), NFW scale radius (r_s) and density (ρ_s), number of particles (N_p), force-softening length for gravitational ($h_{g,i}$) and self ($h_{s,i}$) interactions, time-stepping criterion (κ), and tolerance parameter (η). The parameter κ corresponds to the maximum probability that two particles scatter with each other in a given time step and is defined in Sec. 4.3.3. The parameter η captures the fraction of the gravitational softening length that a particle can travel in a specified time step; it is discussed in Sec. 4.3.2. All of the listed configurations are simulated using the three SIDM methods described in Sec. 4.3.1: Kernel Overlap, Spline, and Top Hat.

4.3.1 Implementation of Dark Matter Scattering

This study takes an SIDM cross section per unit DM particle mass of $\sigma/m = 50 \text{ cm}^2/\text{g}$ as a benchmark scenario. The interactions are implemented using three different SIDM methods from the literature: the Kernel-Overlap, Spline, and Top-Hat methods. The Kernel-Overlap method is available in the public version of GIZMO, while the Top-Hat and Spline methods have been re-implemented for this work.

Kernel-Overlap Method

The Kernel-Overlap procedure applies a scattering method derived from the collisional Boltzmann equation, treating each particle as a discrete element of the phase-space distribution of the DM halo—see Ref. [176] Appendix A for a full derivation. Briefly, a particle i at position \mathbf{r} is associated with the density kernel $W(r, h_i)$ with “smoothing length” h_i , which can be thought of as the radius over which the particle is smeared to give it some non-zero volume. The distance h_i must be chosen carefully; setting it too large leads to non-local interactions, while setting it smaller than the mean particle spacing leads to non-physical, two-body relaxation effects. Throughout, we use $h_{s,i}$ to refer to the smoothing length for the self interactions, distinguishing it from $h_{g,i}$, the gravitational smoothing length (discussed in more detail in Sec. 4.3.2).

In this framework, the scattering rate of some particle i from a target particle j is given by

$$\Gamma_{ij} = (\sigma/m) m_p v_{\text{rel}} g_{ij}, \quad (4.1)$$

where m_p is the mass of the DM simulation particle, $v_{\text{rel}} = |\mathbf{v}_i - \mathbf{v}_j|$ is the relative velocity of the two particles, and g_{ij} is a number-density factor derived from the density kernel of

the respective particles:

$$g_{ij} = \int d^3\mathbf{x} W(|\mathbf{x}|, h_{s,i}) W(|\mathbf{x} + \delta\mathbf{x}_{ij}|, h_{s,j}) , \quad (4.2)$$

where $h_{s,i(j)}$ is the self-interaction smoothing length for the $i^{\text{th}}(j^{\text{th}})$ particle. The angular integral is taken over the entire volume of the kernel and $\delta\mathbf{x}_{ij}$ is the distance between the two particles. $W(r, h_i)$ is generally chosen to be the cubic-spline kernel:²

$$W(r, h_i) = \frac{8}{\pi h_i^3} \begin{cases} 1 - 6\left(\frac{r}{h_i}\right)^2 + 6\left(\frac{r}{h_i}\right)^3 & 0 \leq \frac{r}{h_i} \leq \frac{1}{2} \\ 2\left(1 - \frac{r}{h_i}\right)^3 & \frac{1}{2} < \frac{r}{h_i} \leq 1 \\ 0 & \frac{r}{h_i} > 1. \end{cases} \quad (4.3)$$

In principle, other kernel forms could be used here, which may affect the simulation results. As such, our results pertain specifically to this choice of the kernel. GIZMO approximates the integral in Eq. 4.2 by taking the average of the particle smoothing lengths and treating the result as a constant length, $h_{\text{avg}} = (h_{s,i} + h_{s,j})/2$, in the kernel expression. With this simplification, a table of $g_{ij}(\delta x_{ij})$ can be generated at the start of a simulation and the integral is simply a function of $\delta x_{ij}/h_{\text{avg}}$.

Given Eq. (4.1), the probability that particle i scatters in a time step dt_i is

$$P_{ij} = \Gamma_{ij} dt_i \quad (4.4)$$

with the total probability of interaction between the particles being

$$P_{ij} = P_{ji} = \frac{P(i|j) + P(j|i)}{2}. \quad (4.5)$$

²To ensure the resulting scattering probability matches Eq. 4.1, the kernel is normalized such that $4\pi \int_0^h dx x^2 g_{ij}(x) = 1$.

Whether the pair of particles actually scatter is determined by drawing a random number $R \in [0, 1]$ and comparing it to the probability. If $R < P_{ij}$, then a kick is applied to both particles in the center-of-mass frame. The post-interaction velocities are:

$$\mathbf{v}'_i = \mathbf{v}_c + \frac{m_j}{m_j + m_i} v_{\text{rel}} \hat{\mathbf{e}} \quad \mathbf{v}'_j = \mathbf{v}_c - \frac{m_i}{m_i + m_j} v_{\text{rel}} \hat{\mathbf{e}}, \quad (4.6)$$

where \mathbf{v}_c is the center-of-mass velocity and $\hat{\mathbf{e}}$ is a random direction.

Spline Method

The Spline method, based on the approach described in Ref. [214], is unique because the scattering is not determined on a pair-by-pair basis. The total probability of scattering P_i is calculated first and then a neighbor is chosen to scatter with. This total probability is built up from the individual interaction probabilities between two particles:

$$P_{ij} = (\sigma/m) W(\delta x_{ij}, h_{s,i}) m_p v_{\text{rel}} dt_i, \quad (4.7)$$

where the cubic-spline kernel is taken for $W(r, h_{s,i})$. For a given particle i , the total probability of scattering is the sum

$$P_i = \sum_{j=0}^N \frac{P_{ij}}{2} = \sum_{j=0}^N (\sigma/m) W(\delta x_{ij}, h_{s,i}) \frac{m_p}{2} v_{\text{rel}} dt_i, \quad (4.8)$$

where N is the discreet number of neighbors within the kernel length, and the factor of two in the denominator arises because two particles participate in a scattering event. A collision occurs if $R < P_i$, for some uniform random number $R \in [0, 1]$. To select the nearest neighbor that participates in the scattering event, all the nearby particles are ranked by their distance to i . The target for the collision is chosen as the first particle l that satisfies $R < \sum_j^l P_{ij}$. A velocity kick is then applied following Eq. 4.6.

Top-Hat Method

The third DM collision method considered here was first introduced in Ref. [103]. It differs from the previous two approaches because it uses a top-hat rather than a cubic-spline kernel. As such, there is no explicit weighting of the scattering probability by the particle separation. In this case, the probability of scattering between a pair of particles is

$$P_{ij} = \frac{(\sigma/m) m_p v_{\text{rel}} dt_i}{\frac{4}{3}\pi h_{s,i}^3}. \quad (4.9)$$

A DM-DM scattering event occurs if $R < P_{ij}$ at a given time step, where $R \in [0, 1]$ is a uniform random number. The final particle kinematics is again set by Eq. 4.6.

4.3.2 Implementation of Force-Softening Scheme

The choice of force-softening length, h_i , plays a key role in determining the robustness of the SIDM halo evolution. If the force softening is adaptive, the scale h_i is determined by

$$\frac{4\pi}{3} h_i^3 \sum_{j=1}^N W(\delta x_{ij}, h_i) = N_{\text{eff}}, \quad (4.10)$$

where N_{eff} is the effective number of neighbors [201, 78, 80]. We set a minimum softening of $h_i = 3$ pc for all adaptive runs. For the cubic-spline kernel, $N_{\text{eff}} = 32$ is the standard choice in GIZMO, providing a good balance between computational expense and accuracy [80].

In this work, adaptive softening is always used for self interactions and is the default for gravitational interactions ($h_i = h_{g,i} = h_{s,i}$ in Eq. (4.10)). However, Sec. 4.4.4 also explores the effect of using a fixed gravitational softening length for the low-concentration halo. The fixed force softening (Plummer equivalent $h_{g,i} = 2.8\epsilon$ for cubic spline) is determined using

the criteria of Ref. [239], which is based on the constraints previously described in Ref. [212]:

$$\epsilon = r_s \left[\ln(1 + c_{200}) - \frac{c_{200}}{1 + c_{200}} \right] \sqrt{\frac{0.32 (N_p/1000)^{-0.8}}{1.12 c_{200}^{1.26}}}. \quad (4.11)$$

This results in softening values much smaller than the criterion of Ref. [164], but comparable to values determined by the adaptive softening algorithm, i.e. $\epsilon \sim 10$ pc. In general, the gravitational softening length should have minimal direct impact on the halo evolution as it is at least several times smaller than the core size. For the low-concentration halo, Eq. 4.11 yields $\epsilon = 12.6$ pc, which is more than an order-of-magnitude smaller than the core size until far into core collapse.

4.3.3 Implementation of the Time-Stepping Criterion

The time step, dt_i , is a key parameter to set when initializing an SIDM simulation run. Considerations of a particle's gravitational acceleration motivates setting the time step of particle i as

$$dt_i = \sqrt{\frac{2\eta h_{g,i}}{a}}, \quad (4.12)$$

where a is the magnitude of the acceleration that the particle experiences. The tolerance parameter, η , is a dimensionless number that describes the fraction of the force-softening length that the particle is allowed to move in the given time step. The default value in GIZMO is $\eta = 0.02$ [78]. In this work, we use $\eta = 0.02$ as the baseline scenario, but also consider $\eta = 0.002$.

However, one must also take into account the number of scattering events that occur between two DM particles in a single simulation time step. If a particle scatters multiple times in dt_i ,

and on different CPUs, energy and momentum may not be conserved. Therefore, dt_i should be small enough that the probability of multiple scatters is itself small.

For both the Kernel-Overlap and Top-Hat methods, a time-stepping criterion is applied that requires $P_{ij} < \kappa$, where κ is the maximum probability of scattering for a pair of particles.³ In practice, this means that

$$\Gamma_{ij}(\sigma/m, h_{\text{avg}}) dt_i < \kappa. \quad (4.13)$$

We consider two possible limits for the time-stepping criterion: $\kappa = 0.02$ and 0.002 . By default, $\kappa = 0.2$ [176] in GIZMO and $\kappa = 0.02$ in Arepo [214]. As will be discussed in Sec. 4.4.3, the difference between a 2% and 0.2% probability is enough to generate noticeable differences in the late-time evolution of an SIDM halo.

The time-stepping criterion will be different for the Spline method, given that the probability that particle i scatters depends on its nearest neighbors. In this case, the constraint becomes

$$\sigma \rho_{\text{loc}} v_{\text{loc}} dt_i < \kappa, \quad (4.14)$$

where v_{loc} is the local velocity dispersion, which is estimated as the maximum relative velocity between a neighbor and particle i —see Refs. [201, 78]—and the local density is

$$\rho_{\text{loc}} = \sum_{j=0}^N m_{\text{p}} W(\delta x_{ij}, h_{s,i}). \quad (4.15)$$

In practice, the value chosen for dt_i is the minimum of the two estimated with Eq. 5.15 and Eq. 4.13 (or Eq. 5.16). This ensures that the time stepping is small enough to address

³For comparison purposes, it is useful to implement a formalism for which the time steps across SIDM implementations are equivalent for a given choice of κ . For this reason, we use Eq. (4.13) for both Kernel Overlap and Top Hat.

concerns regarding both the gravitational and self interactions.

4.3.4 Characterization of the Halo Core

For the purposes of this study, it is necessary to characterize halo properties such as the central density and core size. To recover a density profile for a halo, the location of its center must be known. To determine this, we calculate the center-of-mass of the particles with the highest local densities, as determined by the estimation of ρ_{loc} in Eq. (4.15) and assuming a cubic-spline kernel. The number of particles used for this evaluation is resolution-dependent. For the low-, medium- and high-resolution simulations, we choose 200, 3000, and 6000 particles, respectively. In general, the center-of-mass of the entire halo does not coincide with the center-of-mass of the halo’s core because, over time, the core shifts relative to the outer regions of the halo, especially for the low-resolution simulations. Using the core’s center-of-mass allows for a more reliable determination of the core density and velocity dispersion profiles.

Once the core’s center-of-mass is determined, the particles in the halo are divided into 100 evenly-spaced radial logarithmic bins for which the density and velocity dispersion are obtained. To quantify the core density and size, the following density profile is fit to the inner region of the halo,

$$\rho(r) = \frac{\rho_{\text{core}}}{(1 + (r/r_0)^2)^{3/2}}, \quad (4.16)$$

where ρ_{core} is the core density and r_0 is the characteristic radius beyond which the slope of the log profile transitions from a constant to -3 . This density profile is a good approximation to the isothermal density profile in the inner regions. The fitting is done with a non-linear least-square method. However, the outer slope of this profile will not hold far outside of the core, where the slope of the log profile transitions to -2 . For this reason, we determine appropriate

fitting boundaries at every simulation snapshot. First, the central density ρ_{core} is estimated by averaging the local densities of the 200 central-most particles and then the profile is fit out to the radius where the density drops to $\rho_{\text{core}}/5$. We define the core radius, r_{core} , as the radius where the density drops to half the core density, which implies $r_{\text{core}} = r_0 \sqrt{2^{-2/3} - 1}$. Given the expectation that the core is isothermal throughout the halo’s evolution, we compute the instantaneous core velocity dispersion using all the particles within r_{core} and relate the 3D and 1D dispersions assuming an isotropic velocity distribution, $v_{\text{core},3\text{D}}^2 = 3v_{\text{core}}^2$.

4.4 Numerical Effects on SIDM Halo Evolution

This section explores how various numerical implementations of an N-body code affect the evolution of an SIDM halo. In particular, we consider effects of the SIDM implementation method (Kernel Overlap, Spline, or Top Hat), the numerical resolution, the gravitational force softening, and the time-stepping criterion. Each of the following subsections examines the effects of these variations on outputs such as the density profile evolution or the total energy of the system.

4.4.1 SIDM Methods

One of the main goals of this study is to compare between different SIDM implementation methods. Fig. 4.1 shows the core density normalized to the NFW scale density, $\rho_{\text{core}}/\rho_s$ (top panels), and core velocity dispersion normalized to the maximal circular velocity of the halo, $v_{\text{core}}/v_{\text{max}}$ (bottom panels), for the Spline (red), Kernel-Overlap (blue) and Top-Hat (green) methods. For each curve, time is plotted in units of the thermal relaxation timescale of the halo, t/t_0 , where $t_0 \equiv (\sqrt{16/\pi}\rho_s v_0 \sigma/m)^{-1}$ and $v_0 \equiv \sqrt{4\pi G \rho_s r_s^2}$ [9, 148]. Shown on the same plot are variations on the number of particles, the time-stepping criterion, and the

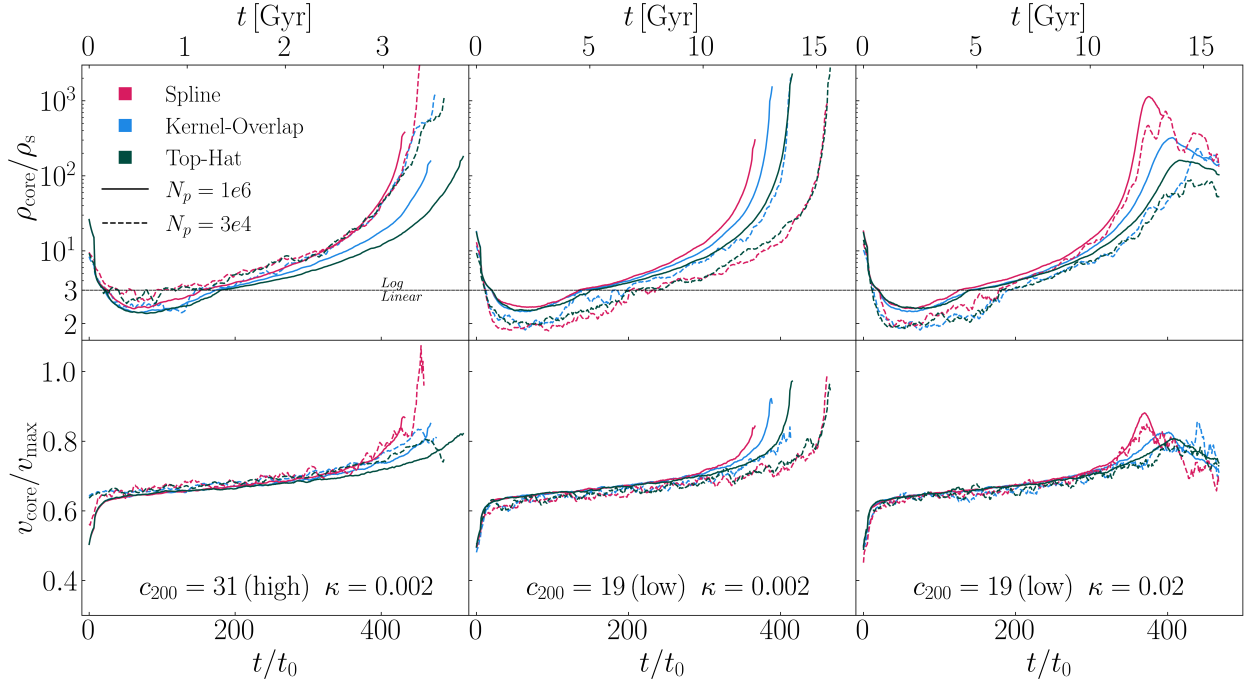


Figure 4.1: The evolution of a $1.15 \times 10^9 M_\odot$ halo with either a $c_{200} = 19$ or 31 concentration, assuming a self-interaction cross section of $\sigma/m = 50 \text{ cm}^2/\text{g}$. The low-concentration halo, which collapses late in cosmological time, is generated for both $\kappa = 0.002$ and 0.02 . The high-concentration halo, which collapses earlier, is only generated for $\kappa = 0.002$. The halo evolution is shown as a function of dimensionless time, normalized in terms of the thermal relaxation time of the halo, t_0 . The top axis provides the dimensionful time in Gyr. **Top:** The evolution of core density, ρ_{core} , normalized to the NFW scale radius, ρ_s . Note the two vertical axes: a linear (log) scale is used for densities below (above) $3\rho_s$. Results for the Spline, Kernel-Overlap, and Top-Hat SIDM implementations are shown in red, blue, and green, respectively. The solid (dashed) lines correspond to the high (low)-resolution simulations. **Bottom:** The evolution of velocity dispersion, v_{core} , normalized to the halo’s maximum velocity, v_{max} . All plotted curves have been smoothed by averaging over the six nearest snapshots, which span about $10t_0$, with the exception of very early or late times where the halo evolution is rapid and no smoothing is necessary. For the high-resolution simulations, all three SIDM methods predict similar evolution during core formation, but diverge during core collapse. Specifically, the Spline method leads to the most rapid halo evolution, while the Top-Hat method leads to the slowest. The low-resolution simulations show considerable variation in the minimum density, which ultimately affects the core-collapse timescale. As discussed in Sec. 4.4.2, this is traced back to numerical noise in the initial conditions. Lastly, simulations with $\kappa = 0.02$ experience a failure at late times where core-collapse reverses, regardless of the SIDM method and resolution. These results pertain specifically to halos simulated with adaptive force softening for gravity.

concentration of the halo used for the initial conditions of the simulation. The effects of some of these variations will be discussed below.

For all cases plotted in Fig. 4.1, the general behavior of the density evolution follows the characteristic trajectory expected from the SIDM fluid model [9, 104, 51, 148, 155, 234, 84]. In the initial stages of halo evolution, heat flows inwards and the core grows in size until it reaches a maximum radius, corresponding to some minimum central density. At this point, the central region of the halo is much hotter than its surroundings and eventually heat flow reverses direction, triggering the onset of runaway core collapse. During this final stage, the core rapidly shrinks in size and increases in both temperature and density. However, as is evident from Fig. 4.1, the detailed features of this evolution can vary significantly depending on the numerical implementation.

A general finding is that during the core-expansion phase, the core temperature is more robust than the core density to the different implementations and resolutions and always gives results that are close to the expectation from the fluid approach to within about $2\%v_{\max}$ (this will be further discussed below). The different implementations do significantly affect the core density during core expansion, the general trend being that simulations for which the minimum core density is larger collapse faster (and vice-versa). Thus, capturing physical SIDM behavior at early times in a halo’s evolution significantly affects the late-time behavior.

In all high-resolution simulations, the Spline method produces the earliest core collapse, followed by the Kernel-Overlap and then the Top-Hat method. To quantify this comparison, one can define the collapse time, t_{coll} , as the time at which the core density reaches 100 times the scale density, $\rho_{\text{core}}(t_{\text{coll}}) \equiv 100\rho_s$ (evolving halos to higher core densities involves significantly higher computational cost). For the high-concentration halos, the collapse time is $t_{\text{coll}} \approx 416t_0, 461t_0$, and $500t_0$ for the Spline, Kernel-Overlap, and Top-Hat method, respectively. For the low-concentration halos simulated with $\kappa = 0.002$, $t_{\text{coll}} \approx (338\text{--}394)t_0$, depending on the SIDM method. Holding all other variables constant, the higher $\kappa = 0.02$

simulations tend to collapse $\sim 2\%$ faster. Additionally, for some cases, the behavior of both central density and velocity dispersion stall and become non-physical at late times.

One possible cause for the differences in halo evolution is the scattering rate of particles within the simulation. Theoretically, the rate is expected to be,

$$\Gamma_{\text{exp}} = \int_V \frac{\rho(\mathbf{x})^2}{2m_{\text{p}}^2} \langle \sigma v_{\text{rel}} \rangle dV, \quad (4.17)$$

where $\rho(\mathbf{x})$ is the halo's density profile and $\langle \sigma v_{\text{rel}} \rangle$ is the thermal average of the cross section times the relative velocity. The thermal averaging can be calculated by assuming that all interacting particles have a Maxwell-Boltzmann distribution of the form $f(\mathbf{v}) = [1/(2\pi v_r^2)]^{3/2} e^{-(\mathbf{v}/v_r)^2/2}$ (where $v_r(\mathbf{x})$ is the position-dependent 1D radial velocity dispersion of the halo), which for a constant cross section just gives $\langle \sigma v_{\text{rel}} \rangle = 4/\sqrt{\pi} \times \sigma v_r$. To estimate Γ_{exp} , we spline the density and dispersion profiles for each simulation snapshot, which is taken every t_0 to capture the halo's evolution during core collapse, and numerically integrate over the entire simulation volume. The expected scattering rate can then be compared to the scattering rate observed in the simulations. To obtain this rate, we count the number of scattering events, N_{scat} , within each time interval, t_0 , in the entire simulation volume, and take $\Gamma_{\text{obs}} = N_{\text{scat}}/t_0$.

For all simulations run in this study, Γ_{exp} and Γ_{obs} agree with each other to within about 10% and are remarkably constant in time. In particular, for the highest-resolution simulations, the ratios are constant throughout the entire evolution with the exception of the last few snapshots that are deep in the core-collapse regime (when Γ_{obs} is extremely sensitive to the rapid evolution). These ratios are $\Gamma_{\text{obs}}/\Gamma_{\text{exp}} \approx 1.08, 1.06,$ and 1.02 for the Kernel-Overlap, Spline, and Top-Hat implementations, respectively (see Fig. A1 for additional details). In this regard, we note that Ref. [140] found larger differences in the scattering rates between the Arepo and GIZMO codes, and these differences were cross-section dependent. We are

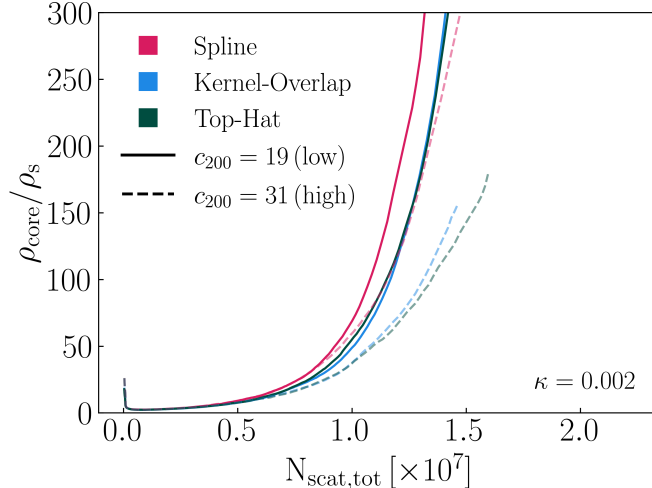


Figure 4.2: The evolution of core density as a function of the total scattered mass for the high-resolution simulations with $\kappa = 0.002$. The solid opaque lines correspond to the low-concentration halo, while the dashed lines are for the high-concentration halo. The Kernel-Overlap and Top-Hat methods achieve the same core density at equivalent scattered mass, while the Spline method achieves the same core density with less scattering. These results pertain specifically to halos simulated with adaptive force softening for gravity.

unable to make a direct comparison to these results because GIZMO and Arepo are different in more ways than just the SIDM implementations. Additionally, the SIDM kernels we use are adaptive, while Ref. [140] used a fixed softening for SIDM that was a fraction of the gravitational force softening (which was also not adaptive).

To study whether the different scattering rates contribute to the variations in evolution for different SIDM implementations, one could think of the cumulative number of scattering events at any given time in the simulation as a universal clock. Namely, since different SIDM implementations have different instantaneous scattering rates, it is plausible that evolution would be equivalent if plotted as a function of the cumulative number of scattering events instead of actual simulation time. To test this, the total number of scattering events is computed, $N_{\text{scat,tot}}(t) \equiv \sum_{t_i=0}^t N_{\text{scat}}(t_i)$ (where t_i denotes the time intervals between the first snapshot and any snapshot at time t). These values differ slightly between the different SIDM implementations. For example, at the time of maximal core (approximately $\sim 70t_0$), $N_{\text{scat,tot}}(70t_0) = 9.40 \times 10^5$, 9.25×10^5 and 8.69×10^5 for the Kernel-Overlap, Spline, and

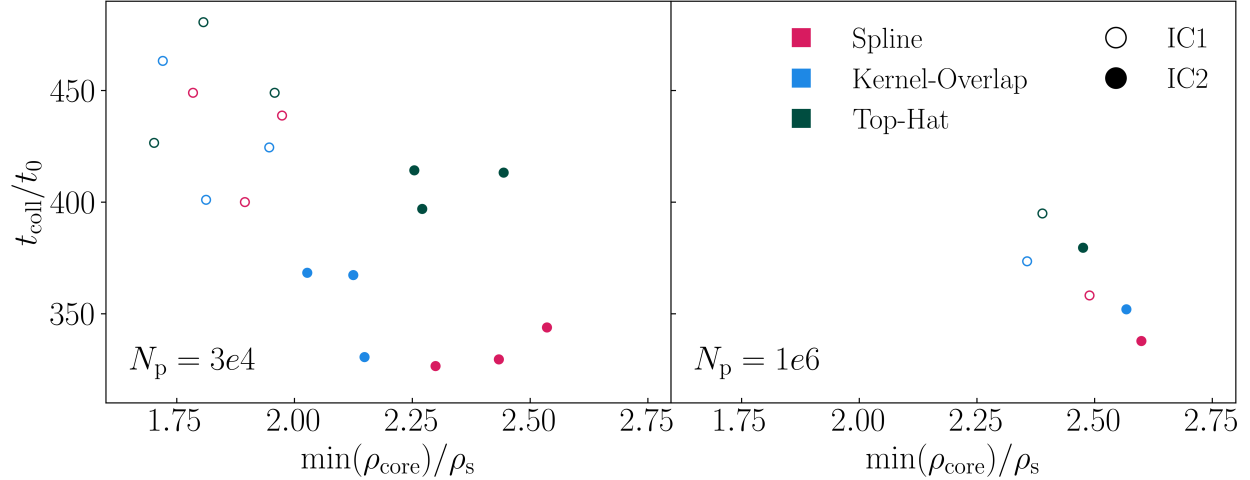


Figure 4.3: The collapse time, t_{coll} , in units of relaxation time plotted as a function of minimum core density, normalized to ρ_s . Results are shown for the low- (left panel) and high-resolution (right panel) simulation of the low-concentration halo with $\kappa = 0.002$. They are plotted for two different realizations of the NFW initial conditions of the halo (IC1 and IC2), shown by the empty/filled circles. For a given initial condition and SIDM method (indicated by color), each low-resolution halo is re-simulated three times to test reproducibility. The dominant source of scatter in the minimum core density and collapse time for the low-resolution simulations is the numerical noise in the generation of the initial conditions. These results pertain specifically to halos simulated with adaptive force softening for gravity.

Top-Hat implementations, respectively. Halo evolution as a function of $N_{\text{scat,tot}}$ is plotted in Fig. 5.3 for the highest-resolution runs and for both high- and low-concentration simulations with $\kappa = 0.002$. Using this variable instead of time brings the Kernel-Overlap and Top-Hat methods into close agreement, while the Spline method still collapses earlier than the others. This suggests that, while differences in the scattering rates between the SIDM implementations could explain some of the variations in collapse times, additional factors must also be affecting the results. In what follows, we study some additional aspects of core-collapsing SIDM simulations.

4.4.2 Mass Resolution and Initial Conditions

The total number of particles in a halo must be large enough to ensure that halo properties are well resolved and that numerical noise does not have an effect on the halo’s evolution. This subsection explores the effects of reducing the particle count below 10^6 per halo. The most dramatic differences occur for the lowest-resolution halos in the suite, the results of which are indicated by the dashed lines in Fig. 4.1 (curves for medium-resolution simulations are not shown because they are nearly identical to those of the high-resolution simulations). These low-resolution halos exhibit significant variation in both the minimum core density as well as the core-collapse time. For example, the low-concentration halo has $\min(\rho_{\text{core}}) \approx (1.6\text{--}2.0)\rho_s$ for the low-resolution runs, while the range narrows to $\approx (2.3\text{--}2.5)\rho_s$ for the high-resolution runs (see Fig. 4.3).

In general, for cases where the cores are larger and less dense, the low-resolution halos take longer to core collapse than their higher-resolution counterparts. For the low-concentration halo simulated with $\kappa = 0.002$, the core-collapse times are $t_{\text{coll}} \approx 450t_0$ for the Spline and Top-Hat method and $t_{\text{coll}} \approx 400t_0$ for the Kernel-Overlap case. As mentioned above, the early-evolution of the halos ultimately impacts its late-time evolution. These effects are due to numerical noise in the initial conditions and are not physical.

To further test numerical noise, Fig. 4.3 plots the collapse time and minimum core density for multiple realizations of the low-concentration halo with $\kappa = 0.002$. The left panel corresponds to low resolution and the right panel to high resolution. In each case, open circles correspond to the baseline NFW initial conditions used in this work (IC1) while the filled circles correspond to a separate, independent set of initial conditions (IC2). For the low-resolution case only, and for a given initial condition and SIDM implementation, each halo is simulated three times to test whether additional numerical effects, such as issues with random seed generators, are at play. This is not done for the high-resolution simulations

due to computational costs.

As the left panel of Fig. 4.3 demonstrates, there are at least two sources of variability for the low-resolution simulations. A dominant source of uncertainty is related to the choice of initial conditions, which leads to variability of order 30% in both collapse time and minimal core density. A sub-dominant source of uncertainty, which is likely due to random number seed generation in the code (although we cannot isolate the effect explicitly), leads to $\sim 10\%$ variations in collapse time and $\sim 5\%$ variations in minimal central density. The right panel shows results for the higher-resolution simulations. Clearly, the spread in these results, corresponding to varying initial conditions, is now much smaller, of order 10% for both collapse time and minimal core density.

As discussed earlier, the minimal core density and collapse times are in fact related to each other since larger minimal core densities generally correspond to earlier collapse times. This is somewhat expected since the instantaneous collision timescale in the core is proportional to $(\rho_{\text{core}} v_{\text{core}})^{-1}$. Numerically, we find that the values of v_{core} at the time of maximal core are approximately constant when varying SIDM methods and initial conditions, and therefore one might expect that $t_{\text{coll}} \propto \min(\rho_{\text{core}})^{-1}$ which is approximately the scaling observed in Fig. 4.3.

Given the results of this section, from this point onward, the analyses focus solely on the high-resolution simulations.

4.4.3 Time-Stepping Criterion

Energy non-conservation due to numerical processes plays a key role in SIDM halo evolution. The top panel of Fig. 4.4 plots the evolution of the total energy,⁴ normalized to the initial

⁴For the following discussion, “total energy” refers to the total potential and kinetic energy of all the particles in the simulation.

energy, E_0 , of each simulated halo as a function of core density. As the halo evolves in time, it moves clockwise along each curve, starting from the initial state (marked with an ‘x’), then moving towards lower core density through core expansion, and then towards higher core density in the subsequent core collapse. For the $\kappa = 0.002$ example (top left), the energy is well-conserved ($E/|E_0| \approx -1$) while $\rho_{\text{core}} \approx 10\rho_s$. Far into the core-collapse regime, though, the different SIDM implementations result in different energy evolution. Simulations run with the Spline method show the largest energy loss, while the Top-Hat simulations exhibit the least energy loss. At very late times, some of the halos start to exhibit significant gains in energy.

This behavior is even more apparent in the bottom row of Fig. 4.4, which shows the energy evolution as a function of time. Changes in energy are driven by two distinct numerical effects that compete with each other. The first is energy loss from the implementation of gravitational scattering. This effect should be present even for a CDM simulation, which is indeed the case, as demonstrated by the solid black lines in the bottom row of Fig. 4.4. The second main effect arises from the implementation of the self interactions. The additional energy gains that result from this effect are apparent in the bottom panel of Fig. 4.4, where all three SIDM lines differ from the black CDM expectation. In the initial stages of core collapse, we observe a $\sim 1.0\text{--}1.3\%$ change in energy for the $\kappa = 0.002$ halo. SIDM offsets the energy loss from gravitational scattering, bringing the halo closer to its initial energy inventory. However, this does not improve the accuracy of the simulations as artificially adding and removing energy throughout the halo influences its thermal evolution unpredictably.

While these sub-percent changes to the total energy may seem negligible, any numerical energy loss during core collapse is effectively an additional heat source in the central region of the halo where the vast majority of the self interactions take place. As the energy decreases, the potential well of the halo deepens and mass is dragged towards the center of the halo, effectively accelerating core collapse. From Fig. 4.4, it is clear that the Spline method heats

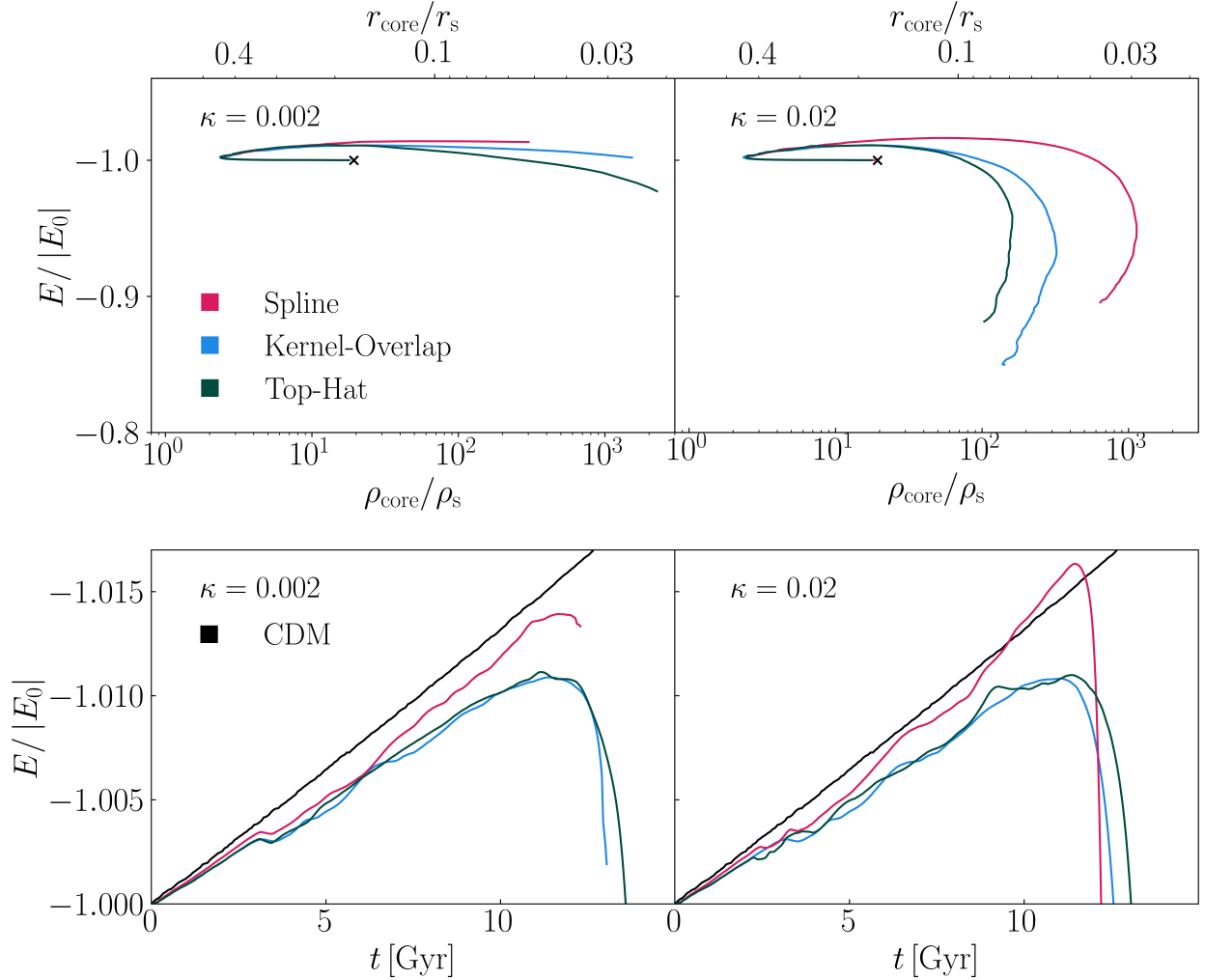


Figure 4.4: Top: The evolution of total energy versus core density for the low-concentration halo with $\kappa = 0.002$ and 0.02 . Plotted in this space, the halo’s energy evolves clockwise with time. This evolution is characterized by a phase of core expansion at constant energy followed by the halo’s energy becoming more negative, i.e. losing thermal energy, from the time of core formation to core collapse. Simulations with $\kappa = 0.02$ exhibit a critical failure of energy conservation once core densities reach $50\text{--}500\rho_s$ (depending on SIDM method), where both the kinetic and potential energy is rapidly lost. Generally, the Spline method experiences this failure at much higher core densities than the other two methods. Bottom: The evolution of halo energy over time. For comparison, the evolution of a CDM halo is plotted in black. The Spline method produces energy evolution closest to the CDM halo at times past the “maximum core”, showing that this method produces the least net energy gain due to the DM scattering. These results pertain specifically to halos simulated with adaptive force softening.

halos the most in the initial stages of core collapse, followed by the Kernel-Overlap and Top-Hat methods. This explains the behavior noted in Fig. 4.1, where the Spline method results in the fastest core-collapse times.

Conversely, any numerical effects that lead to artificial gains in energy will effectively cool the system, delaying core collapse. At very late times in the halo evolution, all the simulations begin to gain a lot of energy, which causes the core to expand again and the entire halo to become less gravitationally bound. For the $\kappa = 0.002$ halo, this cooling does not have a noticeable effect on the core’s evolution. However, for the $\kappa = 0.02$ example, the degree of numerical cooling is so significant that it causes the core-collapse process to completely reverse. The right-most column of Fig. 4.1 shows the case of $\kappa = 0.02$ for the low-concentration halo. For all three SIDM implementations, the density growth slows down and experiences some fluctuations when the core density exceeds $\sim 200\rho_s$. Looking at the evolution of the central velocity dispersion, it is clear that something is going wrong because the dispersion starts to decrease just as the growth of core density begins to fluctuate. Beyond this point, the core collapse halts and reverses with the density dropping by as much as a factor of 10 by the end of the simulation run. At the same time, the central velocity dispersion falls back down to $\sim 0.7v_{\max}$, virtually reversing the total heat gain since the start of core collapse. In general, the Top-Hat method fails at lowest core density, while the Spline method fails at the highest. From the right panel of Fig. 4.4, it is clear that the reversal of core collapse coincides with a rapid turnaround in the halo’s $E/|E_0|$. In all three SIDM implementations, there is a decrease of $\sim 15\%$ of the total halo energy by the end of the simulation run.

While the energy loss driven by gravitational interactions is tied to adaptive force softening (as discussed in the next section), the energy gains driven by self interactions likely result from particles scattering multiple times in a single time step. Specifically, "bad events" constitute particle multi-scatters with neighbors that reside on other CPUs, which leads to energy gain since the scattering velocities are not updated between multi-scattering events

(see Ref. [173] for a detailed discussion). Generally the number of bad events is of the same order as the number of multi-scatters because most of the particle neighbors reside on different CPUs. A simple back-of-the-envelope estimate of the double-scattering rate shows these highly infrequent events can generate a significant change in energy even for well-resolved halos. The number of double-scattering events, $N^{(2)}$, in the halo's core is

$$N^{(2)} = N^{(1)}P_i \approx N^{(1)}\kappa, \quad (4.18)$$

where $N^{(1)}$ is the number of single-scattering events and P_i can be approximated as κ far into core collapse when the interactions are very frequent. Assuming each double-interaction event adds kinetic energy comparable to a core particle of mass m_p with velocity v_{core} , the relative change in a halo's kinetic energy is

$$\frac{\Delta E}{E_{0,\text{kin}}} \approx \frac{N^{(2)}m_p v_{\text{core}}^2}{M_{\text{halo}}v_{\text{core}}^2} \approx \frac{N^{(2)}}{N} \approx \kappa \frac{N^{(1)}}{N}, \quad (4.19)$$

where $E_{0,\text{kin}}$ is the halo's initial kinetic energy, and we approximate the average speed of a halo particle as being $\mathcal{O}(1)v_{\text{core}}$. Clearly, the gain in kinetic energy becomes appreciable as $N^{(2)}$ approaches the total number of particles in the halo, N . For the high-resolution simulations with $N = 10^6$ particles, approximately $N^{(2)} = 10^6$ double-scattering events are needed to change the halo's kinetic energy by $E_{0,\text{kin}}$. During the last ≈ 1 Gyr of the simulation concurrent with the rapid changes in the halo's energy, the high-resolution simulations with $\kappa = 0.02$ go through $N^{(1)} \approx \mathcal{O}(10^7)$ single-scattering events and $N^{(2)} \approx \mathcal{O}(10^5)$ double-scattering events. This results in an energy change of approximately

$$\frac{\Delta E}{E_{0,\text{kin}}} \approx 0.02 \times \frac{10^7}{10^6} \approx 0.1, \quad (4.20)$$

which is comparable to the energy change during this time of the simulation ($\approx 15\%E_0$). Since $\Delta E \propto \kappa$, reducing κ by an order-of-magnitude greatly improves energy conservation.

However, $\kappa = 0.002$ does not, in general, guarantee the absence of artificial heating. Instead, reducing κ allows the simulation to reach higher densities, where the energy error per double scattering event increases due to the rising temperature of the core.

Refs. [173, 56], implemented several features in their N-body codes to reduce the impact of bad multiple scattering events. In order to reduce the probability of bad scattering, Ref. [173] enforced a particle communication direction between every pair of the CPUs, while Ref. [56] additionally enforced a communication queue such that a single particle is only actively scattering on a single CPU at a time, which completely eliminates the possibility of simultaneous multi scattering. Not unlike simply lowering the scattering rates in individual particle time steps, this latter approach does come with a significant impact on computational efficiency of the simulation.

A key take-away is that without implementing a numerical scheme that reduces the rate of multi scattering, the time-stepping parameter, κ , must be chosen judiciously to minimize energy non-conservation. For a given κ , we find that the Spline method minimizes energy gain or loss compared to the other two methods for the halos simulated here. It is not clear why the Spline method exhibits smaller energy gains, but it could be due to the neighbor sorting when choosing which particle to scatter with, which is a major difference from the other two methods.

4.4.4 Adaptive Gravitational Force Softening

All analyses until this point have focused on simulations that were run using adaptive force softening for the gravitational interactions. Here, we explore the effects on the halo evolution by instead using a fixed force-softening length, ϵ , and different tolerance parameter, η . Because the goal is to maximize energy conservation, we focus on the Spline method in the following discussion. Figure 4.5 shows the results of re-simulating the low-concentration

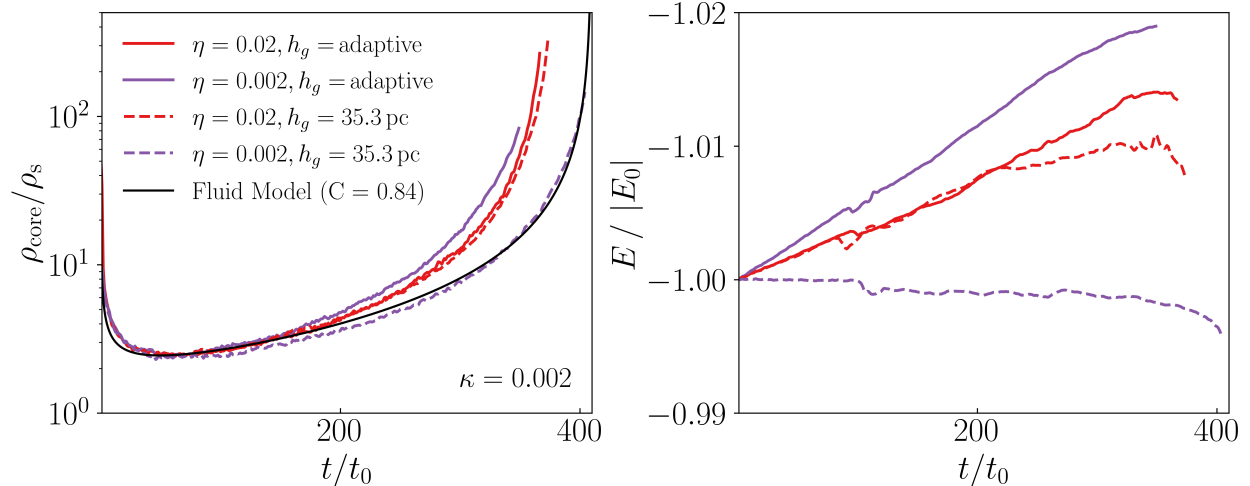


Figure 4.5: The evolution of core density and energy of the low-concentration halo with fixed and adaptive force softening for gravity, using the Spline implementation. The particle smoothing h_s is adaptive. Additionally, the tolerance parameter, η , is varied. The simulation with fixed force softening and $\eta = 0.002$ exhibits much improved energy conservation relative to the others. The black line corresponds to the best-fit fluid model solution with $C = 0.84$, obtained by fitting to the simulation with best energy conservation.

$\kappa = 0.002$ halo for the Spline method. The previously described adaptively-softened simulation is plotted in solid red for comparison. As shown in the right panel of Fig. 4.5, reducing η while using adaptive softening increases energy loss over the course of the simulation. However, the combination of fixing the force-softening length *and* decreasing the tolerance parameter to $\eta = 0.002$ essentially removes the numerical heating observed in all other simulations. By comparing the evolution of this simulation with the rest, it is clear that the gain of $E/|E_0| \sim 1\text{--}2\%$ results in roughly a 10% acceleration in core collapse. Because it is unpredictable how much of an effect numerical heating/cooling will have on core evolution in general, adaptive softening for gravity is undesirable for DM particles in core-collapsing simulations.

4.5 Comparison to the Fluid Model

The hydrodynamical evolution of SIDM halos is captured by the gravothermal fluid model, extensively explored in several key studies [128, 8, 104, 161, 51, 148, 155, 232, 234, 84, 242]. The set of partial differential equations describing the evolution of the local density $\rho(r, t)$ at location r and time t , velocity dispersion $v(r, t)$ and luminosity $L(r, t)$, are the fluid-momentum equation in the hydrostatic limit, the first law of thermodynamics, and a heat transport equation with an effective heat transport coefficient that is typically used in both the short and long mean-free-path regimes. The heat transport equation is given by

$$\frac{L}{4\pi r^2} = -\frac{3}{2}av\frac{\sigma}{m}\left(\frac{4\pi G}{C\rho v^2} + \frac{a}{b}\left(\frac{\sigma}{m}\right)^2\right)^{-1}\frac{\partial v^2}{\partial r}, \quad (4.21)$$

where $a = 4/\pi$ and $b = 25\sqrt{\pi}/32$. For almost all cases of interest, the entire halo initially evolves in the long mean-free-path regime during which the first term in parenthesis dominates. When the core density and velocity dispersion become large, the second term can begin to dominate and the core enters the short mean-free-path regime. Eq. (4.21) is an approximation because there is no *ab initio* derivation of heat transport in the long mean-free-path regime. In that regime, the parameter C has been used as a constant (in space and time) $\mathcal{O}(1)$ fudge-factor in an attempt to calibrate the conductivity using N-body simulations of isolated and idealized halos. Several studies have evaluated this constant and there exist discrepancies of order 25% between different studies with some finding values of $C \approx 0.6$ [155, 51] while others find larger values of $C \approx 0.75$ [104] and $C \approx 0.82$ [234]. The various derivations have used different simulation suites with most focused on either the Pippin halo run of Ref. [48] with various cross sections, or isolated halos run by Refs. [104] and [234]. Additionally, the various studies use different methods to fit the fluid model to these simulations. Given the findings of our study, it is plausible that at least some of these discrepancies arise from numerical variations between the simulations.

For completeness, we evaluate our own value of C by comparing the fluid solution of Ref. [155]’s run #1 to our high-concentration, high-resolution, $\kappa, \eta = 0.002$ simulation, with the Spline method and fixed gravitational softening (which exhibits good energy conservation). We choose the value of C for which the fluid method and simulation reach $\rho_{\text{core}} = 100\rho_s$ at the same time and find $C \approx 0.84$. The fluid result is shown by the solid black curve in the left panel of Fig. 4.5.

After setting C , one can then compare the entire simulated halo evolution to the variables that are solved for in the fluid approach. For example, the fluid model predicts that the core density reaches its minimal value at approximately $60t_0$ for an initial NFW halo in isolation. At that time, the core density is predicted to be $\rho_{\text{core}} \approx 2.4\rho_s$, the core radius is $r_{\text{core}} \approx 0.45r_s$, and the core velocity dispersion is $v_{\text{core}} \approx 0.64v_{\text{max}}$. As shown in Fig. 4.1, the results for both the low- and high-concentration simulations are consistent with the fluid predictions. In particular, the minimum core density in the high-resolution simulations⁵ is $\min(\rho_{\text{core}}) \approx (2.4\text{--}2.5)\rho_s$ and is reached around $t \approx 70t_0$, regardless of SIDM implementation. There is particularly good agreement in the central velocity dispersion with $v_{\text{core}} \approx (0.64\text{--}0.65)v_{\text{max}}$. There are no systematic differences in the core sizes between SIDM implementations, with $r_{\text{core}} \approx 0.42r_s$ for all resolutions simulated, as shown in Fig. A2.

4.6 Conclusions

This paper explores the uncertainties in modeling DM self interactions in N-body simulations, focusing on the regime where the core size is shrinking and the core density is increasing with time. As a concrete case study, we focused on a high- and low-concentration variant of a $1.15 \times 10^9 M_\odot$ halo. We assumed a constant cross section of $50 \text{ cm}^2/\text{g}$ and implemented

⁵Given a density profile at every snapshot, we fit a cubic polynomial to $\rho_{\text{core}}(t/t_0)$ in the time span $(50\text{--}200)t_0$ when core collapse is expected to be occurring. From this, we determine the density at maximum core, $\min(\rho_{\text{core}})/\rho_s$, by finding the minimum of the resulting curve. This procedure reduces numerical noise in determining these quantities, which can be significant depending on the resolution.

the self interactions using three common modeling methods found in the literature: the Spline, Kernel-Overlap, and Top-Hat techniques. Additionally, we also varied the number of particles, time-stepping criteria, and gravitational force softening used to simulate the halos. For the isolated dwarf halos considered in this work, we showed that:

- Clear differences arise in the halo evolution depending on the SIDM implementation. Halos evolved using the Spline method collapse fastest, followed by those evolved using the Kernel-Overlap and then the Top-Hat method. These differences result from the interplay of at least two effects. First is that the different SIDM implementations yield different scattering rates, which can be between $\sim 2\text{--}8\%$ larger than the expected theoretical value. Second is that the specific numerical implementation of gravitational and DM scattering can result in the halo’s total energy not being conserved. Small differences in the energy conservation can translate to large differences in the maximum core densities reached before evolution stalls. We find that the Spline method has the best energy conservation for the halos simulated.
- An inadequate choice of time step can result in core evolution that stalls or reverses entirely, reducing the observed density and dispersion profiles. Therefore, an appropriate choice of the time-stepping criterion is critical for minimizing the effects of energy non-conservation—e.g., one must ensure that the probability of DM self-scattering in a single time step is very small. For our simulated halos, we found that limiting this probability to 0.2% ($\kappa = 0.002$) was sufficient to prevent spurious cooling during a halo’s core collapse. This choice for κ is about an order-of-magnitude lower than the default values used in GIZMO ($\kappa = 0.2$) and Arepo ($\kappa = 0.02$).
- Numerical heating that arises from adaptive gravitational softening can accelerate the core-collapse process, even if it only results in a few-percent change in the halo’s total energy. We showed that using a fixed gravitational softening, along with an appropriate choice of tolerance parameter ($\eta = 0.002$), maximized the accuracy of energy

conservation for the case of the Spline method.

- The evolution of low-resolution halos with 3×10^4 particles is dominated by noise in the generation of initial conditions. In particular, stochastic noise in different realizations of identical $\sim 10^9 M_\odot$ NFW halos introduces a $\sim 30\%$ scatter in the core density and collapse time. This is a larger systematic uncertainty than the choice of SIDM method. The highest-resolution halos considered here, which have 10^6 particles, are more robust to changes in the initial conditions, but still lead to 10% level uncertainties in collapse time. This highlights that a certain level of uncertainty persists across our simulations even after attempting to optimize the SIDM implementation.

This work underscores the challenges encountered when simulating the SIDM gravothermal collapse process and comparing results across the literature that may start from different sets of simulation parameters, initial conditions and methods. While we have only focused on an isolated $\sim 10^9 M_\odot$ halo here as a concrete example, the results already demonstrate that the detailed implementation of the gravitational and self interactions can significantly alter a halo's evolution into the core-collapse regime. These results motivate further convergence studies for an expanded range of halo masses and should also be generalized to a cosmological setting. Such work will help minimize numerical mis-modeling effects and ensure that spurious energy gains or losses in SIDM simulations are not misattributed to genuine physical effects.

Chapter 5

Breakdown of approximate universality in the evolution of SIDM halos

5.1 Abstract

Self-interacting dark matter (SIDM) models offer a promising solution to several small-scale problems in cosmology, providing a compelling mechanism to resolve these issues by altering the structure of dark matter halos. This study explores the gravothermal evolution of isolated SIDM halos under a variety of self-interacting cross sections, including both monotonic and resonant velocity-dependent scattering models. We present simulations that demonstrate how these interactions impact the core formation and collapse in dark matter halos. Our results reveal that velocity-dependent cross sections generally match the previously proposed universal evolution models up to a factor of order unity, and present a parametric fit for more accurate predictions. This work provides a deeper understanding of SIDM and its

implications for galaxy formation and evolution.

5.2 Introduction

Dark matter (DM) self interactions provide the means to transfer heat and mass across a halo [198]. When the self interactions are strong enough, they can impact the structure, morphology and diversity of galaxies and their satellites—see Refs. [206, 3] for reviews. Self-interacting Dark Matter, can reshape the DM halos by thermalizing the DM in the central regions of the halos, forming a core of constant density and, given enough time, it can lead to the gravothermal collapse in which the core grows exponentially in density eventually collapsing into a black hole [128, 9, 104, 148, 155, 61]. This mechanism for black hole formation can produce seeds for super-massive black holes (SMBH) in the early universe, $z \geq 6$, which are unlikely to form so early in Λ CDM cosmology [161]. While the core collapse progresses within the long-mean-free-path (LMFP) regime—a scenario in which the DM particle interactions are infrequent and the particles can make full orbits around the halo without scattering—the core sheds mass rapidly as its temperature/density increases. However, eventually the core will enter and short-mean-free-path (SMFP) regime in which the interactions become frequent enough to inhibit the heat and mass transport in and out of the core. From this point onward it is possible to extrapolate from the moment of transition from the LMFP to the SMFP to predict the mass of the final black hole [148, 61].

DM core collapse could explain several discrepancies between observed properties of MW satellite galaxies and cosmological simulations assuming Λ CDM cosmology [206]. However, SIDM models that disfavor core collapse in MW satellite galaxies have been cannot fully explain these discrepancies and have been largely ruled out [166, 211, 32, 99, 195, 197]. Several studies have shown that the interaction has to be velocity-dependant to match the full diversity and structure of galaxies at various mass scales with the cross section of the order

$0.1 - 2 \text{ cm}^2/\text{g}$ at the host galaxy scales [90, 169, 94, 4] and as high as $50 - 100 \text{ cm}^2/\text{g}$ [195, 32] at the scales of dwarf galaxies.

From the perspective of particle physics, it's natural to expect a velocity-dependent cross sections and many previous studies have considered a Yukawa cross section, analogues to Rutherford scattering. Although, a wide range of possible DM interactions exhibit a "resonance" cross section, where scattering is enhanced at some characteristic relative velocity [28]. While we don't understand the dominant DM scattering mechanism, it is possible to identify universalities in DM halo evolution across a variety of velocity-dependent cross sections [231, 155, 61]. This can greatly simplify the process of eliminating DM scattering mechanisms without the need to simulate the entire range of model parameters. A universality has been identified for monotonically decreasing cross-sections using semi-analytical methods [155, 229, 234] and using N-body simulations [231]. These studies showed that the evolution under velocity-dependent cross sections can be mapped to a constant cross section by velocity-averaging of the heat conductivity at the "maximum core"—a point in halo evolution where the core reaches maximum size—, which is predicted to be universal in first order solutions to the fluid equations [155, 234]. The aforementioned universality has not been thoroughly tested in N-body simulations. Ref. [231] have focused on nearly completely velocity dependent cross sections with $\omega \ll v_{\text{max}}$.

Additionally, it remains unclear whether this or another universality applies to "resonant" interactions, the influence of which have not been thoroughly explored in N-body simulations. Resonance cross sections have been first introduced and extensively studied in the context of DM annihilation and its consequences for DM relic density an cosmic ray excess [70, 68, 88, 52, 163, 82, 130, 53, 71], but its consequences for galaxy dynamics and morphology have not been explored in detail. Recently Ref. [62] have investigated the implications of resonant cross sections on the structure of dark matter halos and found that the halo's central density was lower relative to the universal prediction. However, the full parameter of cross

sections have not been explored thoroughly explored to date. In this paper, we explore the halo evolution under a wide range of possible Yukawa-like and resonant cross sections, and propose an parametric fit for a general mapping method for any velocity-dependent cross section.

This paper is organized as follows, in Section 5.3 we discuss the differential cross sections we employ in the simulations as well as the previously established mapping methods from differential cross section to a constant "effective" cross section. Section 5.4 describes the halos simulated and specific cross sections employed in the simulations. In section 5.6 we describe the halo evolution produced by a variety of differential cross sections and provide a parametric prescription for predicting core properties at any time that is simply a function of the velocity-averaged cross section and the halo's NFW parameters. We summarize our findings in section 5.7.

5.3 Differential Cross Sections

In this section we discuss the Yukawa and resonant SIDM models and we describe velocity-averaging methods of the cross sections.

5.3.1 Yukawa Scattering

The Yukawa interaction describes the majority of coupling in the electro-weak theory and the fermion coupling to the Higgs field. Its ubiquity in the standard model of physics makes the Yukawa interaction a natural first choice for exploring the dark sector of physics and this option has been explored extensively in many SIDM studies (e.g. [82, 112, 10, 145, 234, 232, 230]).

In the non-relativistic limit, the Yukawa interaction governs the scattering between two particles in indistinguishable states. It is mediated by a light scalar ϕ , or vector ϕ_μ particle, with the interaction Lagrangian of the form:

$$\mathcal{L}_{\text{int}} = \begin{cases} g_\chi \chi \chi \phi \\ g_\chi \chi \gamma^\mu \chi \phi_\mu. \end{cases} \quad (5.1)$$

for both of these scenarios [207]. Here, we briefly describe the cross section and direct the reader to [67] for comprehensive cross section calculations. The total center-of-mass cross section includes the contributions from the t-, u- and -tu channels

$$\sigma = \sigma^{(t)} + \sigma^{(u)} + \sigma^{(tu)}, \quad (5.2)$$

where the u- and t-channel contribute equally to the cross section

$$\sigma^{(t)} = \sigma^{(u)} = \frac{2\pi\sigma_0}{1 + (v/\omega)^2}, \quad (5.3)$$

and

$$\sigma^{(tu)} = 4\pi\sigma_0 \frac{\ln(1 + (v/\omega)^2)}{(v/\omega)^2(2 + (v/\omega)^2)}, \quad (5.4)$$

Here, we only consider the t-channel scattering, which corresponds to the Rutherford-analogous differential cross section:

$$\frac{d\sigma^{(t)}}{d\Omega} = \frac{d\sigma^{(u)}}{d\Omega} = \frac{\sigma_0}{2 [1 + (v/\omega)^2 \sin^2 \frac{\theta}{2}]}. \quad (5.5)$$

The inclusion of the tu-channel has minimal effect on the velocity dependence of the total cross section and we neglect it here for simplicity [67].

Additional complication arises due to the fact that Rutherford scattering is dominated by forward scattering, which leaves the halo largely unchanged for indistinguishable particles. For this reason the momentum transfer, or viscosity cross sections have been proposed as the more useful quantities for parameterization of heat transfer [53, 208, 173, 155, 232]. Additionally, from the perspective of N-body simulations, applying such cross sections directly can reduce the computational cost of simulations several times over [173]. The viscosity cross section has been shown to reproduce the halo evolution under the full differential cross section with high accuracy [229]. It is defined as

$$\sigma_{\text{visc}} = 3/2 \int d\Omega \sin^2(\theta) \frac{d\sigma}{d\Omega} \quad (5.6)$$

For the Yukawa scattering, this integral results in

$$\sigma_{\text{visc}} = \frac{8\sigma_0\omega^6}{v^6} \left[\left(2 + \frac{v^2}{\omega^2} \right) \ln \left(1 + \frac{v^2}{\omega^2} \right) - 2\frac{v^2}{\omega^2} \right]. \quad (5.7)$$

We run several simulations with a Yukawa viscosity cross section to simulate scenarios in the cross section is strongly dominated at low relative velocities. Additionally, we simulate resonant cross sections, some of which are only weakly resonating, and similar to the Yukawa cross section. We describe the resonance cross sections in the following section.

5.3.2 Resonant Scattering

Resonant interactions are characterized by a peak in the cross section that is produced by an absorption of the scattering particles into a bound, or quasi-bound state. The half-life of this state is related to the width of the resonance and is practically instantaneous compared to the timescales of galactic evolution. Resonant DM is a product of charged fermionic, or hadronic DM particles interacting with their anti-particles. For example, for fermionic matter, a resonance can be achieved through an interaction mediated by a scalar particle

analogous to the Yukawa scattering described above [28]. The σ or ρ meson resonances in QCD-like DM are another possibility [28]. For low-energy, elastic scattering, such resonant interactions can be approximated with the Breit-Wigner distribution:

$$\sigma_{\text{visc}} = \sigma_0 + \frac{\sigma_1 (v/w)^{4L}}{(1 + (v/w)^2)^2 + g(v/w)^{4L+2}}, \quad (5.8)$$

where σ_0, σ_1 are normalization constants, g is the unitless resonance width factor, w is a characteristic velocity and L is the angular momentum of the bound state [28, 29]. For $L = 0$, the S-wave scattering, $\sigma_v(0) \rightarrow \sigma_0 + \sigma_1$, while for $L = 1$, the P-wave scattering, $\sigma_v(0) \rightarrow \sigma_0$, i.e. the resonance term vanishes at low velocities. In this paper, we focus on the S-wave scattering with $\sigma_0 = 0$, but include a few examples of non-vanishing, P-wave cross sections with a constant term for completeness.

For S-wave scattering, the cross section peaks at

$$v_{\text{peak}} = \omega \sqrt{1 - g/2}. \quad (5.9)$$

The P-wave analogous expression is much more complicated, however the above expression is sufficiently accurate for strongly resonant, $g \ll 1$, P-wave cross sections, like the ones considered here (accurate within 5%).

Such scattering is also intrinsically isotropic in the center-of-mass (CM) frame since the post decay directions of the particles is agnostic to the initial relative momenta of the particles. Hence, $\sigma_v = \sigma$ up to a constant factor.

5.3.3 Velocity Averaging Methods

A simple approach to predicting the evolution of DM halos whose particles interact with a velocity-dependent cross section is to average the cross section over the halo's core velocity

distribution to produce an effective, velocity-independent cross section, σ_{eff} which would produce an equivalent halo evolution [155, 232, 61, 234]. Motivated by thermal conductivity in the kinetic theory of gases, we focus on velocity averaging of the form

$$\langle \kappa \rangle^{-1} \propto K_n(\sigma_v(v_{\text{rel}})) = \frac{\langle v_{\text{rel}}^n \sigma(v_{\text{rel}}) \rangle}{\langle v_{\text{rel}}^n \rangle}, \quad (5.10)$$

where $\langle \cdot \rangle$ symbolises the thermal average over the Maxwell-Boltzmann (MB) distribution with the 1D velocity radial dispersion,

$$\langle f(\mathbf{v}_{\text{rel}}) \rangle = \int_0^\infty \frac{1}{(2\pi v_r^2)^{3/2}} e^{-\frac{(\mathbf{v}_{\text{rel}}/v_r)^2}{2}} \cdot f(\mathbf{v}_{\text{rel}}), \quad (5.11)$$

and n is an arbitrary number. For cross sections monotonically decreasing with v_{rel} , $n = 5$ has been shown a good fit to N-body simulations [231, 229]. This value is also well motivated by first order approximation to the heat transfer in kinetic theory, where to first order the heat conductivity of gases in the SMFP regime is proportional to [155, 61]

$$\kappa_{\text{SMFP}} \propto \frac{1}{K_5}. \quad (5.12)$$

Expanding the fluid solution to the second order the heat conductivity is proportional to

$$\kappa_{\text{SMFP}}^{(2)} \propto \frac{1}{K_{\text{eff}}^{(2)}} = \left(\frac{77K_5 - 112K_7 + 80K_9}{28(K_5)^2 + 80K_5K_9 - 64(K_7)^2} \right)^{-1} \quad (5.13)$$

While this calculation can be carried out analytically for gases in the SMFP, this is generally not the case in the LMFP. However, some motivation exists for $\kappa_{\text{LMFP}} \propto K_3$ as it has been shown that energy transfer for collisions governed by Yukawa scattering result in heat transfer proportional to $\langle \sigma_{\text{visc}} v^3 \rangle$ [31].

Surprisingly, it is the SMFP solution (first order) that has been found to match to N-body simulations in terms of halo core collapse, but with moderate differences in core density

over most of the halo evolution. Halos simulated with velocity dependent cross section had smaller core densities than their constant cross section counterparts [231]. Similar differences have not been predicted by the semi-analytic fluid model, which predicts a universal halo evolution with characteristic "maximum core" density $\rho_{\min} \approx 2.4\rho_s$, radius $r_{\min} \approx 0.45r_s$, and velocity dispersion is $v_{\min} \approx 0.64v_{\max}$ [155]. Another universality predicted by fluid model is the core collapse time $t_{\text{coll}} \approx 330t_{c,0}$, where $t_{c,0}$ is a timescale normalized to halo's physical properties at the maximum core stage [155, 61]

$$t_{c,0} = \frac{2}{3aC}(\rho_{\min}v_{\min}K_n(\sigma(v_{\text{rel}}))^{-1}. \quad (5.14)$$

Here C is a dimensionless free parameter of order unity, which we take to be $C = 0.82$ based on simulation from Ref. [156]. Due to the strong self-similarity in the "maximum core" phase of halo evolution, the v_{core} has been previously used for the 1D velocity dispersion in the the aforementioned mapping. Given the results of Ref. [231], it is possible this self-similarity does not hold in general for velocity dependent cross sections and this mapping method may need to be revised. Additionally, it remains unclear whether this general mapping will hold for cross sections that are a non-monotonic function of v_{rel} , such as the resonance interactions we focus on here.

5.4 Simulations

We run the simulations employing the gravity-tree solver in GIZMO [78]. Although we have modified the SIDM module in GIZMO with the aim of improving energy conservation in halos with strong self-interactions [156]. These changes include a more conservative timestepping criteria and a smoothed-particle-hydrodynamical (SPH) scattering algorithm originally applied to SIDM in the Arepo code [214]. In addition to the changes described in Ref. [156], we have incorporated the velocity dependent cross sections, which follow Eq. (5.7)

and Eq. (5.8) and appropriate time stepping criteria (See appendix 5.5) for details and code verification test.

Most of the simulations consider an isolated halo of mass $M_{200} = 1.15 \times 10^9 M_\odot$ and concentration $c_{200} = 19$, but we also reproduce the BM2 halo simulated by [232] to verify our code and to test the robustness of our results to halo parameters. This halo has smaller mass $M_{200} = 2.32 \times 10^7 M_\odot$ and lower concentration $c_{200} = 7.6$ (at $z = 0$). These initial conditions are created using `Spheric` [63], which generates spherically symmetric NFW halos with characteristic radius r_s and density ρ_s . Halos are exponentially truncated at radius r_{cutoff} . We refer the reader to Table 1 for full halo details.

For our primary halo (#1) we run a set of 14 simulations with different velocity-dependent SIDM cross sections, which span a range of $v_{\text{peak}} = 0.1 - 3.0 v_{\text{max}}$ and two such cross section (one Yukawa and one resonant) are simulated for halo #2. Following the proposed velocity-averaging methods of Refs. [232, 230], we normalize all cross section such that $K_5 = 16.5 \text{ cm}^2/\text{g}$ and we compare the results to a simulation run with such constant cross section. Additionally, to keep all simulations firmly in the long-mean-free-path (LMFP) regime, we ensure $\sigma_v(v_{\text{rel}})$ does not exceed $50 \text{ cm}^2/\text{g}$ at $v_{\text{rel}} > v_{\text{max}}$. This ensures that high velocity energy DM particles, which are responsible for the majority of the heat transfer in the halo remain in the LMFP. The cross section are plotted in Figure 5.3. Note that most of the resonance cross sections peak well above v_{max} .

We color code the cross sections in two groups, one that encompasses cross sections that are weakly resonating or exhibit no resonance, while the second group is composed of strongly resonating cross sections (with $g \ll 1$). The former have the results plotted in shades of blue, while the resonance dominant cross sections are plotted in shades of red. See table 5.1 for cross section parameters. Colors scale linearly with v_{peak} determined by eq. (5.9) so that cross sections with scattering more dominant at higher relative velocities are plotted in darker shades.

For each simulation the core density and core size are determined by fitting a cored profile to each simulation's snapshot. The central velocity dispersion is then calculated from the core particles' radial velocity. See Ref.[156] for the full description of this fitting method.

Halo #	c_{200}	M_{200} [M_{\odot}]	r_{200} [kpc]	r_s [kpc]	ρ_s [M_{\odot}/kpc^3]	v_{max} [km/s]	r_{cutoff} [kpc]
1	18.7	1.15×10^9	22.1	1.18	2.73×10^7	21	23.6
2	7.6	2.32×10^7	1.07	0.141	2.73×10^8	8	2.77

Table 5.1: Halo parameters

















Case	σ_1 cm ² /g	σ_0 cm ² /g	w km/s	g/L	Color	Case	σ_1 cm ² /g	σ_0 cm ² /g	w km/s	g/L	Color
C0	18243.5	0	1	–		R1	9.4	5.5	20	0.05/1	
C1	4839	0	5	–		R2	2.515	0	45	0.05/0	
C2	1804	0	7	–		R3	1.305	0	53	0.025/0	
C3	642	0	10	–		R4	1.529	6.14	55	0.06/1	
C4	233.9	0	20	0.66/0		R5	1.302	0	57.5	0.025/0	
C5	28.7	0	45	1.33/0		R6	1.344	0	60	0.025/0	
C6	16.5	0	70.1	–		R7	2.161	0	70	0.04/0	
C7	16.5	0	∞	–		R8	4.405	0	80	0.08/0	

Table 5.2: Cross section parameters.

5.5 Simulation Convergence

We test our implementation of the velocity dependent against the results of the BM2 halo in Ref. [232]. This simulation is listed as C0 in Table 5.4 with cross section parameters $\sigma_1 = 18243.5$ and $w = 1$. The result of our simulation together with the results from Ref. [232] are plotted together in the left panel of Figure 5.2 and agree with some deviations in the maximum core phase, which is expected as we reproduce the initial conditions from

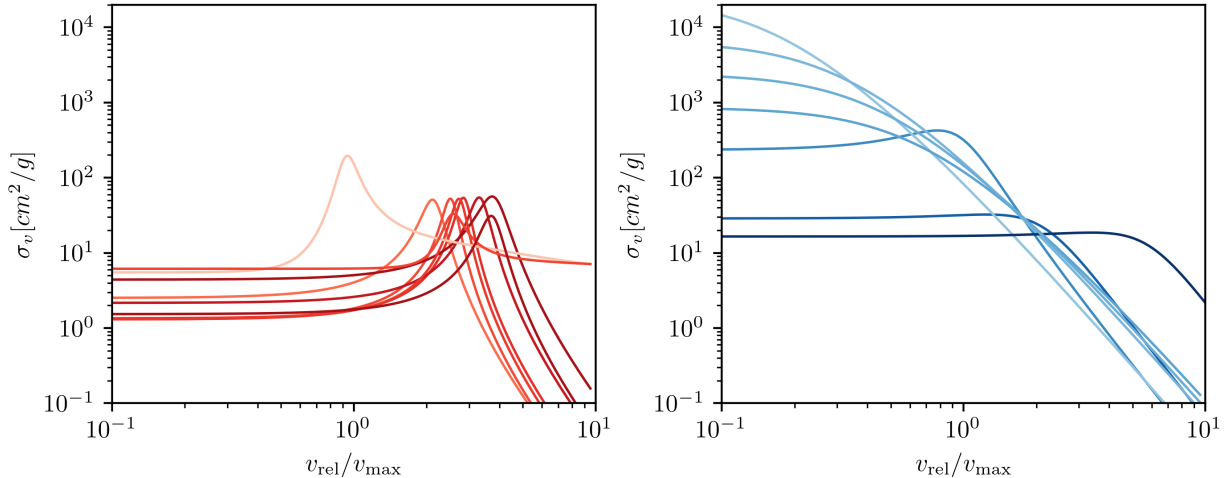


Figure 5.1: The viscosity cross sections used in the simulations plotted as a function of relative velocity. For narrative purposes, the cross section are divided into two groups, the non-resonance and resonance-dominant. The former is composed of Yukawa cross sections together with two weakly resonating cross sections (i.e. $g \simeq 1$). Following the results from Refs. [229, 234] all cross section are normalised such that $K_5 = 16.5\text{cm}^2/\text{g}$ and should produce similar halo evolution for a given halo.

Ref. [232] with different random seeds. At this resolution level stochastic noise in different realizations of identical initial conditions can affect the subsequent halo evolution at a 10% level.

Following the results from Ref. [156] we run all simulations with timestepping criteria that severely limit the probability of scattering in a given particle time step. There are two timestepping criteria to consider. First, there is limit to how far a particle can move in a time step following a gravitational scattering:

$$dt_i = \sqrt{\frac{2\eta h_{g,i}}{a}}, \quad (5.15)$$

where $h_{g,i}$ is the gravitational force softening, a is the gravitational acceleration a particle experienced in the current timestep and η is an accuracy parameter describing the fraction

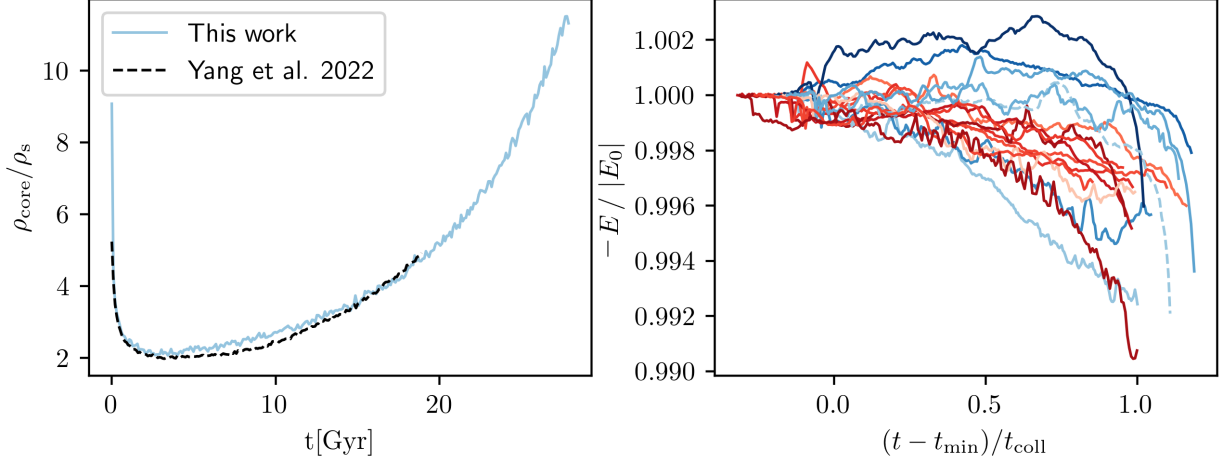


Figure 5.2: **Left:** The evolution of the core density for halo #2 and with interaction cross section $C0$, which is equivalent to halo BM2 from Ref. [232]. **Right:** The evolution of halo’s total energy for all simulations listed in Table 5.1. We ensure that all simulations experience less than 1% deviations in halo’s energy to limit the artificial cooling in the halo’s core that occurs due to ”bad” scattering events [173, 156].

of the force-softening length that the particle is allowed to move in the following time step.

The second timestepping criteria relates directly to the self-interactions of the DM:

$$\sigma \rho_{\text{loc}} v_{\text{loc}} dt_i < \kappa, \quad (5.16)$$

where ρ_{loc} is the local DM density, v_{loc} is the local velocity dispersion and dt_i is the current timestep for a particle i . The parameter κ is effectively the maximum probability of scattering between a pair of particles in timestep dt_i and the timesteps are adjusted to keep this probability smaller than κ .

For all simulations run here we pick $\kappa = \eta = 0.002$ to maintain energy conservation with 1% over the course of the simulation. The right panel of figure 5.2 plot the energy evolution for all our simulations. Given this setup, the energy of the halo begins to deviate far into core collapse, but too late and with too small of an effect to have any significant impact on the

our results.

5.6 Halo Evolution Under Differential Scattering

Figure 4.1 plots the evolution of core density vs time for halo #1 for all the cross sections described in Table 1. Shown in blue are cross sections with weak or no resonance, and in red are the simulations with resonance-dominant cross sections. Additionally, plotted in dashed blue are the results for the constant effective cross section, σ_{eff} . Following the results of Ref. [232], we expect all of these to produce halo evolutions similar to the effective cross section, and we find significant agreement for vastly different cross sections with core collapse times in agreement up to a factor of ~ 2 . However, there are systematic differences in both the core density and time of maximum core, where the core reaches minimum density, ρ_{min} , t_{min} , and the core collapse time, t_{coll} . Resonant cross sections that peak above v_{max} produce higher density cores and core collapse sooner than the halo subjected to the constant σ_{eff} . Conversely, low-velocity-dominant cross sections form lower density cores and collapse much later than expected from σ_{eff} . The two most slowly evolving halos correspond to the Yukawa cross sections with $w = 0.24, 0.33 v_{\text{max}}$. These cross sections produce halo evolution that is as much as half the rate of the effective cross section.

A simple rescaling of time by $t/t_{c,0}$ using the timescale from Ref. [155], which normalizes the halo evolution by the maximum core properties does not improve the fit between velocity-dependent cross sections and their σ_{eff} . One could attribute these differences to the fact that for strongly velocity-dependent cross sections at least a portion of the core particles exist in the SMFP regime over most of the halo evolution. While this is true for the Yukawa-like cross sections with $\sigma(v_{\text{rel}}) > 10^3 \text{ cm}^2/\text{g}$ at low velocities, low-velocity particles are few in number and collectively do not contribute much to the halo's heat transfer and therefore have minimal impact on halo evolution. A comparison between the most extreme cross

sections reveals this to be the case. The five Yukawa cross sections with $\sigma_1 > 200 \text{ cm}^2/g$ all produce halo evolution similar to one another and all evolve at a somewhat faster pace than the two Yukawa cross sections with $\sigma_1 < 20 \text{ cm}^2/g$. This indicates that the interactions that dominate heat transfer in the center of the halo are the ones with $v_{\text{rel}} > v_{\text{max}}$, where all the Yukawa cross sections are similar in magnitude. This is expected given that the heat transfer scales with K_p which is dominated by these high velocity interactions for as long as $p > 1$. This can be formally shown by calculating the core heat conductivity, as we do in Sec. 5.6.4, where we find that all of these cross sections evolve firmly in the LMFP regime until far into the core collapse regime despite very large cross sections at low relative velocities.

While σ_{eff} averaging produces a good first order estimate for the evolution of halo's central density from core expansion to core collapse, the apparent systematic differences in the maximum core density points to the limits of the first order analytic predictions. In the following sections, we generate a parametric fit to capture the systematic deviations of both the maximum core properties and core collapse time, t_{coll} from the analytic prediction. We build upon this to parameterize the entire halo evolution.

5.6.1 Predicting Core Formation

We chose to parameterize halo evolution in terms of the unit-less variable K_{p-2}/K_p . Figure 5.4 shows the core density at maximum core plotted against various velocity-averaged cross sections, ranging from K_1 to K_{eff} and all the powers of v_{rel} in between. Clearly, low powers of v_{rel} hold more information about the core density at maximum core and ρ_{min} correlates most strongly with K_1/K_3 , or K_3/K_5 . For these averages the maximum core density is largely constant for $K_{p-2}/K_p > 1$, but begins to rise rapidly for $K_{p-2}/K_p < 1$, especially for K_1/K_3 . We chose to parameterize the halo evolution by K_3/K_5 as it provides a smoother correlation than K_1/K_3 . The correlation between maximum core properties and K_1/K_3 be-

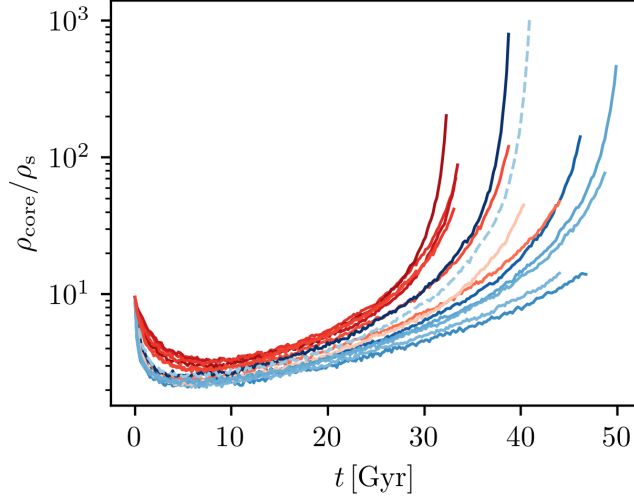


Figure 5.3: The evolution of core density for halo #1 under the viscosity cross sections described in Table 1. Plotted in dashed line is the evolution under a constant, effective cross section $\sigma_{\text{eff}} = 16.5 \text{ cm}^2/\text{g}$ calculated using the method from Ref. [229]. Generally, the resonating cross sections (plotted in shades of red) tend result in faster halo evolution than σ_{eff} , while the Yukawa cross section evolve more slowly. Yukawa cross sections with $w \ll v_{\text{max}}$ deviate the most from the evolution expected from σ_{eff} .

comes very steep at $K_1/K_3 < 1$, which can reduce predictive accuracy of the parametric fit. The same is true for the correlation of t_{min} , and t_{coll} . A similar exercise of plotting against non-consecutive powers of v_{rel} e.g K_1/K_7 , leads to far poorer correlation and we do not include these results here.

The resulting fits parameterised by K_3/K_5 for both ρ_{min} and t_{min} are shown in Figure 5.5. We normalize the maximum core density by ρ_s and maximum core time by $t_{c,0}$ defined in equation Eq. 5.14. For both, we chose to fit an exponential function to capture the strong scaling of both quantities at $K_3/K_5 < 1$. Although this choice is not special or motivated by theory, this function does exhibit the desired behavior at both large and small limits of K_3/K_5 . Here, the results for halo #2 are included and plotted as the crosses with the coding scheme outlined in Table 5.1. The resulting t_{min} and ρ_{min} lie on the same curve for both

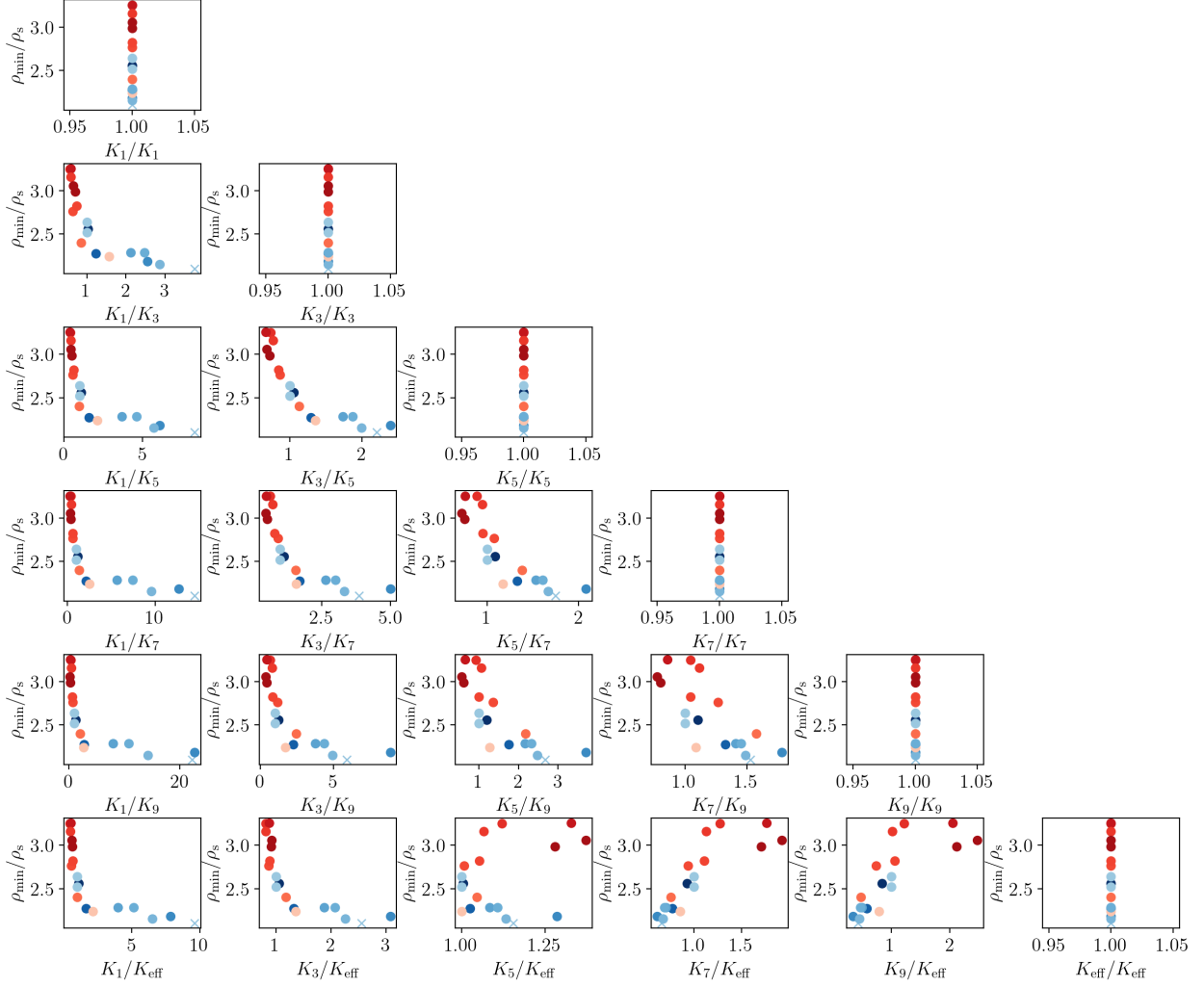


Figure 5.4: Core density at maximum core plotted against various velocity averaged cross section. Generally, ρ_{\min} is more correlated lower powers of v_{rel} . We choose K_3/K_5 as the single variable to parameterize the halo.

halos. The parametric equations for the maximum core phase are:

$$\begin{aligned} \rho_{\min}/\rho_s &= 6.51e^{-2.72K_3/K_5} + 2.15 \\ t_{\min}/t_{c,0} &= 358e^{-3.44K_3/K_5} + 36.5 \end{aligned} \tag{5.17}$$

The core 1D velocity dispersion at maximum core follows the fluid prediction for all cross sections with $v_{\text{core}} \approx 0.64v_{\text{max}}$ (see appendix B fig). However the core size generally varies linearly with core density at this stage of halo evolution. Figure 5.6 shows the linear correlation

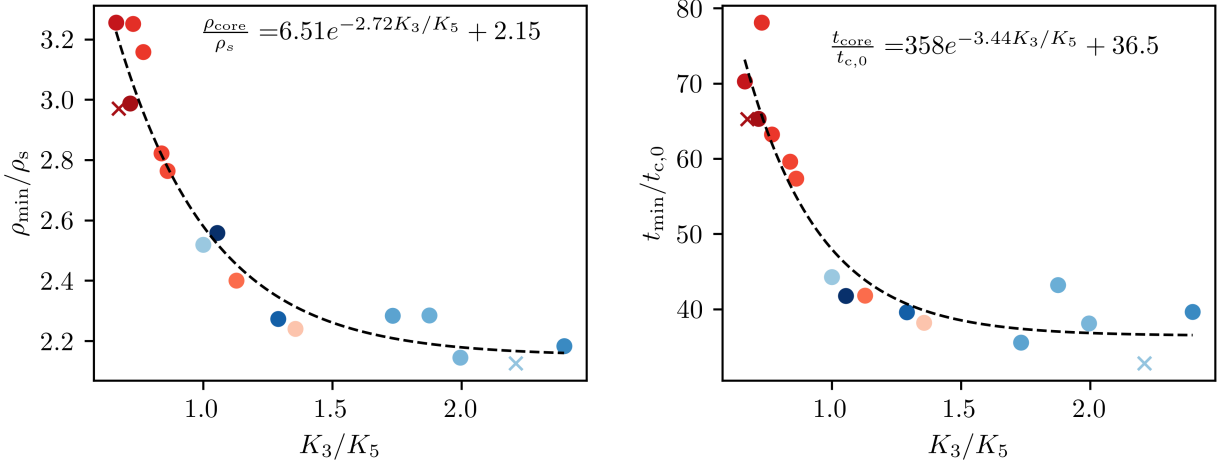


Figure 5.5: Core density and time at maximum core plotted against the ratio of the velocity-averaged, K_3/K_5 , cross sections. The resulting fits to an exponential function are shown. Both the density and time at the maximum core exhibit rapid changes for $K_3/K_5 \leq 1$, but approach a constant at large K_3/K_5 .

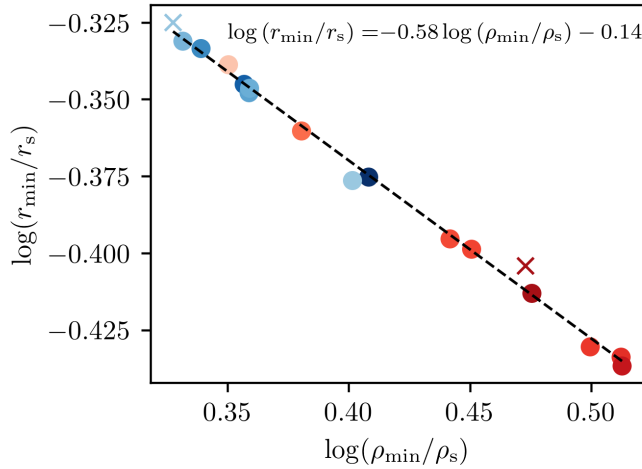


Figure 5.6: Core size vs. core density at the maximum core stage. Each point corresponds to a simulation with a different cross section color coded as described in Table. 5.1. The dots are simulations of halo #1 and crosses are simulations of halo #2. The red points are simulations with resonant cross sections and these tend to evolve faster with smaller and higher density cores at the maximum core stage. Conversely, the blue points are non-resonating cross sections which evolve more slowly producing larger and lower density cores once the core is fully formalised.

with decreasing core size as core density increases. This relationship is fit to

$$\log(r_{\min}/r_s) = -0.58 \log(\rho_{\min}/\rho_s) - 0.14, \quad (5.18)$$

and consequently the core mass at maximum core is

$$\log(M_{\min}/M_s) = 1.28 \log(r_{\min}/r_s) + 0.39, \quad (5.19)$$

where $M_s = \rho_s r_s^3$. Armed with a prediction for the maximum core phase, next we derive a core collapse timescale.

5.6.2 Predicting Core Collapse Time

In this section a parametric fit for the collapse time t_{coll} is derived. Although another approach is to adapt a maximum core relaxation timescale [9, 161, 234]

$$t_{r,0} = \frac{150}{C} \left(\sigma_{\text{eff}} \rho_{\min} r_{\min} \sqrt{4\pi G \rho_{\min}} \right)^{-1}, \quad (5.20)$$

which produces a fit of similar predictive power once the variations in ρ_{\min} and r_{\min} are accounted for, we continue with the parametric fitting as it is algebraically simpler.

We define the core collapse time as the time when the core density reaches $10\rho_s$. Figure 5.7 shows the ratio of core collapse time to maximum core time as a function of the velocity-averaged cross section variable K_3/K_5 . The resulting exponential fit is

$$t_{\text{coll}}/t_{\min} = 13.5(1 - e^{-1.90K_3/K_5}) - 6.51 \quad (5.21)$$

and shows that for cross sections dominant at velocities $v_{\text{rel}} > v_{\text{max}}$ the time from maximum core to core collapse is only about half as much relative to cross sections where scattering

is dominant at low velocities. Applying the above parametric equations 5.17 to the core evolution for all our simulations produces a universal halo evolution as shown in Figure 5.8, with a unprecedented match at the maximum core phase and subsequent halo evolution for all cross sections. Figure 5.10 shows the halo density profiles at equivalent points in halo evolution (at equivalent \tilde{t}) for the constant cross section, C7, and resonant R8 which peaks at $v_{\text{rel}} \approx 3v_{\text{max}}$. At the three chosen points in the halo evolution the outer density profile matches well between the two cross sections with the exception of $\tilde{t} = 1.3$, where small deviations between the two can be seen around $r_{\text{core}}/r_s = 0.5$. This is due to the fact that for the same initial conditions, the resonant cross section enters the SMFP regime at smaller core densities than the constant cross section, which makes the outer density profile steeper than in the LMFP regime [9, 104, 155, 61]. Additionally, there are small differences in core density/size, of about 20%, that arise from the variations in core properties once the core temperature reaches $v_{\text{core}} \approx 0.64v_{\text{max}}$ at the maximum core phase.

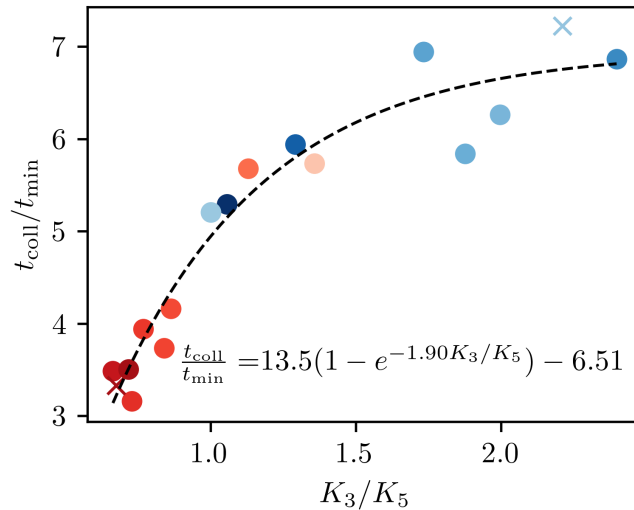


Figure 5.7: Core collapse time as a ratio to the maximum core time versus K_3/K_5 , the velocity-averaged cross sections. The resulting exponential fit is shown. t_{coll} serves as a normalization timescale that produces universal halo evolution for any self-interaction cross section.

With some understanding of the temporal evolution of SIDM halos across different cross sections, next we show that the core properties at any point in time follow the same power

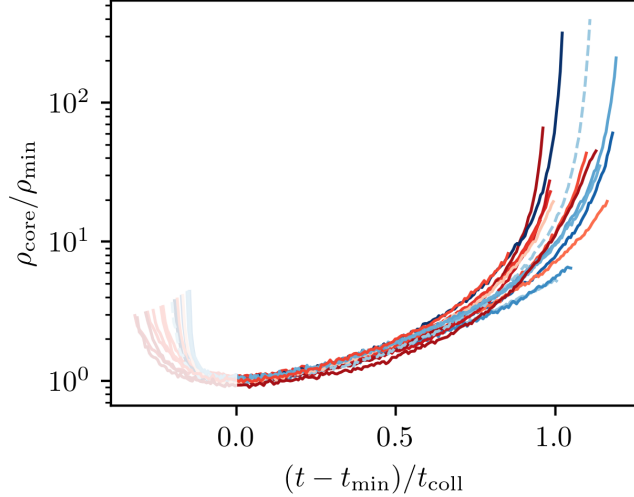


Figure 5.8: Halo evolution normalised by the collapse timescale t_{coll} and maximum core properties ρ_{min} , t_{min} for all simulated cross section for halo #1. The resulting increases the agreement with the effective cross section σ_{eff} and removes any systematic deviations from universality due to differences in the cross sections.

laws. This allows us to fully predict core properties at any time with a few simple equations.

5.6.3 Evolution of Core Properties

In this section we focus on predicting core properties throughout the halo evolution. The solution to gravothermal equations predicts a simple power law between central parameters, ρ_{core} , r_{core} and v_{core} [9, 155]

$$\frac{r_{core}}{r_s} = \left(\frac{r_{min}}{r_s} \right) \frac{\rho_{core}^{-\frac{1}{\alpha}}}{\rho_{min}}, \quad \frac{v_{core}^2}{v_{min}^2} = \left(\frac{v_{min}}{v_{max}} \right)^2 \frac{r_{core}^{2-\alpha}}{r_{min}}, \quad \frac{M_{core}}{M_s} = \left(\frac{M_{min}}{M_s} \right) \frac{r_{core}^{3-\alpha}}{r_{min}}, \quad (5.22)$$

where the choice of normalization constants is arbitrary, but due to the differences in these quantities at maximum core, it is convenient to normalize the LHS by the respective NFW parameters, while the RHS is normalised by the maximum core properties. Since the terms in the parentheses (the maximum core properties) are already constrained by the equations above, a prediction for core properties at any subsequent time is easily produced by combining

these relations, given that α is generally independent of the cross section.

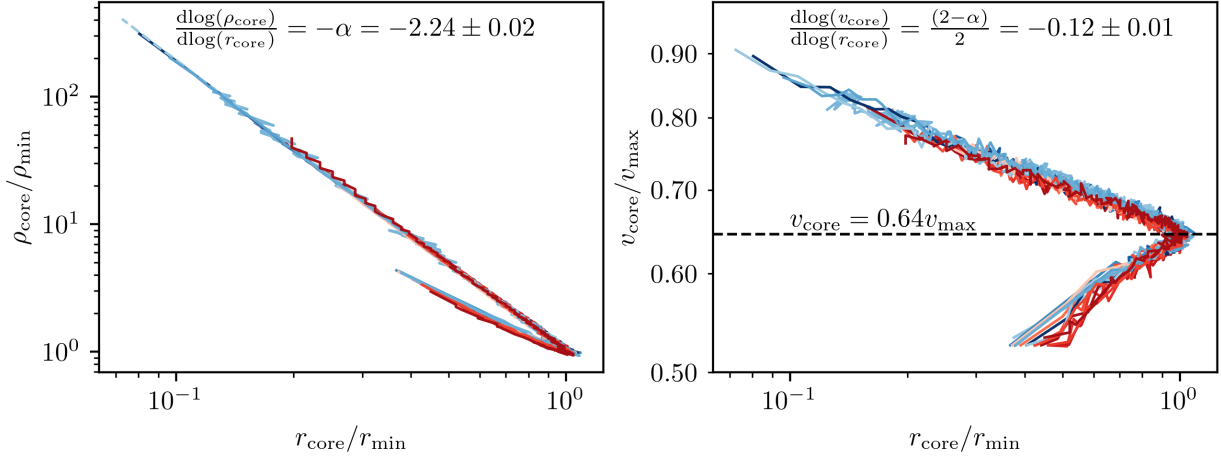


Figure 5.9: **Left:** Core density versus core size for all cross sections and both halos simulated in Table 5.2, 5.1. All exhibit approximately the same power law during core expansion $\alpha_e = 1.43 \pm 0.03$ and during core collapse $\alpha_c = 2.24 \pm 0.02$. **Right:** The core velocity dispersion versus core size. Both core expansion and core collapse exhibit a single power law with the corresponding α that is generally cross-section independent.

Figure 5.9 plots the evolution of core density and core velocity dispersion versus core size. Interestingly, despite major differences in the core state at the maximum core stage, all cross sections produce the same power law. During core collapse $\alpha_c = 2.24$ and during core expansion $\alpha_e = 1.43$. Given these relations, we must only constrain how one of the core properties evolves over time to fully predict core evolution for any cross section. To this end the evolution of core density post the maximum core phase is parameterized for the simulation of the effective cross section. The following function captures the evolution of core density with an error of less than 1 part in 1000 at all times

$$\log(\rho_{\text{core}}/\rho_{\text{min}})(\tilde{t}) = 0.38\tilde{t}^{-7.01} + 0.02\tilde{t}^{37.49} + 0.76, \quad (5.23)$$

where $\tilde{t} = (t - t_{\text{min}})/t_{\text{coll}}$.

Combining this with our parametric fit for the maximum core properties 5.18 and the fact that $v_{\text{min}} \approx 0.645v_{\text{max}}$ regardless of the interaction cross section, we can fully parameterize

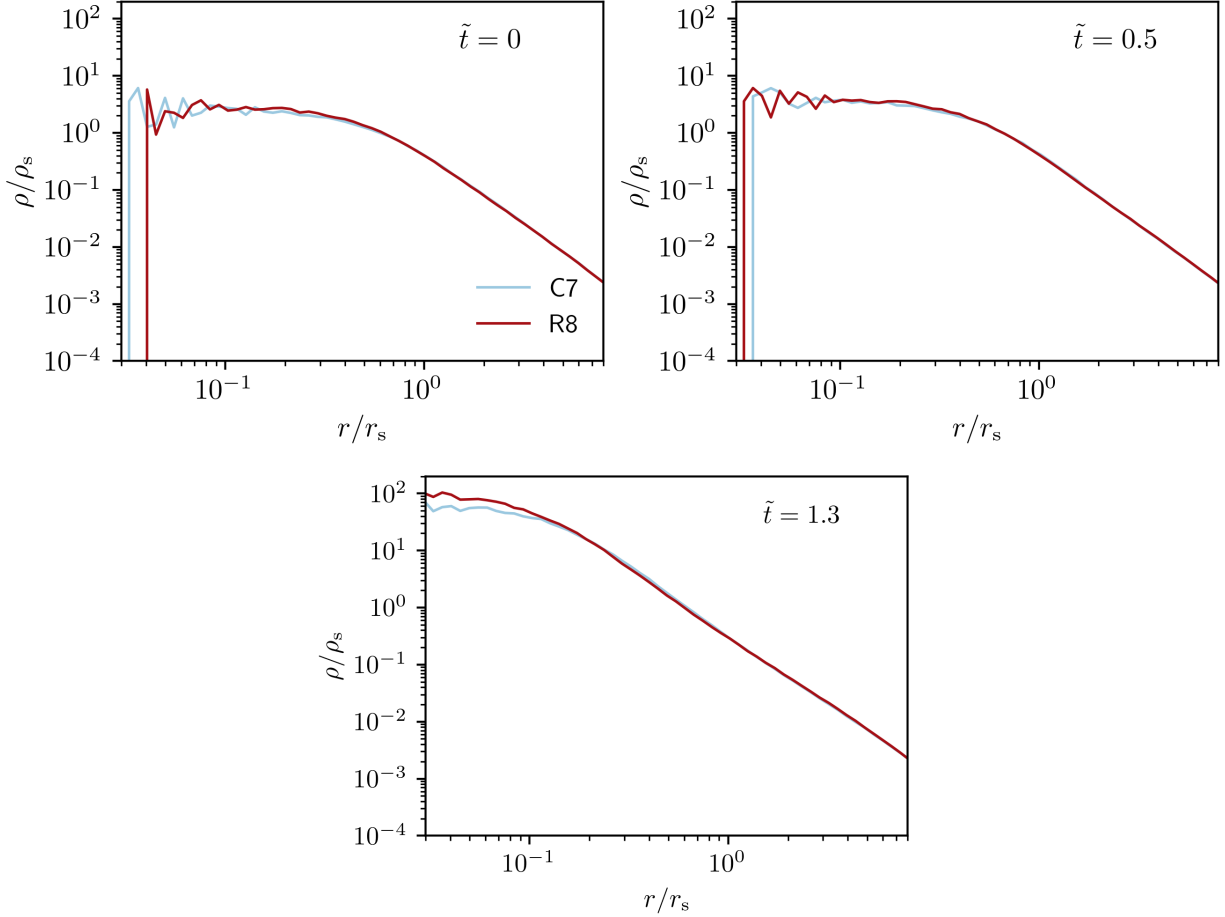


Figure 5.10: Halo density profile at equivalent times in the halo evolution for the cross sections C7 (constant) and R8 (the cross section most dominant at $v_{\text{rel}} \gg v_{\text{max}}$). The differences in the core density are relatively small prior to core collapse, and the outer halo profiles are identical at equivalent times in the halo evolution. However, the differences in the core densities grow far into core collapse due to the remaining scatter in the core collapse time in our analytic fits.

the core properties at any time. Combining the core size-density relation Eq. 5.22 and Eq. 5.18 provides simple relation between core size and core density for any cross section, where the cross section dependence enters through the maximum core parameters ρ_{\min} , time variable \tilde{t} , which in turn depends on t_{\min} and the core collapse time t_{coll}

$$\log(r_{\text{core}}/r_s) = -0.58 \log(\rho_{\min}/\rho_s) - 0.14 - \alpha^{-1} \log(\rho_{\text{core}}/\rho_{\min})(\tilde{t}). \quad (5.24)$$

Similarly, since the core velocity dispersion at maximum core is independent of the interaction cross section, the relationship between the core velocity dispersion and core size is somewhat simpler

$$\log(v_{\text{core}}/v_{\min}) = \frac{(2 - \alpha)}{2} \log(r_{\text{core}}/r_{\min}). \quad (5.25)$$

And finally, combining equations Eqs. 5.19, 5.24 we derive the description for core mass M_{core} as a function of core size.

$$\log(M_{\text{core}}/M_s) = 1.28 \log(r_{\min}/r_s) + 0.39 + (2 - \alpha) \log(r_{\text{core}}/r_{\min}) \quad (5.26)$$

Notably, the differences in the core mass at maximum core will not persist once the core collapse enters the SMFP regime resulting in different core masses once the core becomes relativistic.

5.6.4 Consequences for Black Hole Formation

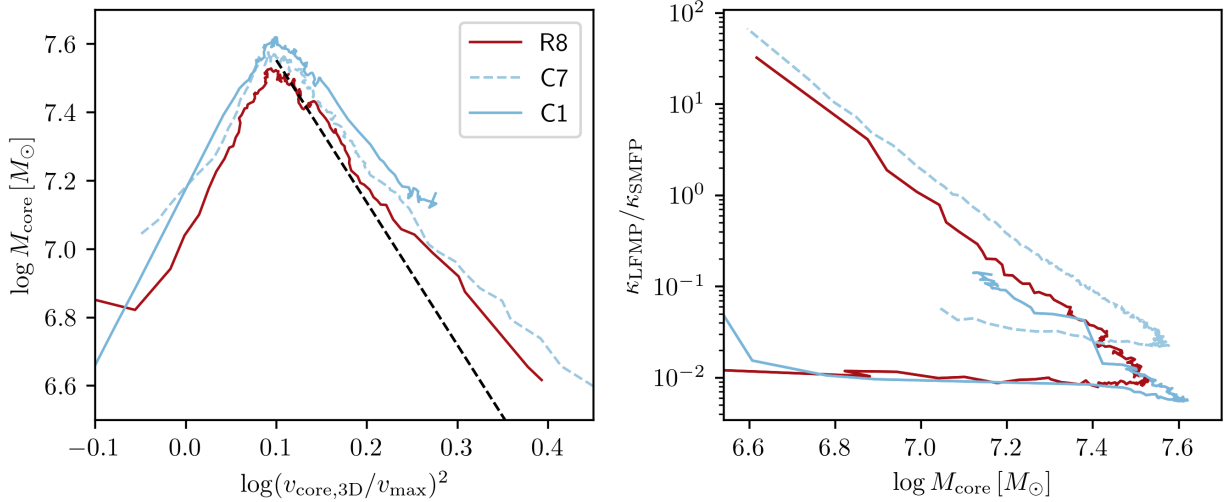


Figure 5.11: **Left:** Halo core mass as a function of core velocity dispersion squared for a simulation sample with a constant, resonant and monotonic cross sections. The analytic prediction for the mass evolution in the LMFP regime is plotted for reference in the black dashed line. Eventually all simulations deviate as they enter the SMFP regime and the core begins to shed less mass as the temperature increases. **Right:** The ratio of the LMFP to SMFP heat conductivity for the halo’s core. Despite initially lower core mass exhibited by cross sections that dominate at $v_{\text{rel}} > v_{\text{max}}$, the R8 cross section transitions to the SMFP regime at a larger core mass compared to cross sections that dominate at $v_{\text{rel}} < v_{\text{max}}$, which could lead to a relatively higher mass black hole once the relativistic instability is reached.

An intriguing result of the runaway gravothermal collapse in the SMFP regime is the potential formation of a black hole. A black hole may form quickly around the time of relativistic instability, when the core dispersion is $v_{\text{core}} \approx c/3$ [9, 8, 27]. As the core temperature rises up to that point, the core mass will shrink. In the LMFP, the mass-temperature scaling is expected to be around $\frac{d\log M_{\text{core}}}{d\log v_{\text{core},3\text{D}}^2} \approx -4.17$. At some point during core collapse, the core has to transition to the SMFP regime where the slope becomes much more shallow i.e. the core sheds less mass as the temperature increases $\frac{d\log M_{\text{core}}}{d\log v_{\text{core},3\text{D}}^2} \approx -1$ (but somewhat less than -1)[61]. Figure 5.11 plots the evolution of the core mass as a function of core temperature, $v_{\text{core},3\text{D}}^2$, for a small sample of the cross sections. These are cross sections C1, R9 which correspond to the minimum and maximum values of $K3/K5$ and C7 which is the constant cross section. For reference, the LMFP scaling is plotted as black dashed line. The cross

sections where scattering is dominant at velocities greater than v_{\max} produce core masses that are initially about $\approx 50\%$ more massive than what is produced by a constant cross section. The converse is true for cross sections where scattering is dominated at velocities smaller than v_{\max} . However, the resonant cross section, R8, transitions to the SMFP regime faster than the Yukawa, C1, counterpart and consequently sheds less mass in the process. Since all cross sections studied here have the same asymptotic behavior

$$\frac{d \log \sigma(v_{\text{rel}})}{d \log(v_{\text{rel}})} = -4, \quad (5.27)$$

the eventual black hole mass resulting from the resonant cross section may be orders of magnitude higher than the Yukawa counterpart. Effectively, a resonance in the cross section at relative velocities $v_{\text{rel}} > v_{\max}$ may preserve core mass by accelerating the transition to the SMFP regime. This estimate requires significant extrapolation of our findings and more work is necessary to determine precisely how large these differences can be.

5.7 Summary

In this paper, we present results of a set of idealised SIDM halo simulations employing a variety of velocity-dependent cross sections. This includes resonance cross sections, whose scattering is strongly dominant at a characteristic relative velocity, and cross sections that are monotonically decreasing with relative velocity. For both monotonic and resonance cross sections, the SIDM halo evolution deviates by a factor of order unity from the previously proposed effective cross section motivated by the kinetic theory of heat conduction.

Resonance cross sections that peak at relative velocities above the halo's v_{\max} tend to form

denser, smaller and less massive cores than halos subjected to a constant cross section by as much as $\approx 30\%$. Conversely, cross sections (resonant or monotonic) whose interactions dominate at velocities smaller than v_{max} form less dense, larger and more massive cores than their constant cross section counterparts. Consequently, SIDM halos with comparable core-collapse timescales have core masses that vary by as much as a factor of 2 depending on the underlying cross section.

The minimum-density core phase has the same velocity dispersion across all the different particle physics models as anticipated by previous results based on solutions to the gravothermal equations. However, the differences in core density and core size affect the rate of halo evolution with the lower density cores taking longer to core collapse and vice-versa. This contributes enough variability in the core collapse time to significantly deviate from the previously proposed universal halo evolution employing a heat transfer cross section of the form $\langle v^5 \sigma_v \rangle$. We note here that the approximate universality appears in the long mean-free path solution to the set of gravothermal equations even if the velocity averaging factor differs from v^5 . Motivated by this, we investigated if there was another way that the universality could be restored. We found that the scatter in the evolution of the core density in models with velocity-dependent cross section is reduced if we use the ratio of cross section averages $\langle v_{\text{rel}}^3 \sigma_v \rangle \langle v_{\text{rel}}^2 \rangle / \langle v_{\text{rel}}^5 \sigma_v \rangle$ to get better estimates of the minimum density, time when that is achieved and the collapse time. We tested other averages and found that adding more information or other averages don't decrease the scatter.

The form of universality suggested in Ref. [155] required only that the time-scale be defined with a specific velocity average of the cross section. In this sense, we have not been able to recover the approximate universality by only rescaling one time-scale. We found that it was also important to rescale the minimum density as a function of the ratio of cross section averages. Further we found that the ratio of collapse time to time when minimum density is achieved, varied systematically with the cross section model and some of this variation

could be removed with the same ratio of cross section averages. Our final result in Figure 6 could be seen as an approximate universality but we stress that it doesn't have the same theoretical description in terms of solutions to the gravothermal equations as was found for monotonically decreasing cross sections.

This work contributes to the increasingly more precise analytical modeling of SIDM halos. Combining our fits with the work of Ref. [230] makes it possible to predict the profiles of MW dwarfs for any interaction cross section and without running additional N-body simulations. With these tools, one can efficiently explore a wide range of cross sections and constrain the 3-parameter space for monotonic/resonant cross sections by comparing the predicted properties of MW dwarfs to their observed properties. We plan to explore this critical subject in a subsequent study.

Bibliography

- [1] *New light on dark stars : red dwarfs, low mass stars, brown dwarfs*, Jan. 2000.
- [2] D. S. Abbot, A. Voigt, D. Li, G. Le Hir, R. T. Pierrehumbert, M. Branson, D. Pollard, and D. D. B. Koll. Robust elements of Snowball Earth atmospheric circulation and oases for life. *Journal of Geophysical Research (Atmospheres)*, 118(12):6017–6027, Jun 2013.
- [3] S. Adhikari et al. Astrophysical Tests of Dark Matter Self-Interactions. 7 2022.
- [4] K. E. Andrade, J. Fuson, S. Gad-Nasr, D. Kong, Q. Minor, M. G. Roberts, and M. Kaplinghat. A stringent upper limit on dark matter self-interaction cross-section from cluster strong lensing. , 510(1):54–81, Feb. 2022.
- [5] K. E. Andrade, Q. Minor, A. Nierenberg, and M. Kaplinghat. Detecting dark matter cores in galaxy clusters with strong lensing. , 487(2):1905–1926, Aug. 2019.
- [6] G. Anglada-Escudé, P. J. Amado, J. Barnes, Z. M. Berdiñas, R. P. Butler, G. A. L. Coleman, I. de la Cueva, S. Dreizler, M. Endl, B. Giesers, S. V. Jeffers, J. S. Jenkins, H. R. A. Jones, M. Kiraga, M. Kürster, M. J. López-González, C. J. Marvin, N. Morales, J. Morin, R. P. Nelson, J. Ortiz, A. Ofir, S.-J. Paardekooper, A. Reiners, E. Rodríguez, C. Rodríguez-López, L. F. Sarmiento, J. P. Strachan, Y. Tsapras, M. Tuomi, and M. Zechmeister. A terrestrial planet candidate in a temperate orbit around proxima centauri. *Nature*, 536(7617):437–440, 08 2016.
- [7] J. C. Armstrong, R. Barnes, S. Domagal-Goldman, J. Breiner, T. R. Quinn, and V. S. Meadows. Effects of Extreme Obliquity Variations on the Habitability of Exoplanets. *Astrobiology*, 14(4):277–291, Apr. 2014.
- [8] S. Balberg and S. L. Shapiro. Gravothermal Collapse of Self-Interacting Dark Matter Halos and the Origin of Massive Black Holes. , 88(10):101301, Mar. 2002.
- [9] S. Balberg, S. L. Shapiro, and S. Inagaki. Self-Interacting Dark Matter Halos and the Gravothermal Catastrophe. , 568(2):475–487, Apr. 2002.
- [10] A. Banerjee, S. Adhikari, N. Dalal, S. More, and A. Kravtsov. Signatures of self-interacting dark matter on cluster density profile and subhalo distributions. , 2020(2):024, Feb. 2020.

- [11] R. Barnes, S. N. Raymond, B. Jackson, and R. Greenberg. Tides and the Evolution of Planetary Habitability. *Astrobiology*, 8(3):557–568, Jun 2008.
- [12] Z. Berezhiani. Through the Looking-Glass Alice’s Adventures in Mirror World. In *From Fields to Strings: Circumnavigating Theoretical Physics: Ian Kogan Memorial Collection (in 3 Vols)*. Edited by SHIFMAN MISHA ET AL. Published by World Scientific Publishing Co. Pte. Ltd, pages 2147–2195. 2005.
- [13] S. I. Blinnikov and M. Y. Khlopov. Possible Astronomical Effects of Mirror Particles. , 27:371–375, Aug. 1983.
- [14] K. K. Boddy, J. L. Feng, M. Kaplinghat, and T. M. P. Tait. Self-interacting dark matter from a non-Abelian hidden sector. , 89(11):115017, June 2014.
- [15] E. Bolmont, A.-S. Libert, J. Leconte, and F. Selsis. Habitability of planets on eccentric orbits: Limits of the mean flux approximation. , 591:A106, June 2016.
- [16] E. Bolmont, F. Selsis, J. E. Owen, I. Ribas, S. N. Raymond, J. Leconte, and M. Gillon. Water loss from terrestrial planets orbiting ultracool dwarfs: implications for the planets of TRAPPIST-1. , 464(3):3728–3741, Jan 2017.
- [17] W. J. Borucki. KEPLER Mission: development and overview. *Reports on Progress in Physics*, 79(3):036901, Mar. 2016.
- [18] S. Bose, W. A. Hellwing, C. S. Frenk, A. Jenkins, M. R. Lovell, J. C. Helly, B. Li, V. Gonzalez-Perez, and L. Gao. Substructure and galaxy formation in the Copernicus Complexio warm dark matter simulations. , 464(4):4520–4533, Feb. 2017.
- [19] M. Boylan-Kolchin, J. S. Bullock, and M. Kaplinghat. Too big to fail? The puzzling darkness of massive Milky Way subhaloes. , 415(1):L40–L44, July 2011.
- [20] M. Boylan-Kolchin, J. S. Bullock, and M. Kaplinghat. The Milky Way’s bright satellites as an apparent failure of Λ CDM. , 422(2):1203–1218, May 2012.
- [21] M. T. Brady, E. A. Petigura, H. A. Knutson, E. Sinukoff, H. Isaacson, L. A. Hirsch, B. J. Fulton, M. R. Kosiarek, and A. W. Howard. Kepler-1656b: A Dense Sub-Saturn with an Extreme Eccentricity. , 156(4):147, Oct 2018.
- [22] J. S. Bullock and M. Boylan-Kolchin. Small-Scale Challenges to the Λ CDM Paradigm. , 55(1):343–387, Aug. 2017.
- [23] J. S. Bullock, A. V. Kravtsov, and D. H. Weinberg. Reionization and the Abundance of Galactic Satellites. , 539(2):517–521, Aug. 2000.
- [24] A. Burkert. The Structure and Evolution of Weakly Self-interacting Cold Dark Matter Halos. , 534(2):L143–L146, May 2000.
- [25] D. Ceverino, A. Klypin, E. S. Klimek, S. Trujillo-Gomez, C. W. Churchill, J. Primack, and A. Dekel. Radiative feedback and the low efficiency of galaxy formation in low-mass haloes at high redshift. , 442(2):1545–1559, Aug. 2014.

- [26] K. Chance and R. L. Kurucz. An improved high-resolution solar reference spectrum for earth’s atmosphere measurements in the ultraviolet, visible, and near infrared. , 111(9):1289–1295, Jun 2010.
- [27] J. Choquette, J. M. Cline, and J. M. Cornell. Early formation of supermassive black holes via dark matter self-interactions. , 2019(7):036, July 2019.
- [28] X. Chu, C. Garcia-Cely, and H. Murayama. Velocity Dependence from Resonant Self-Interacting Dark Matter. , 122(7):071103, Feb. 2019.
- [29] X. Chu, C. Garcia-Cely, and H. Murayama. A practical and consistent parametrization of dark matter self-interactions. , 2020(6):043, June 2020.
- [30] D. Clowe, M. Bradač, A. H. Gonzalez, M. Markevitch, S. W. Randall, C. Jones, and D. Zaritsky. A Direct Empirical Proof of the Existence of Dark Matter. , 648(2):L109–L113, Sept. 2006.
- [31] B. Colquhoun, S. Heeba, F. Kahlhoefer, L. Sagunski, and S. Tulin. Semiclassical regime for dark matter self-interactions. , 103(3):035006, Feb. 2021.
- [32] C. A. Correa. Constraining velocity-dependent self-interacting dark matter with the Milky Way’s dwarf spheroidal galaxies. , 503(1):920–937, May 2021.
- [33] C. A. Correa, M. Schaller, S. Ploekinger, N. Anau Montel, C. Weniger, and S. Ando. TangoSIDM: tantalizing models of self-interacting dark matter. , 517(2):3045–3063, Dec. 2022.
- [34] P. Creasey, O. Sameie, L. V. Sales, H.-B. Yu, M. Vogelsberger, and J. Zavala. Spreading out and staying sharp - creating diverse rotation curves via baryonic and self-interaction effects. , 468(2):2283–2295, June 2017.
- [35] A. Ç. Şengül and C. Dvorkin. Probing dark matter with strong gravitational lensing through an effective density slope. , 516(1):336–357, Oct. 2022.
- [36] A. c. Şengül and C. Dvorkin. Probing dark matter with strong gravitational lensing through an effective density slope. *Mon. Not. Roy. Astron. Soc.*, 516(1):336–357, 2022.
- [37] G. D’Amico, P. Panci, A. Lupi, S. Bovino, and J. Silk. Massive black holes from dissipative dark matter. , 473(1):328–335, Jan. 2018.
- [38] A. Dekel and J. Silk. The Origin of Dwarf Galaxies, Cold Dark Matter, and Biased Galaxy Formation. , 303:39, Apr. 1986.
- [39] J. A. Dittmann, J. M. Irwin, D. Charbonneau, X. Bonfils, N. Astudillo-Defru, R. D. Haywood, Z. K. Berta-Thompson, E. R. Newton, J. E. Rodriguez, J. G. Winters, T.-G. Tan, J.-M. Almenara, F. Bouchy, X. Delfosse, T. Forveille, C. Lovis, F. Murgas, F. Pepe, N. C. Santos, S. Udry, A. Wünsche, G. A. Esquerdo, D. W. Latham, and C. D. Dressing. A temperate rocky super-Earth transiting a nearby cool star. , 544:333–336, Apr. 2017.

- [40] A. R. Dobrovolskis. Spin states and climates of eccentric exoplanets. , 192(1):1–23, Dec 2007.
- [41] S. H. Dole. *Habitable planets for man*. 1964.
- [42] C. D. Dressing, D. S. Spiegel, C. A. Scharf, K. Menou, and S. N. Raymond. Habitable Climates: The Influence of Eccentricity. , 721(2):1295–1307, Oct 2010.
- [43] A. Drlica-Wagner, K. Bechtol, S. Mau, M. McNanna, E. O. Nadler, A. B. Pace, T. S. Li, A. Pieres, E. Rozo, J. D. Simon, A. R. Walker, R. H. Wechsler, T. M. C. Abbott, S. Allam, J. Annis, E. Bertin, D. Brooks, D. L. Burke, A. C. Rosell, M. Carrasco Kind, J. Carretero, M. Costanzi, L. N. da Costa, J. De Vicente, S. Desai, H. T. Diehl, P. Doel, T. F. Eifler, S. Everett, B. Flaugher, J. Frieman, J. García-Bellido, E. Gaztanaga, D. Gruen, R. A. Gruendl, J. Gschwend, G. Gutierrez, K. Honscheid, D. J. James, E. Krause, K. Kuehn, N. Kuropatkin, O. Lahav, M. A. G. Maia, J. L. Marshall, P. Melchior, F. Menanteau, R. Miquel, A. Palmese, A. A. Plazas, E. Sanchez, V. Scarpine, M. Schubnell, S. Serrano, I. Sevilla-Noarbe, M. Smith, E. Suchyta, G. Tarle, and DES Collaboration. Milky Way Satellite Census. I. The Observational Selection Function for Milky Way Satellites in DES Y3 and Pan-STARRS DR1. , 893(1):47, Apr. 2020.
- [44] A. Drlica-Wagner, K. Bechtol, E. S. Rykoff, E. Luque, A. Queiroz, Y. Y. Mao, R. H. Wechsler, J. D. Simon, B. Santiago, B. Yanny, E. Balbinot, S. Dodelson, A. Fausti Neto, D. J. James, T. S. Li, M. A. G. Maia, J. L. Marshall, A. Pieres, K. Stringer, A. R. Walker, T. M. C. Abbott, F. B. Abdalla, S. Allam, A. Benoit-Lévy, G. M. Bernstein, E. Bertin, D. Brooks, E. Buckley-Geer, D. L. Burke, A. Carnero Rosell, M. Carrasco Kind, J. Carretero, M. Crocce, L. N. da Costa, S. Desai, H. T. Diehl, J. P. Dietrich, P. Doel, T. F. Eifler, A. E. Evrard, D. A. Finley, B. Flaugher, P. Fosalba, J. Frieman, E. Gaztanaga, D. W. Gerdes, D. Gruen, R. A. Gruendl, G. Gutierrez, K. Honscheid, K. Kuehn, N. Kuropatkin, O. Lahav, P. Martini, R. Miquel, B. Nord, R. Ogando, A. A. Plazas, K. Reil, A. Roodman, M. Sako, E. Sanchez, V. Scarpine, M. Schubnell, I. Sevilla-Noarbe, R. C. Smith, M. Soares-Santos, F. Sobreira, E. Suchyta, M. E. C. Swanson, G. Tarle, D. Tucker, V. Vikram, W. Wester, Y. Zhang, J. Zuntz, and DES Collaboration. Eight Ultra-faint Galaxy Candidates Discovered in Year Two of the Dark Energy Survey. , 813(2):109, Nov. 2015.
- [45] R. V. Dunkle and J. T. Bevens. A Approximate Analysis of the Solar Reflectance and Transmittance of a Snow Cover. *Journal of Atmospheric Sciences*, 13(2):212–216, Apr 1956.
- [46] A. Edson, S. Lee, P. Bannon, J. F. Kasting, and D. Pollard. Atmospheric circulations of terrestrial planets orbiting low-mass stars. , 212:1–13, Mar. 2011.
- [47] G. Efstathiou. Suppressing the formation of dwarf galaxies via photoionization. , 256(2):43P–47P, May 1992.
- [48] O. D. Elbert, J. S. Bullock, S. Garrison-Kimmel, M. Rocha, J. Oñorbe, and A. H. G. Peter. Core formation in dwarf haloes with self-interacting dark matter: no fine-tuning necessary. , 453(1):29–37, Oct. 2015.

- [49] O. D. Elbert, J. S. Bullock, S. Garrison-Kimmel, M. Rocha, J. Oñorbe, and A. H. G. Peter. Core formation in dwarf haloes with self-interacting dark matter: no fine-tuning necessary. *Mon. Not. Roy. Astron. Soc.*, 453(1):29–37, 2015.
- [50] N. V. Erkaev, Y. N. Kulikov, H. Lammer, F. Selsis, D. Langmayr, G. F. Jaritz, and H. K. Biernat. Roche lobe effects on the atmospheric loss from “Hot Jupiters”. , 472:329–334, Sept. 2007.
- [51] R. Essig, S. D. McDermott, H.-B. Yu, and Y.-M. Zhong. Constraining Dissipative Dark Matter Self-Interactions. , 123(12):121102, Sept. 2019.
- [52] D. Feldman, Z. Liu, and P. Nath. PAMELA positron excess as a signal from the hidden sector. , 79(6):063509, Mar. 2009.
- [53] J. L. Feng, M. Kaplinghat, and H.-B. Yu. Sommerfeld enhancements for thermal relic dark matter. , 82(8):083525, Oct. 2010.
- [54] W.-X. Feng, H.-B. Yu, and Y.-M. Zhong. Seeding Supermassive Black Holes with Self-interacting Dark Matter: A Unified Scenario with Baryons. , 914(2):L26, June 2021.
- [55] D. Ferreira, J. Marshall, P. A. O’Gorman, and S. Seager. Climate at high-obliquity. , 243:236–248, Nov. 2014.
- [56] M. S. Fischer, M. Brüggen, K. Schmidt-Hoberg, K. Dolag, F. Kahlhoefer, A. Ragagnin, and A. Robertson. N-body simulations of dark matter with frequent self-interactions. , 505(1):851–868, July 2021.
- [57] R. A. Flores and J. R. Primack. Observational and Theoretical Constraints on Singular Dark Matter Halos. , 427:L1, May 1994.
- [58] R. Foot. Mirror Matter-Type Dark Matter. *International Journal of Modern Physics D*, 13(10):2161–2192, Jan. 2004.
- [59] A. B. Fry, F. Governato, A. Pontzen, T. Quinn, M. Tremmel, L. Anderson, H. Menon, A. M. Brooks, and J. Wadsley. All about baryons: revisiting SIDM predictions at small halo masses. , 452(2):1468–1479, Sept. 2015.
- [60] Y. Fujii, D. Angerhausen, R. Deitrick, S. Domagal-Goldman, J. L. Grenfell, Y. Hori, S. R. Kane, E. Pallé, H. Rauer, N. Siegler, K. Stapelfeldt, and K. B. Stevenson. Exoplanet Biosignatures: Observational Prospects. *Astrobiology*, 18(6):739–778, June 2018.
- [61] S. Gad-Nasr, K. K. Boddy, M. Kaplinghat, N. J. Outmezguine, and L. Sagunski. On the Late-Time Evolution of Velocity-Dependent Self-Interacting Dark Matter Halos. *arXiv e-prints*, page arXiv:2312.09296, Dec. 2023.
- [62] C. García-Cely, G. Landini, and Ó. Zapata. Dark matter in QCD-like theories with a theta vacuum: cosmological and astrophysical implications. *arXiv e-prints*, page arXiv:2405.10367, May 2024.

- [63] S. Garrison-Kimmel, M. Rocha, M. Boylan-Kolchin, J. S. Bullock, and J. Lally. Can feedback solve the too-big-to-fail problem? , 433(4):3539–3546, Aug. 2013.
- [64] S. Garrison-Kimmel, A. Wetzel, J. S. Bullock, P. F. Hopkins, M. Boylan-Kolchin, C.-A. Faucher-Giguère, D. Kereš, E. Quataert, R. E. Sanderson, A. S. Graus, and T. Kelley. Not so lumpy after all: modelling the depletion of dark matter subhaloes by Milky Way-like galaxies. , 471(2):1709–1727, Oct. 2017.
- [65] M. J. Giguere, D. A. Fischer, A. W. Howard, J. A. Johnson, G. W. Henry, J. T. Wright, G. W. Marcy, H. T. Isaacson, F. Hou, and J. Spronck. A High-eccentricity Component in the Double-planet System around HD 163607 and a Planet around HD 164509. , 744(1):4, Jan 2012.
- [66] M. Gillon, A. H. M. J. Triaud, B.-O. Demory, E. Jehin, E. Agol, K. M. Deck, S. M. Lederer, J. de Wit, A. Burdanov, J. G. Ingalls, E. Bolmont, J. Leconte, S. N. Raymond, F. Selsis, M. Turbet, K. Barkaoui, A. Burgasser, M. R. Burleigh, S. J. Carey, A. Chauhev, C. M. Copperwheat, L. Delrez, C. S. Fernandes, D. L. Holdsworth, E. J. Kotze, V. Van Grootel, Y. Almleaky, Z. Benkhaldoun, P. Magain, and D. Queloz. Seven temperate terrestrial planets around the nearby ultracool dwarf star TRAPPIST-1. , 542:456–460, Feb. 2017.
- [67] S. Girmohanta and R. Shrock. Cross section calculations in theories of self-interacting dark matter. *Phys. Rev. D*, 106(6):063013, 2022.
- [68] P. Gondolo and G. Gelmini. Cosmic abundances of stable particles: improved analysis. *Nuclear Physics B*, 360(1):145–179, Aug. 1991.
- [69] F. Governato, A. Zolotov, A. Pontzen, C. Christensen, S. H. Oh, A. M. Brooks, T. Quinn, S. Shen, and J. Wadsley. Cuspy no more: how outflows affect the central dark matter and baryon distribution in Λ cold dark matter galaxies. , 422(2):1231–1240, May 2012.
- [70] K. Griest and D. Seckel. Three exceptions in the calculation of relic abundances. *Phys. Rev. D*, 43:3191–3203, May 1991.
- [71] J. Guo, F. Zhang, X. Chen, and Z. Han. Probability distribution of terrestrial planets in habitable zones around host stars. , 323:367–373, Oct. 2009.
- [72] R. M. Haberle, C. P. McKay, D. Tyler, and R. T. Reynolds. Can Synchronously Rotating Planets Support An Atmosphere? In L. R. Doyle, editor, *Circumstellar Habitable Zones*, page 29, Jan. 1996.
- [73] H. Harakawa, B. Sato, M. Omiya, D. A. Fischer, Y. Hori, S. Ida, E. Kambe, M. Yoshida, H. Izumiura, H. Koyano, S. Nagayama, Y. Shimizu, N. Okada, K. Okita, A. Sakamoto, and T. Yamamuro. Five New Exoplanets Orbiting Three Metal-rich, Massive Stars: Two-planet Systems Including Long-period Planets and an Eccentric Planet. , 806(1):5, Jun 2015.

- [74] J. R. Hargis, B. Willman, and A. H. G. Peter. Too many, too few, or just right? the predicted number and distribution of milky way dwarf galaxies. *The Astrophysical Journal Letters*, 795(1):L13, oct 2014.
- [75] R. Heller and R. Barnes. Runaway greenhouse effect on exomoons due to irradiation from hot, young giant planets. *International Journal of Astrobiology*, 14(2):335–343, Apr 2015.
- [76] L. Hernquist. An Analytical Model for Spherical Galaxies and Bulges. , 356:359, June 1990.
- [77] S. Hess, J. Ryan, J. Tillman, R. Henry, and C. Leovy. The annual cycle of pressure on mars measured by viking landers 1 and 2. *Geophysical Research Letters*, 7(3):197–200, 1980. cited By 100.
- [78] P. F. Hopkins. A new class of accurate, mesh-free hydrodynamic simulation methods. , 450(1):53–110, June 2015.
- [79] P. F. Hopkins, D. Kereš, J. Oñorbe, C.-A. Faucher-Giguère, E. Quataert, N. Murray, and J. S. Bullock. Galaxies on FIRE (Feedback In Realistic Environments): stellar feedback explains cosmologically inefficient star formation. , 445(1):581–603, Nov. 2014.
- [80] P. F. Hopkins, A. Wetzel, D. Kereš, C.-A. Faucher-Giguère, E. Quataert, M. Boylan-Kolchin, N. Murray, C. C. Hayward, S. Garrison-Kimmel, C. Hummels, R. Feldmann, P. Torrey, X. Ma, D. Anglés-Alcázar, K.-Y. Su, M. Orr, D. Schmitz, I. Escala, R. Sanderson, M. Y. Grudić, Z. Hafen, J.-H. Kim, A. Fitts, J. S. Bullock, C. Wheeler, T. K. Chan, O. D. Elbert, and D. Narayanan. FIRE-2 simulations: physics versus numerics in galaxy formation. , 480(1):800–863, Oct. 2018.
- [81] E. C. Hunke and W. H. Lipscomb. *CICE: The Los Alamos Sea Ice Model. Documentation and Software User’s Manual. Version 4.0.* T-3 Fluid Dynamics Group, Los Alamos National Laboratory, Tech. Rep. LA-CC-06-012., 2008.
- [82] M. Ibe, H. Murayama, and T. T. Yanagida. Breit-Wigner enhancement of dark matter annihilation. , 79(9):095009, May 2009.
- [83] A. P. Ingersoll. The Runaway Greenhouse: A History of Water on Venus. *Journal of Atmospheric Sciences*, 26(6):1191–1198, Nov 1969.
- [84] F. Jiang, A. Benson, P. F. Hopkins, O. Slone, M. Lisanti, M. Kaplinghat, A. H. G. Peter, Z. C. Zeng, X. Du, S. Yang, and X. Shen. A semi-analytic study of self-interacting dark-matter haloes with baryons. , 521(3):4630–4644, May 2023.
- [85] H. R. A. Jones, R. P. Butler, C. G. Tinney, G. W. Marcy, B. D. Carter, A. J. Penny, C. McCarthy, and J. Bailey. High-eccentricity planets from the Anglo-Australian Planet Search. , 369(1):249–256, Jun 2006.

- [86] M. Joshi. Climate Model Studies of Synchronously Rotating Planets. *Astrobiology*, 3(2):415–427, June 2003.
- [87] M. M. Joshi, R. M. Haberle, and R. T. Reynolds. Simulations of the Atmospheres of Synchronously Rotating Terrestrial Planets Orbiting M Dwarfs: Conditions for Atmospheric Collapse and the Implications for Habitability. , 129:450–465, Oct. 1997.
- [88] G. Jungman, M. Kamionkowski, and K. Griest. Supersymmetric dark matter. , 267:195–373, Mar. 1996.
- [89] F. Kahlhoefer, M. Kaplinghat, T. R. Slatyer, and C.-L. Wu. Diversity in density profiles of self-interacting dark matter satellite halos. , 2019(12):010, Dec. 2019.
- [90] A. Kamada, M. Kaplinghat, A. B. Pace, and H.-B. Yu. Self-Interacting Dark Matter Can Explain Diverse Galactic Rotation Curves. , 119(11):111102, Sept. 2017.
- [91] S. R. Kane, R. A. Wittenmyer, N. R. Hinkel, A. Roy, S. Mahadevan, D. Dragomir, J. M. Matthews, G. W. Henry, A. Chakraborty, T. S. Boyajian, J. T. Wright, D. R. Ciardi, D. A. Fischer, R. P. Butler, C. G. Tinney, B. D. Carter, H. R. A. Jones, J. Bailey, and S. J. O’Toole. Evidence for Reflected Light from the Most Eccentric Exoplanet Known. , 821(1):65, Apr 2016.
- [92] M. Kaplinghat, R. E. Keeley, T. Linden, and H.-B. Yu. Tying Dark Matter to Baryons with Self-Interactions. , 113(2):021302, July 2014.
- [93] M. Kaplinghat, S. Tulin, and H.-B. Yu. Dark Matter Halos as Particle Colliders: Unified Solution to Small-Scale Structure Puzzles from Dwarfs to Clusters. , 116(4):041302, Jan. 2016.
- [94] M. Kaplinghat, M. Valli, and H.-B. Yu. Too big to fail in light of Gaia. , 490(1):231–242, Nov. 2019.
- [95] J. F. Kasting, H. Chen, and R. K. Kopparapu. Stratospheric Temperatures and Water Loss from Moist Greenhouse Atmospheres of Earth-like Planets. , 813(1):L3, Nov 2015.
- [96] J. F. Kasting, D. P. Whitmire, and R. T. Reynolds. Habitable Zones around Main Sequence Stars. , 101(1):108–128, Jan 1993.
- [97] M. Y. Khlopov, G. M. Beskin, N. G. Bochkarev, L. A. Pustilnik, and S. A. Pustilnik. Observational Physics of the Mirror World. , 35:21, Feb. 1991.
- [98] M. L. Khodachenko, I. Ribas, H. Lammer, J.-M. Grießmeier, M. Leitner, F. Selsis, C. Eiroa, A. Hanslmeier, H. K. Biernat, C. J. Farrugia, and H. O. Rucker. Coronal Mass Ejection (CME) Activity of Low Mass M Stars as An Important Factor for The Habitability of Terrestrial Exoplanets. I. CME Impact on Expected Magnetospheres of Earth-Like Exoplanets in Close-In Habitable Zones. *Astrobiology*, 7(1):167–184, Feb 2007.

- [99] S. Y. Kim and A. H. G. Peter. The Milky Way satellite velocity function is a sharp probe of small-scale structure problems. *arXiv e-prints*, page arXiv:2106.09050, June 2021.
- [100] A. Klypin, S. Gottlöber, A. V. Kravtsov, and A. M. Khokhlov. Galaxies in N-Body Simulations: Overcoming the Overmerging Problem. , 516(2):530–551, May 1999.
- [101] A. Klypin, I. Karachentsev, D. Makarov, and O. Nasonova. Abundance of field galaxies. , 454(2):1798–1810, Dec. 2015.
- [102] A. A. Klypin, S. Trujillo-Gomez, and J. Primack. Dark Matter Halos in the Standard Cosmological Model: Results from the Bolshoi Simulation. , 740(2):102, Oct. 2011.
- [103] C. S. Kochanek and M. White. A Quantitative Study of Interacting Dark Matter in Halos. , 543(2):514–520, Nov. 2000.
- [104] J. Koda and P. R. Shapiro. Gravothermal collapse of isolated self-interacting dark matter haloes: N-body simulation versus the fluid model. , 415(2):1125–1137, Aug. 2011.
- [105] D. D. B. Koll and T. W. Cronin. Earth’s outgoing longwave radiation linear due to H₂O greenhouse effect. *Proceedings of the National Academy of Science*, 115(41):10293–10298, Oct 2018.
- [106] R. K. Kopparapu. A Revised Estimate of the Occurrence Rate of Terrestrial Planets in the Habitable Zones around Kepler M-dwarfs. , 767(1):L8, Apr 2013.
- [107] R. K. Kopparapu, R. Ramirez, J. F. Kasting, V. Eymet, T. D. Robinson, S. Mahadevan, R. C. Terrien, S. Domagal-Goldman, V. Meadows, and R. Deshpande. Erratum: ”Habitable Zones around Main-sequence Stars: New Estimates”. , 770:82, June 2013.
- [108] R. K. Kopparapu, R. Ramirez, J. F. Kasting, V. Eymet, T. D. Robinson, S. Mahadevan, R. C. Terrien, S. Domagal-Goldman, V. Meadows, and R. Deshpande. Habitable Zones around Main-sequence Stars: New Estimates. , 765(2):131, Mar 2013.
- [109] R. k. Kopparapu, E. T. Wolf, G. Arney, N. E. Batalha, J. Haqq-Misra, S. L. Grimm, and K. Heng. Habitable Moist Atmospheres on Terrestrial Planets near the Inner Edge of the Habitable Zone around M Dwarfs. , 845(1):5, Aug 2017.
- [110] R. k. Kopparapu, E. T. Wolf, J. Haqq-Misra, J. Yang, J. F. Kasting, V. Meadows, R. Terrien, and S. Mahadevan. The Inner Edge of the Habitable Zone for Synchronously Rotating Planets around Low-mass Stars Using General Circulation Models. , 819(1):84, Mar. 2016.
- [111] S. G. Korzennik, T. M. Brown, D. A. Fischer, P. Nisenson, and R. W. Noyes. A High-Eccentricity Low-Mass Companion to HD 89744. , 533(2):L147–L150, Apr 2000.
- [112] J. Kummer, F. Kahlhoefer, and K. Schmidt-Hoberg. Effective description of dark matter self-interactions in small dark matter haloes. , 474(1):388–399, Feb. 2018.

- [113] R. Kuzio de Naray, G. D. Martinez, J. S. Bullock, and M. Kaplinghat. The Case Against Warm or Self-Interacting Dark Matter as Explanations for Cores in Low Surface Brightness Galaxies. , 710(2):L161–L166, Feb. 2010.
- [114] B. P. M. Laevens, N. F. Martin, E. J. Bernard, E. F. Schlafly, B. Sesar, H.-W. Rix, E. F. Bell, A. M. N. Ferguson, C. T. Slater, W. E. Sweeney, R. F. G. Wyse, A. P. Huxor, W. S. Burgett, K. C. Chambers, P. W. Draper, K. W. Hodapp, N. Kaiser, E. A. Magnier, N. Metcalfe, J. L. Tonry, R. J. Wainscoat, and C. Waters. Sagittarius II, Draco II and Laevens 3: Three New Milky Way Satellites Discovered in the Pan-STARRS 1 3π Survey. , 813(1):44, Nov. 2015.
- [115] H. Lammer, H. I. M. Lichtenegger, Y. N. Kulikov, J.-M. Grießmeier, N. Terada, N. V. Erkaev, H. K. Biernat, M. L. Khodachenko, I. Ribas, T. Penz, and F. Selsis. Coronal Mass Ejection (CME) Activity of Low Mass M Stars as An Important Factor for The Habitability of Terrestrial Exoplanets. II. CME-Induced Ion Pick Up of Earth-like Exoplanets in Close-In Habitable Zones. *Astrobiology*, 7(1):185–207, Feb 2007.
- [116] H. Lammer, P. Odert, M. Leitzinger, M. L. Khodachenko, M. Panchenko, Y. N. Kulikov, T. L. Zhang, H. I. M. Lichtenegger, N. V. Erkaev, G. Wuchterl, G. Micela, T. Penz, H. K. Biernat, J. Weingrill, M. Steller, H. Ottacher, J. Hasiba, and A. Hanslmeier. Determining the mass loss limit for close-in exoplanets: what can we learn from transit observations? , 506(1):399–410, Oct 2009.
- [117] M. A. Latif, A. Lupi, D. R. G. Schleicher, G. D’Amico, P. Panci, and S. Bovino. Black hole formation in the context of dissipative dark matter. , 485(3):3352–3359, May 2019.
- [118] A. Lazar, J. S. Bullock, M. Boylan-Kolchin, T. K. Chan, P. F. Hopkins, A. S. Graus, A. Wetzel, K. El-Badry, C. Wheeler, M. C. Straight, D. Kereš, C.-A. Faucher-Giguère, A. Fitts, and S. Garrison-Kimmel. A dark matter profile to model diverse feedback-induced core sizes of Λ CDM haloes. , 497(2):2393–2417, Sept. 2020.
- [119] J. Leconte. Continuous reorientation of synchronous terrestrial planets due to mantle convection. *Nature Geoscience*, 11(3):168–172, Feb. 2018.
- [120] J. Leconte, F. Forget, B. Charnay, R. Wordsworth, F. Selsis, E. Millour, and A. Spiga. 3D climate modeling of close-in land planets: Circulation patterns, climate moist bistability, and habitability. , 554:A69, June 2013.
- [121] N. T. Lewis, F. H. Lambert, I. A. Boutle, N. J. Mayne, J. Manners, and D. M. Acreman. The Influence of a Substellar Continent on the Climate of a Tidally Locked Exoplanet. , 854(2):171, Feb. 2018.
- [122] A. P. Lincowski, V. S. Meadows, D. Crisp, T. D. Robinson, R. Luger, J. Lustig-Yaeger, and G. N. Arney. Evolved Climates and Observational Discriminants for the TRAPPIST-1 Planetary System. , 867(1):76, Nov. 2018.

- [123] R. S. Lindzen and B. Farrell. Some realistic modifications of simple climate models. *Journal of Atmospheric Science*, 34:1487–1501, Oct. 1977.
- [124] M. Linsenmeier, S. Pascale, and V. Lucarini. Climate of Earth-like planets with high obliquity and eccentric orbits: Implications for habitability conditions. , 105:43–59, Jan 2015.
- [125] E. L. Lokas. Dark matter distribution in dwarf spheroidal galaxies. , 333(3):697–708, July 2002.
- [126] R. Luger and R. Barnes. Extreme Water Loss and Abiotic O₂ Buildup on Planets Throughout the Habitable Zones of M Dwarfs. *Astrobiology*, 15:119–143, Feb. 2015.
- [127] R. Luger, R. Barnes, E. Lopez, J. Fortney, B. Jackson, and V. Meadows. Habitable Evaporated Cores: Transforming Mini-Neptunes into Super-Earths in the Habitable Zones of M Dwarfs. *Astrobiology*, 15:57–88, Jan. 2015.
- [128] D. Lynden-Bell and P. P. Eggleton. On the consequences of the gravothermal catastrophe. *Monthly Notices of the Royal Astronomical Society*, 191(3):483–498, 07 1980.
- [129] A. V. Macciò and F. Fontanot. How cold is dark matter? Constraints from Milky Way satellites. , 404(1):L16–L20, May 2010.
- [130] J. March-Russell and S. M. West. WIMPonium and boost factors for indirect dark matter detection. *Physics Letters B*, 676(4-5):133–139, June 2009.
- [131] R. Massey, L. Williams, R. Smit, M. Swinbank, T. D. Kitching, D. Harvey, M. Jauzac, H. Israel, D. Clowe, A. Edge, M. Hilton, E. Jullo, A. Leonard, J. Liesenborgs, J. Merten, I. Mohammed, D. Nagai, J. Richard, A. Robertson, P. Saha, R. Santana, J. Stott, and E. Tittley. The behaviour of dark matter associated with four bright cluster galaxies in the 10 kpc core of Abell 3827. , 449(4):3393–3406, June 2015.
- [132] M. Mayor and D. Queloz. A Jupiter-mass companion to a solar-type star. , 378:355–359, Nov. 1995.
- [133] A. W. McConnachie. The Observed Properties of Dwarf Galaxies in and around the Local Group. , 144(1):4, July 2012.
- [134] S. S. McGaugh, V. C. Rubin, and W. J. G. de Blok. High-Resolution Rotation Curves of Low Surface Brightness Galaxies. I. Data. , 122(5):2381–2395, Nov. 2001.
- [135] W. B. McKinnon, R. T. Pappalardo, and K. K. Khurana. Europa: Perspectives on an Ocean World. In R. T. Pappalardo, W. B. McKinnon, and K. K. Khurana, editors, *Europa*, page 697. 2009.
- [136] V. S. Meadows and R. K. Barnes. *Factors Affecting Exoplanet Habitability*, page 57. 2018.

- [137] V. S. Meadows and D. Crisp. Ground-based near-infrared observations of the Venus nightside: The thermal structure and water abundance near the surface. , 101:4595, 1996.
- [138] M. Meneghetti, A. Ragagnin, S. Borgani, F. Calura, G. Despali, C. Giocoli, G. L. Granato, C. Grillo, L. Moscardini, E. Rasia, P. Rosati, G. Angora, L. Bassini, P. Bergamini, G. B. Caminha, G. Granata, A. Mercurio, R. B. Metcalf, P. Natarajan, M. Nonino, G. V. Pignataro, C. Ragone-Figueroa, E. Vanzella, A. Acebron, K. Dolag, G. Murante, G. Taffoni, L. Tornatore, L. Tortorelli, and M. Valentini. The probability of galaxy-galaxy strong lensing events in hydrodynamical simulations of galaxy clusters. , 668:A188, Dec. 2022.
- [139] K. Menou. Water-trapped Worlds. , 774(1):51, Sept. 2013.
- [140] H. Meskhidze, F. J. Mercado, O. Sameie, V. H. Robles, J. S. Bullock, M. Kaplinghat, and J. O. Weatherall. Comparing implementations of self-interacting dark matter in the GIZMO and AREPO codes. , 513(2):2600–2608, June 2022.
- [141] Q. Minor, S. Gad-Nasr, M. Kaplinghat, and S. Vegetti. An unexpected high concentration for the dark substructure in the gravitational lens SDSSJ0946+1006. , 507(2):1662–1683, Oct. 2021.
- [142] I. Mohammed, J. Liesenborgs, P. Saha, and L. L. R. Williams. Mass-galaxy offsets in Abell 3827, 2218 and 1689: intrinsic properties or line-of-sight substructures? , 439(3):2651–2661, Apr. 2014.
- [143] B. Moore, S. Ghigna, F. Governato, G. Lake, T. Quinn, J. Stadel, and P. Tozzi. Dark Matter Substructure within Galactic Halos. , 524(1):L19–L22, Oct. 1999.
- [144] R. A. Murray-Clay, E. I. Chiang, and N. Murray. Atmospheric Escape From Hot Jupiters. , 693(1):23–42, Mar 2009.
- [145] E. O. Nadler, A. Banerjee, S. Adhikari, Y.-Y. Mao, and R. H. Wechsler. Signatures of Velocity-dependent Dark Matter Self-interactions in Milky Way-mass Halos. , 896(2):112, June 2020.
- [146] D. Naef, D. W. Latham, M. Mayor, T. Mazeh, J. L. Beuzit, G. A. Drukier, C. Perrier-Bellet, D. Queloz, J. P. Sivan, G. Torres, S. Udry, and S. Zucker. HD 80606 b, a planet on an extremely elongated orbit. , 375:L27–L30, Aug 2001.
- [147] J. F. Navarro, C. S. Frenk, and S. D. M. White. A Universal Density Profile from Hierarchical Clustering. , 490(2):493–508, Dec. 1997.
- [148] H. Nishikawa, K. K. Boddy, and M. Kaplinghat. Accelerated core collapse in tidally stripped self-interacting dark matter halos. , 101(6):063009, Mar. 2020.
- [149] J. Oñorbe, M. Boylan-Kolchin, J. S. Bullock, P. F. Hopkins, D. Kereš, C.-A. Faucher-Giguère, E. Quataert, and N. Murray. Forged in FIRE: cusps, cores and baryons in low-mass dwarf galaxies. , 454(2):2092–2106, Dec. 2015.

- [150] P. Odert, M. Leitzinger, A. Hanslmeier, and H. Lammer. Stellar coronal mass ejections - I. Estimating occurrence frequencies and mass-loss rates. , 472(1):876–890, Nov 2017.
- [151] S.-H. Oh, W. J. G. de Blok, E. Brinks, F. Walter, and J. Kennicutt, Robert C. Dark and Luminous Matter in THINGS Dwarf Galaxies. , 141(6):193, June 2011.
- [152] S.-H. Oh, D. A. Hunter, E. Brinks, B. G. Elmegreen, A. Schruba, F. Walter, M. P. Rupen, L. M. Young, C. E. Simpson, M. C. Johnson, K. A. Herrmann, D. Ficut-Vicas, P. Cigan, V. Heesen, T. Ashley, and H.-X. Zhang. High-resolution Mass Models of Dwarf Galaxies from LITTLE THINGS. , 149(6):180, June 2015.
- [153] K. A. Oman, J. F. Navarro, A. Fattahi, C. S. Frenk, T. Sawala, S. D. M. White, R. Bower, R. A. Crain, M. Furlong, M. Schaller, J. Schaye, and T. Theuns. The unexpected diversity of dwarf galaxy rotation curves. , 452(4):3650–3665, Oct. 2015.
- [154] K. A. Oman, J. F. Navarro, L. V. Sales, A. Fattahi, C. S. Frenk, T. Sawala, M. Schaller, and S. D. M. White. Missing dark matter in dwarf galaxies? , 460(4):3610–3623, Aug. 2016.
- [155] N. J. Outmezguine, K. K. Boddy, S. Gad-Nasr, M. Kaplinghat, and L. Sagunski. Universal gravothermal evolution of isolated self-interacting dark matter halos for velocity-dependent cross sections. *arXiv e-prints*, page arXiv:2204.06568, Apr. 2022.
- [156] I. Palubski, O. Slone, M. Kaplinghat, M. Lisanti, and F. Jiang. Numerical Challenges in Modeling Gravothermal Collapse in Self-Interacting Dark Matter Halos. *arXiv e-prints*, page arXiv:2402.12452, Feb. 2024.
- [157] E. Papastergis, R. Giovanelli, M. P. Haynes, and F. Shankar. Is there a “too big to fail” problem in the field? , 574:A113, Feb. 2015.
- [158] R. Pierrehumbert. *Principles of Planetary Climate*. Cambridge University Press, 2010.
- [159] J. C. B. Pineda, C. C. Hayward, V. Springel, and C. Mendes de Oliveira. Rotation curve fitting and its fatal attraction to cores in realistically simulated galaxy observations. , 466(1):63–87, Apr. 2017.
- [160] Planck Collaboration, N. Aghanim, Y. Akrami, F. Arroja, M. Ashdown, J. Aumont, C. Baccigalupi, M. Ballardini, A. J. Banday, R. B. Barreiro, N. Bartolo, S. Basak, R. Battye, K. Benabed, J. P. Bernard, M. Bersanelli, P. Bielewicz, J. J. Bock, J. R. Bond, J. Borrill, F. R. Bouchet, F. Boulanger, M. Bucher, C. Burigana, R. C. Butler, E. Calabrese, J. F. Cardoso, J. Carron, B. Casaponsa, A. Challinor, H. C. Chiang, L. P. L. Colombo, C. Combet, D. Contreras, B. P. Crill, F. Cuttaia, P. de Bernardis, G. de Zotti, J. Delabrouille, J. M. Delouis, F. X. Désert, E. Di Valentino, C. Dickinson, J. M. Diego, S. Donzelli, O. Doré, M. Douspis, A. Ducout, X. Dupac, G. Efstathiou, F. Elsner, T. A. Enßlin, H. K. Eriksen, E. Falgarone, Y. Fantaye, J. Fergusson, R. Fernandez-Cobos, F. Finelli, F. Forastieri, M. Frailis, E. Franceschi, A. Frolov, S. Galeotta, S. Galli, K. Ganga, R. T. Génova-Santos, M. Gerbino, T. Ghosh, J. González-Nuevo, K. M. Górski, S. Gratton, A. Gruppuso, J. E. Gudmundsson,

- J. Hamann, W. Handley, F. K. Hansen, G. Helou, D. Herranz, S. R. Hildebrandt, E. Hivon, Z. Huang, A. H. Jaffe, W. C. Jones, A. Karakci, E. Keihänen, R. Keskitalo, K. Kiiveri, J. Kim, T. S. Kisner, L. Knox, N. Krachmalnicoff, M. Kunz, H. Kurki-Suonio, G. Lagache, J. M. Lamarre, M. Langer, A. Lasenby, M. Lattanzi, C. R. Lawrence, M. Le Jeune, J. P. Leahy, J. Lesgourgues, F. Levrier, A. Lewis, M. Liguori, P. B. Lilje, M. Lilley, V. Lindholm, M. López-Caniego, P. M. Lubin, Y. Z. Ma, J. F. Macías-Pérez, G. Maggio, D. Maino, N. Mandolesi, A. Mangilli, A. Marcos-Caballero, M. Maris, P. G. Martin, M. Martinelli, E. Martínez-González, S. Matarrese, N. Mauri, J. D. McEwen, P. D. Meerburg, P. R. Meinhold, A. Melchiorri, A. Mennella, M. Migliaccio, M. Millea, S. Mitra, M. A. Miville-Deschênes, D. Molinari, A. Moneti, L. Montier, G. Morgante, A. Moss, S. Mottet, M. Münchmeyer, P. Natoli, H. U. Nørgaard-Nielsen, C. A. Oxborrow, L. Pagano, D. Paoletti, B. Partridge, G. Patanchon, T. J. Pearson, M. Peel, H. V. Peiris, F. Perrotta, V. Pettorino, F. Piacentini, L. Polastri, G. Polenta, J. L. Puget, J. P. Rachen, M. Reinecke, M. Remazeilles, C. Renault, A. Renzi, G. Rocha, C. Rosset, G. Roudier, J. A. Rubiño-Martín, B. Ruiz-Granados, L. Salvati, M. Sandri, M. Savelainen, D. Scott, E. P. S. Shellard, M. Shirashi, C. Sirignano, G. Sirri, L. D. Spencer, R. Sunyaev, A. S. Suur-Uski, J. A. Tauber, D. Tavagnacco, M. Tenti, L. Terenzi, L. Toffolatti, M. Tomasi, T. Trombetti, J. Valiviita, B. Van Tent, L. Vibert, P. Vielva, F. Villa, N. Vittorio, B. D. Wandelt, I. K. Wehus, M. White, S. D. M. White, A. Zacchei, and A. Zonca. Planck 2018 results. I. Overview and the cosmological legacy of Planck. , 641:A1, Sept. 2020.
- [161] J. Pollack, D. N. Spergel, and P. J. Steinhardt. Supermassive Black Holes from Ultra-strongly Self-interacting Dark Matter. , 804(2):131, May 2015.
- [162] A. Pontzen and F. Governato. How supernova feedback turns dark matter cusps into cores. , 421(4):3464–3471, Apr. 2012.
- [163] M. Pospelov and A. Ritz. Astrophysical signatures of secluded dark matter. *Physics Letters B*, 671(3):391–397, Jan. 2009.
- [164] C. Power, J. F. Navarro, A. Jenkins, C. S. Frenk, S. D. M. White, V. Springel, J. Stadel, and T. Quinn. The inner structure of Λ CDM haloes - I. A numerical convergence study. , 338(1):14–34, Jan. 2003.
- [165] J. R. Primack and M. A. K. Gross. Hot dark matter in cosmology. In D. O. Caldwell, editor, *Current aspects of neutrino physics*, pages 287–308. 2001.
- [166] J. I. Read, M. G. Walker, and P. Steger. The case for a cold dark matter cusp in Draco. , 481(1):860–877, Nov. 2018.
- [167] P. L. Read, J. Barstow, B. Charnay, S. Chelvaniththilan, P. G. J. Irwin, S. Knight, S. Lebonnois, S. R. Lewis, J. Mendonça, and L. Montabone. Global energy budgets and âtrenberth diagramsâ for the climates of terrestrial and gas giant planets. *Quarterly Journal of the Royal Meteorological Society*, 142(695):703–720, 2016.

- [168] I. N. Reid, S. L. Hawley, and J. E. Gizis. The Palomar/MSU Nearby-Star Spectroscopic Survey. I. The Northern M Dwarfs -Bandstrengths and Kinematics. , 110:1838, Oct. 1995.
- [169] T. Ren, A. Kwa, M. Kaplinghat, and H.-B. Yu. Reconciling the Diversity and Uniformity of Galactic Rotation Curves with Self-Interacting Dark Matter. *Phys. Rev. X*, 9(3):031020, 2019.
- [170] I. Ribas, E. Bolmont, F. Selsis, A. Reiners, J. Leconte, S. N. Raymond, S. G. Engle, E. F. Guinan, J. Morin, M. Turbet, F. Forget, and G. Anglada-Escude. The habitability of Proxima Centauri b. I. Irradiation, rotation and volatile inventory from formation to the present. *ArXiv e-prints*, Aug. 2016.
- [171] G. R. Ricker, J. N. Winn, R. Vanderspek, D. W. Latham, G. Á. Bakos, J. L. Bean, Z. K. Berta-Thompson, T. M. Brown, L. Buchhave, N. R. Butler, R. P. Butler, W. J. Chaplin, D. Charbonneau, J. Christensen-Dalsgaard, M. Clampin, D. Deming, J. Doty, N. De Lee, C. Dressing, E. W. Dunham, M. Endl, F. Fressin, J. Ge, T. Henning, M. J. Holman, A. W. Howard, S. Ida, J. M. Jenkins, G. Jernigan, J. A. Johnson, L. Kaltenegger, N. Kawai, H. Kjeldsen, G. Laughlin, A. M. Levine, D. Lin, J. J. Lissauer, P. MacQueen, G. Marcy, P. R. McCullough, T. D. Morton, N. Narita, M. Paegert, E. Palles, F. Pepe, J. Pepper, A. Quirrenbach, S. A. Rinehart, D. Sasselov, B. Sato, S. Seager, A. Sozzetti, K. G. Stassun, P. Sullivan, A. Szentgyorgyi, G. Torres, S. Udry, and J. Villaseñor. Transiting Exoplanet Survey Satellite (TESS). *Journal of Astronomical Telescopes, Instruments, and Systems*, 1:014003, Jan. 2015.
- [172] A. Robertson, R. Massey, and V. Eke. Cosmic particle colliders: simulations of self-interacting dark matter with anisotropic scattering. , 467(4):4719–4730, June 2017.
- [173] A. Robertson, R. Massey, and V. Eke. What does the Bullet Cluster tell us about self-interacting dark matter? , 465(1):569–587, Feb. 2017.
- [174] V. H. Robles, J. S. Bullock, O. D. Elbert, A. Fitts, A. González-Samaniego, M. Boylan-Kolchin, P. F. Hopkins, C.-A. Faucher-Giguère, D. Kereš, and C. C. Hayward. SIDM on FIRE: hydrodynamical self-interacting dark matter simulations of low-mass dwarf galaxies. , 472(3):2945–2954, Dec. 2017.
- [175] V. H. Robles, T. Kelley, J. S. Bullock, and M. Kaplinghat. The Milky Way’s halo and subhaloes in self-interacting dark matter. , 490(2):2117–2123, Dec. 2019.
- [176] M. Rocha, A. H. G. Peter, J. S. Bullock, M. Kaplinghat, S. Garrison-Kimmel, J. Oñorbe, and L. A. Moustakas. Cosmological simulations with self-interacting dark matter - I. Constant-density cores and substructure. , 430(1):81–104, Mar. 2013.
- [177] B. E. J. Rose, T. W. Cronin, and C. M. Bitz. Ice Caps and Ice Belts: The Effects of Obliquity on Ice-Albedo Feedback. , 846(1):28, Sep 2017.
- [178] V. C. Rubin and J. Ford, W. Kent. Rotation of the Andromeda Nebula from a Spectroscopic Survey of Emission Regions. , 159:379, Feb. 1970.

- [179] O. Sameie, M. Boylan-Kolchin, R. Sanderson, D. Vargya, P. F. Hopkins, A. Wetzel, J. Bullock, A. Graus, and V. H. Robles. The central densities of Milky Way-mass galaxies in cold and self-interacting dark matter models. , 507(1):720–729, Oct. 2021.
- [180] J. Scalo, L. Kaltenegger, A. G. Segura, M. Fridlund, I. Ribas, Y. N. Kulikov, J. L. Grenfell, H. Rauer, P. Odert, M. Leitzinger, F. Selsis, M. L. Khodachenko, C. Eiroa, J. Kasting, and H. Lammer. M Stars as Targets for Terrestrial Exoplanet Searches And Biosignature Detection. *Astrobiology*, 7(1):85–166, Feb 2007.
- [181] M. Schaller, A. Robertson, R. Massey, R. G. Bower, and V. R. Eke. The offsets between galaxies and their dark matter in Λ cold dark matter. , 453(1):L58–L62, Oct. 2015.
- [182] E. W. Schwieterman, N. Y. Kiang, M. N. Parenteau, C. E. Harman, S. DasSarma, T. M. Fisher, G. N. Arney, H. E. Hartnett, C. T. Reinhard, S. L. Olson, V. S. Meadows, C. S. Cockell, S. I. Walker, J. L. Grenfell, S. Hegde, S. Rugheimer, R. Hu, and T. W. Lyons. Exoplanet Biosignatures: A Review of Remotely Detectable Signs of Life. *Astrobiology*, 18(6):663–708, June 2018.
- [183] E. W. Schwieterman and M. Leung. An Overview of Exoplanet Biosignatures. *Reviews in Mineralogy and Geochemistry*, 90(1):465–514, July 2024.
- [184] S. Seager. *Exoplanets*. 2010.
- [185] S. Seager. Exoplanet Habitability. *Science*, 340(6132):577–581, May 2013.
- [186] A. Segura, J. F. Kasting, V. Meadows, M. Cohen, J. Scalo, D. Crisp, R. A. H. Butler, and G. Tinetti. Biosignatures from Earth-Like Planets Around M Dwarfs. *Astrobiology*, 5:706–725, Dec. 2005.
- [187] A. Segura, K. Krelove, J. F. Kasting, D. Sommerlatt, V. Meadows, D. Crisp, M. Cohen, and E. Mlawer. Ozone Concentrations and Ultraviolet Fluxes on Earth-Like Planets Around Other Stars. *Astrobiology*, 3(4):689–708, Dec 2003.
- [188] F. Selsis, J. F. Kasting, B. Levrard, J. Paillet, I. Ribas, and X. Delfosse. Habitable planets around the star Gliese 581? , 476:1373–1387, Dec. 2007.
- [189] A. L. Shields. The climates of other worlds: A review of the emerging field of exoplanet climatology. *The Astrophysical Journal Supplement Series*, 243(2):30, aug 2019.
- [190] A. L. Shields, S. Ballard, and J. A. Johnson. The habitability of planets orbiting m-dwarf stars. 663:1 – 38, 2016b. The habitability of planets orbiting M-dwarf stars.
- [191] A. L. Shields, C. M. Bitz, V. S. Meadows, M. M. Joshi, and T. D. Robinson. Spectrum-driven Planetary Deglaciation due to Increases in Stellar Luminosity. , 785(1):L9, Apr 2014.
- [192] A. L. Shields, C. M. Bitz, and I. Palubski. Energy Budgets for Terrestrial Extrasolar Planets. , 884(1):L2, Oct 2019.

- [193] A. L. Shields, V. S. Meadows, C. M. Bitz, R. T. Pierrehumbert, M. M. Joshi, and T. D. Robinson. The Effect of Host Star Spectral Energy Distribution and Ice-Albedo Feedback on the Climate of Extrasolar Planets. *Astrobiology*, 13:715–739, Aug. 2013.
- [194] A. P. Showman and Y. Kaspi. Atmospheric Dynamics of Brown Dwarfs and Directly Imaged Giant Planets. *The Astrophysical Journal*, 776(2):85, Oct 2013.
- [195] M. Silverman, J. S. Bullock, M. Kaplinghat, V. H. Robles, and M. Valli. Motivations for a large self-interacting dark matter cross-section from milky way satellites. *Monthly Notices of the Royal Astronomical Society*, 518(2):2418–2435, Nov. 2022.
- [196] J. D. Simon, A. D. Bolatto, A. Leroy, L. Blitz, and E. L. Gates. High-Resolution Measurements of the Halos of Four Dark Matter-Dominated Galaxies: Deviations from a Universal Density Profile. , 621(2):757–776, Mar. 2005.
- [197] O. Slone, F. Jiang, M. Lisanti, and M. Kaplinghat. Orbital evolution of satellite galaxies in self-interacting dark matter models. *Phys. Rev. D*, 107(4):043014, 2023.
- [198] D. N. Spergel and P. J. Steinhardt. Observational Evidence for Self-Interacting Cold Dark Matter. , 84(17):3760–3763, Apr. 2000.
- [199] D. N. Spergel, L. Verde, H. V. Peiris, E. Komatsu, M. R. Nolta, C. L. Bennett, M. Halpern, G. Hinshaw, N. Jarosik, A. Kogut, M. Limon, S. S. Meyer, L. Page, G. S. Tucker, J. L. Weiland, E. Wollack, and E. L. Wright. First-Year Wilkinson Microwave Anisotropy Probe (WMAP) Observations: Determination of Cosmological Parameters. , 148(1):175–194, Sept. 2003.
- [200] D. S. Spiegel, K. Menou, and C. A. Scharf. Habitable Climates: The Influence of Obliquity. , 691(1):596–610, Jan 2009.
- [201] V. Springel. The cosmological simulation code GADGET-2. , 364(4):1105–1134, Dec. 2005.
- [202] J. C. Tarter, P. R. Backus, R. L. Mancinelli, J. M. Aurnou, D. E. Backman, G. S. Basri, A. P. Boss, A. Clarke, D. Deming, L. R. Doyle, E. D. Feigelson, F. Freund, D. H. Grinspoon, R. M. Haberle, S. A. Hauck, II, M. J. Heath, T. J. Henry, J. L. Hollingsworth, M. M. Joshi, S. Kilston, M. C. Liu, E. Meikle, I. N. Reid, L. J. Rothschild, J. Scalo, A. Segura, C. M. Tang, J. M. Tiedje, M. C. Turnbull, L. M. Walkowicz, A. L. Weber, and R. E. Young. A Reappraisal of The Habitability of Planets around M Dwarf Stars. *Astrobiology*, 7:30–65, Mar. 2007.
- [203] R. Teyssier, A. Pontzen, Y. Dubois, and J. I. Read. Cusp-core transformations in dwarf galaxies: observational predictions. , 429(4):3068–3078, Mar. 2013.
- [204] G. Torrealba, V. Belokurov, and S. E. Koposov. Nine tiny star clusters in Gaia DR1, PS1, and DES. , 484(2):2181–2197, Apr. 2019.

- [205] S. Trujillo-Gomez, A. Klypin, P. Colín, D. Ceverino, K. S. Arraki, and J. Primack. Low-mass galaxy assembly in simulations: regulation of early star formation by radiation from massive stars. , 446(2):1140–1162, Jan. 2015.
- [206] S. Tulin and H.-B. Yu. Dark Matter Self-interactions and Small Scale Structure. *Phys. Rept.*, 730:1–57, 2018.
- [207] S. Tulin and H.-B. Yu. Dark matter self-interactions and small scale structure. *Physics Reports*, 730:1–57, 2018. Dark matter self-interactions and small scale structure.
- [208] S. Tulin, H.-B. Yu, and K. M. Zurek. Beyond collisionless dark matter: Particle physics dynamics for dark matter halo structure. , 87(11):115007, June 2013.
- [209] M. Turbet, J. Leconte, F. Selsis, E. Bolmont, F. Forget, I. Ribas, S. N. Raymond, and G. Anglada-Escudé. The habitability of Proxima Centauri b. II. Possible climates and observability. , 596:A112, Dec. 2016.
- [210] H. C. Turner, M. R. Lovell, J. Zavala, and M. Vogelsberger. The onset of gravothermal core collapse in velocity-dependent self-interacting dark matter subhaloes. , 505(4):5327–5339, Aug. 2021.
- [211] M. Valli and H.-B. Yu. Dark matter self-interactions from the internal dynamics of dwarf spheroidals. *Nature Astronomy*, 2:907–912, Aug. 2018.
- [212] F. C. van den Bosch and G. Ogiya. Dark matter substructure in numerical simulations: a tale of discreteness noise, runaway instabilities, and artificial disruption. , 475(3):4066–4087, Apr. 2018.
- [213] S. D. Vance, K. L. Craft, E. Shock, B. E. Schmidt, J. Lunine, K. P. Hand, W. B. McKinnon, E. M. Spiers, C. Chivers, J. D. Lawrence, N. Wolfenbarger, E. J. Leonard, K. J. Robinson, M. J. Styczinski, D. M. Persaud, G. Steinbrügge, M. Y. Zolotov, L. C. Quick, J. E. C. Scully, T. M. Becker, S. M. Howell, R. N. Clark, A. J. Dombard, C. R. Glein, O. Mousis, M. A. Sephton, J. Castillo-Rogez, F. Nimmo, A. S. McEwen, M. S. Gudipati, I. Jun, X. Jia, F. Postberg, K. M. Soderlund, and C. M. Elder. Investigating Europa’s Habitability with the Europa Clipper. , 219(8):81, Dec. 2023.
- [214] M. Vogelsberger, J. Zavala, and A. Loeb. Subhaloes in self-interacting galactic dark matter haloes. , 423(4):3740–3752, July 2012.
- [215] J. C. G. Walker, P. B. Hays, and J. F. Kasting. A negative feedback mechanism for the long-term stabilization of the earth’s surface temperature. , 86:9776–9782, Oct. 1981.
- [216] M. G. Walker, M. Mateo, E. W. Olszewski, J. Peñarrubia, N. W. Evans, and G. Gilmore. A Universal Mass Profile for Dwarf Spheroidal Galaxies? , 704(2):1274–1287, Oct. 2009.
- [217] M. Wieczorek. 10.05 - gravity and topography of the terrestrial planets. In G. Schubert, editor, *Treatise on Geophysics*, pages 165 – 206. Elsevier, Amsterdam, 2007.

- [218] D. M. Williams and J. F. Kasting. Habitable Planets with High Obliquities. , 129:254–267, Sept. 1997.
- [219] D. M. Williams and D. Pollard. Earth-like worlds on eccentric orbits: excursions beyond the habitable zone. *International Journal of Astrobiology*, 1:61–69, Jan 2002.
- [220] G. E. Williams. Late precambrian glacial climate and the earth’s obliquity. *Geological Magazine*, 112(5):441–544, 1975.
- [221] B. Willman. In Pursuit of the Least Luminous Galaxies. *Advances in Astronomy*, 2010:285454, Jan. 2010.
- [222] R. A. Wittenmyer, M. I. Jones, J. Horner, S. R. Kane, J. P. Marshall, A. J. Mustill, J. S. Jenkins, P. A. Pena Rojas, J. Zhao, and E. Villaver. The Pan-Pacific Planet Search. VII. The Most Eccentric Planet Orbiting a Giant Star. , 154(6):274, Dec 2017.
- [223] E. T. Wolf, A. L. Shields, R. K. Kopparapu, J. Haqq-Misra, and O. B. Toon. Constraints on Climate and Habitability for Earth-like Exoplanets Determined from a General Circulation Model. , 837(2):107, Mar 2017.
- [224] E. T. Wolf and O. B. Toon. The evolution of habitable climates under the brightening Sun. *Journal of Geophysical Research (Atmospheres)*, 120(12):5775–5794, Jun 2015.
- [225] J. Wolf, G. D. Martinez, J. S. Bullock, M. Kaplinghat, M. Geha, R. R. Muñoz, J. D. Simon, and F. F. Avedo. Accurate masses for dispersion-supported galaxies. , 406(2):1220–1237, Aug. 2010.
- [226] R. Wordsworth. Atmospheric Heat Redistribution and Collapse on Tidally Locked Rocky Planets. , 806:180, June 2015.
- [227] R. Wordsworth. Atmospheric Heat Redistribution and Collapse on Tidally Locked Rocky Planets. , 806(2):180, June 2015.
- [228] R. Wordsworth and R. Pierrehumbert. Abiotic Oxygen-dominated Atmospheres on Terrestrial Habitable Zone Planets. , 785(2):L20, Apr 2014.
- [229] D. Yang, E. O. Nadler, and H.-b. Yu. Strong Dark Matter Self-interactions Diversify Halo Populations Within and Surrounding the Milky Way. *arXiv e-prints*, page arXiv:2211.13768, Nov. 2022.
- [230] D. Yang, E. O. Nadler, H.-B. Yu, and Y.-M. Zhong. A Parametric Model for Self-Interacting Dark Matter Halos. 5 2023.
- [231] D. Yang and H.-B. Yu. Self-interacting dark matter and small-scale gravitational lenses in galaxy clusters. , 104(10):103031, Nov. 2021.
- [232] D. Yang and H.-B. Yu. Gravothermal evolution of dark matter halos with differential elastic scattering. *JCAP*, 09:077, 2022.

- [233] J. Yang, N. B. Cowan, and D. S. Abbot. Stabilizing Cloud Feedback Dramatically Expands the Habitable Zone of Tidally Locked Planets. , 771(2):L45, July 2013.
- [234] S. Yang, X. Du, Z. C. Zeng, A. Benson, F. Jiang, E. O. Nadler, and A. H. G. Peter. Gravothermal Solutions of SIDM Halos: Mapping from Constant to Velocity-dependent Cross Section. , 946(1):47, Mar. 2023.
- [235] N. Yoshida, V. Springel, S. D. M. White, and G. Tormen. Weakly Self-interacting Dark Matter and the Structure of Dark Halos. , 544(2):L87–L90, Dec. 2000.
- [236] J. Zavala, M. R. Lovell, M. Vogelsberger, and J. D. Burger. Diverse dark matter density at sub-kiloparsec scales in Milky Way satellites: Implications for the nature of dark matter. *Phys. Rev. D*, 100(6):063007, 2019.
- [237] J. Zavala, M. Vogelsberger, and M. G. Walker. Constraining self-interacting dark matter with the Milky way’s dwarf spheroidals. , 431:L20–L24, Apr. 2013.
- [238] M. Zemp, B. Moore, J. Stadel, C. M. Carollo, and P. Madau. Multimass spherical structure models for N-body simulations. , 386(3):1543–1556, May 2008.
- [239] Z. C. Zeng, A. H. G. Peter, X. Du, A. Benson, S. Kim, F. Jiang, F.-Y. Cyr-Racine, and M. Vogelsberger. Core-collapse, evaporation, and tidal effects: the life story of a self-interacting dark matter subhalo. , 513(4):4845–4868, July 2022.
- [240] A. Zentner, S. Dandavate, O. Slone, and M. Lisanti. A critical assessment of solutions to the galaxy diversity problem. *JCAP*, 07(07):031, 2022.
- [241] G. Zhang, A. c. Şengül, and C. Dvorkin. Subhalo effective density slope measurements from HST strong lensing data with neural likelihood-ratio estimation. 8 2023.
- [242] Y.-M. Zhong, D. Yang, and H.-B. Yu. The impact of baryonic potentials on the gravothermal evolution of self-interacting dark matter haloes. *Mon. Not. Roy. Astron. Soc.*, 526(1):758–770, 2023.
- [243] A. Zolotov, A. M. Brooks, B. Willman, F. Governato, A. Pontzen, C. Christensen, A. Dekel, T. Quinn, S. Shen, and J. Wadsley. Baryons Matter: Why Luminous Satellite Galaxies have Reduced Central Masses. , 761(1):71, Dec. 2012.
- [244] F. Zwicky. Die Rotverschiebung von extragalaktischen Nebeln. *Helvetica Physica Acta*, 6:110–127, Jan. 1933.

Appendix A

A.1 Supplementary Figures to Chapter 4

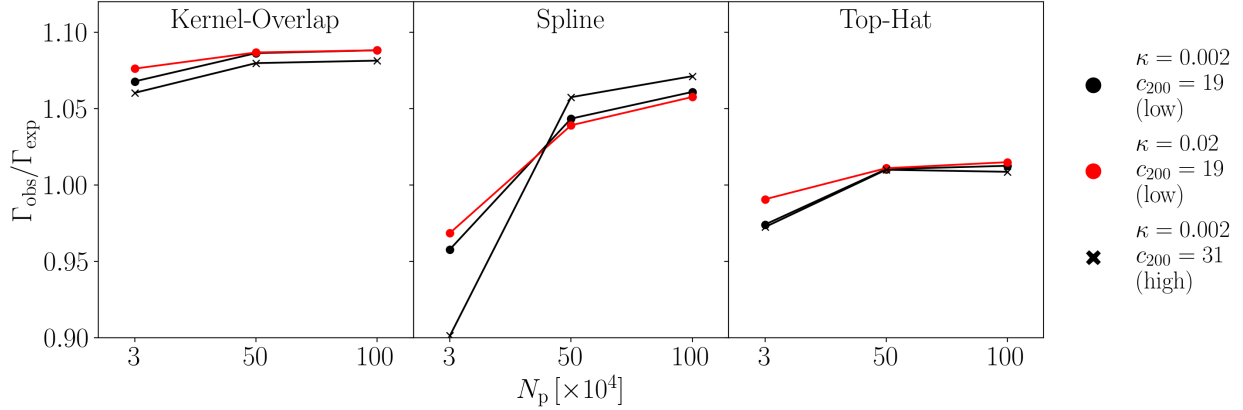


Figure A1: The observed scattering rate, Γ_{obs} , as a fraction of the expected rate, Γ_{exp} , plotted as a function of number of particles, N_p . The left, middle and right columns correspond to the Kernel-Overlap, Spline, and Top-Hat results, respectively. Results for the low-concentration halo with $\kappa = 0.002$ and 0.02 are shown by the filled black and red circles, respectively. Results for the high-concentration $\kappa = 0.002$ halo are shown by the black crosses. In general, $\Gamma_{\text{obs}}/\Gamma_{\text{exp}}$ approaches a common value as the resolution improves. At the highest resolution simulated here, there are still systematic offsets between the observed and expected scattering rate, with the magnitude depending on the specific SIDM implementation.

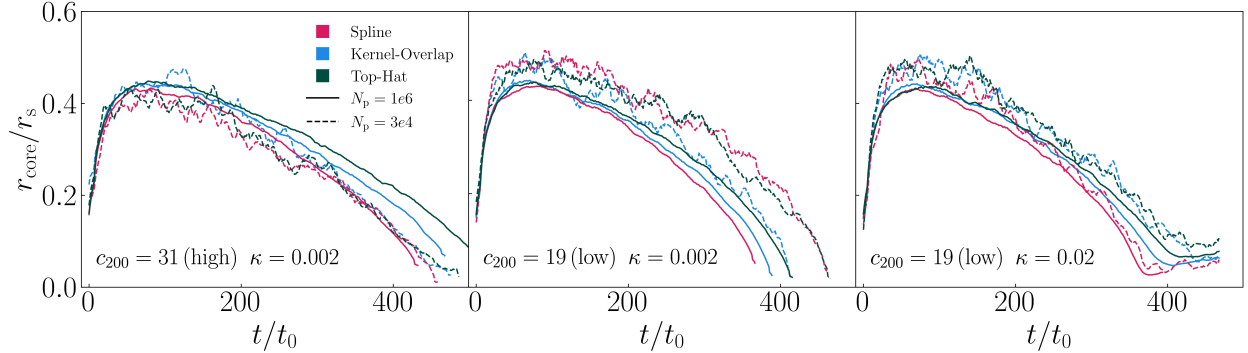


Figure A2: The evolution of the halo's core size, r_{core} , rescaled to its scale radius, r_s . Results are shown for the low- and high-concentration halos and for different time-stepping criteria. Solid (dashed) lines correspond to the highest (lowest)-resolution simulations run here. The Spline, Kernel-Overlap, and Top-Hat results are shown by the red, blue, and green lines, respectively. The simulations with $\kappa = 0.02$ (right panel) show a visible stalling of the core collapse as the core size grows more slowly at late times in the halo's evolution.